Studies on Time-Delayed Feedback Control of Chaos and its Application to Dynamic Force Microscopy

A Dissertation
Presented to the Faculty of the Graduate School
of Kyoto University
in Partial Fulfillment of the Requirements for the Degree of
Doctor of Philosophy

by

Kohei Yamasue

November 2006

Abstract

The time-delayed feedback control is well-known as a practical method for continuous control of chaos, which was proposed by Pyragas in the field of nonlinear dynamics. The first purpose of this thesis is clarification of the ability and characteristics of the time-delayed feedback control of chaos particularly from the viewpoint of the global dynamics of controlled systems, going beyond the traditional analyses based on linearization. The second is to present a novel application of this control method to a chaotic oscillation in a nanoengineering system, called the dynamic force microscope or dynamic-mode atomic force microscope. This thesis contributes to the engineering application of nonlinear dynamics and chaos, and its control especially to nanoengineering systems.

The time-delayed feedback control is one of the most famous chaos control methods due to the diverse fields of application. Experimental demonstration of its ability has been performed to electronic circuits, laser, mechanical oscillators, gas charge systems, chemical systems, plasma, fluids, and so on. Stabilization of unstable periodic orbits embedded in chaotic attractors has been achieved by feedback of the error signal between the current output and the past one of a chaotic system one wishes to control. Utilization of the delayed output allows us to implement the control method to chaotic systems without the exact models, identification of the parameters, nor complicated data processing for reconstruction of underlying dynamics. On the other hand, the time delay introduced to the feedback loop causes difficulty in theoretical analysis of control performance. Dynamics of a controlled system is described by a difference differential equa-

tion and thereby the phase space of the system is a function space, even if the uncontrolled system is finite dimensional. Linearization based approaches have been effectively applied to this infinite dimensional system; however, the scope is essentially limited to the stability of target orbits, or local dynamics in the neighborhood of the orbits. There have been still very few studies referring to the global dynamics of controlled systems and related problems.

Analyses from the viewpoint of the global dynamics are essential especially for chaos control in engineering systems. Clarification of the stability of target orbits cannot fully explain the ability and performance of the control method due to the global nature of chaotic dynamics. Since there is no contradiction if chaotic dynamics coexists with locally stabilized target orbits, the controlled systems can show chaotic behavior in the transient state and have a complicated domain of attraction for the target orbits. The controlled systems can restart to show chaotic behavior even under control, because they are frequently exposed to disturbance such as noise and transient change of system parameters. The chaotic nature of controlled systems in the infinite dimensional function space is fully captured for the first time by this study, which is chiefly performed numerically in the two-well Duffing system under time-delayed feedback control. The thesis begins with a detailed investigation of multiple steady states and their bifurcations. A wide variety of stable orbits different from the target ones are found in the controlled systems, and the mechanism of their stability loss and annihilation are clarified based on the bifurcation theory. The origin of these orbits coexisting with the targets is also discussed and it is then shown that they are derived from the non-target unstable periodic orbits embedded in the chaotic attractor. Coexistence of different stable orbits motivates us to examine the domain of attraction for the target orbits, i.e., regions in the phase space where the initial conditions achieve the convergence of the resulting solutions to the target orbits. The domain of attraction in function space is examined by giving a perturbation to initial conditions toward target orbits. Complicated boundary structures with self-similarity elucidated in this thesis suggest the existence of chaotic dynamics under control. Direct access to the global dynamics in function space is also carried out by employing a global unstable manifold as a probe for observing a phase structure governing the controlled two-well Duffing systems. Possibility of the coexistence of the original chaotic dynamics with stabilized target orbits is demonstrated by revealing a primary and qualitative change of the global phase structure for increase of feedback gain. As its intrinsic nature, persistence of the original chaotic dynamics has destructive influences on the control performance. Transient behavior becomes chaotic and too long, and domain of attraction is also made complicated, even if the control parameters are optimized from the viewpoint of local stability of target orbits. On the other hand, the global phase structure is simplified and then control performances are much improved as feedback gain is increased. This simplification of the global phase structure for increasing feedback gain is generalized to a periodic system under control. A general scenario to the simplification is explained by a theoretical approach associated with the harmonic balance method. The simplification of global dynamics is a promising explanation to the ability of the control method, which was experimentally proved in various systems. The general theoretical approach presented in this thesis can provide a fundamental framework to classify controllable dynamical systems from the viewpoint of global dynamics.

As an application of the time-delayed feedback control, this thesis proposes stabilization of chaotic oscillations of microcantilever sensors in the dynamic fore microscopy. The dynamic force microscopy is a member of scanning probe microscopy and one of the most promising technologies to support the future development of science and engineering in nanoscale. The science and engineering in nanoscale are a new and little explored field of research for nonlinear dynamics and chaos. Recent pioneering works on this field have shown the microcantilever sensors possibly exhibit chaotic oscillations due to a nonlinear interaction between the sensors and target material surfaces one tries to observe. Since the irregular and unpredictable sensors' oscillations significantly deteriorate measurement performance, it is required to develop control techniques to stabilize microcantilever oscillation. As a first step toward control, this thesis numerically demonstrates

elimination of two different chaotic oscillations using the time-delayed feedback control. An extended operating range of the dynamic force microscopes is estimated by stability analysis of the target periodic oscillation. The estimation also clarifies the possibility of improved transient responses of microcantilever oscillation, which allows us to accelerate the scanning rate of the dynamic force microscopes without reducing their force sensitivity. These results show the possibility of the application and provide important information on control performance toward control of actual dynamic force microscopes.

Acknowledgements

I wish to express my foremost and sincere appreciation to Professor Takashi Hikihara, without whose guidance and encouragement the present work would not have been possible. Almost six years ago, he opened the door to the world of nonlinear dynamics and chaos in front of me. His keen insight has also shown me a perspective to its novel application to nanoengineering. His constant cares and efforts on all the aspects of research and education have enabled us to challenge the new fields of research and enjoy life in this laboratory with his excellent leadership and truthful attitude. As a student, I have the confidence in the encounter with a character and I will keep it all through my life.

I would like to appreciate Professor Ralph Abraham, University of California, Santa Cruz, for his valuable suggestions from the viewpoint of the dynamical system theory. His deep theoretical background helped me with a theoretical treatment of the time-delayed feedback controlled systems. I also would like to thank Professor Igor Mezić, University of California, Santa Barbara. He kindly accepted my use of the model for the dynamic force microscopy. This study has been greatly motivated by the early work of his research group on the nonlinear dynamics and chaos in the dynamic force microscopy. The fruitful discussion has also given me a perspective to generalization of the present theoretical work.

I would like to appreciate Dr. Robert Walter Stark, Dr. Ferdinand Jamitzky, and Dr. Javier Rubio-Sierra, Ludwig-Maximilians-Universität München for their precious comments on nonlinear dynamics and control of microcantilevers in the dynamic force microscopy. Month's stay at München for collaboration toward experimental validation of the present work let me realize difficulty in reality and their endeavor to overcome the problems in real systems.

I am greatly indebted to the faculty and students in the Graduate School of Engineering, Kyoto University. In particular, I would like to thank Professor Kazumi Matsushige, Professor Hirofumi Yamada, Dr. Kei Kobayashi, and all other members of electronic material science and engineering laboratory for fruitful discussions and valuable suggestions on actual operation of the dynamic force microscopes. Professor Hirofumi Yamada also served on my dissertation committee. I would like to express my gratitude to Professor Masao Kitano for serving on my dissertation committee. He also provided me a significant comment, which reminded me of the attitude to technological problems as an engineer. I also would like to thank Professor Tsuyoshi Funaki for his encouragement and many precious suggestions on the circuit implementation of the time-delayed feedback control. Special thanks to Dr. Yoshihiko Susuki for his helpful advices and encouragement since my assign to the current laboratory in April, 2001. He has provided tangible and intangible bases to a Ph. D student following him. I would like to appreciate all the members of Professor Hikihara's research group including the past members. In particular, I would like to thank Ms. Keiko Saito, Ms. Minghua Li, Mr. Masayuki Kimura, and Mr. Tatsuya Tomita for their supports to research environment, encouragement, and valuable discussions.

I am grateful to the support of the Ministry of Education, Culture, Sports, Science and Technology in Japan, The 21st Century COE Program (Grant No. 14213201).

Finally, I would like to thank my parents, Yuji and Minako Yamasue for their continual supports and encouragement.

Contents

List of acronyms and symbols

Acronyms

A/D	Analog-to-Digital
AFM	Atomic Force Microscopy / Atomic Force Microscope
AM-DFM	DFM with Amplitude Modulation detection
DFM	Dynamic Force Microscopy / Dynamic Force Microscope
D/A	Digital-to-Analog
ETDAS	Extended Time-Delay Auto-Synchronization
FIFO	First In First Out
FM-DFM	DFM with Frequency Modulation detection
GAIO	software package for Global Analysis of Invariant Objects
IECE	the Institute of Electronics and Communication Engineers of Japan
IEICE	the Institute of Electronics, Information and Communication Engineers
ISCIE	the Institute of Systems, Control and Information Engineers
OGY	Initial letters of three persons' name, Ott, Grebogi, and Yorke
OPF	Occasional Proportional Feedback
PD	Period-Doubling bifurcation
RFDE	Retarded Functional Differential Equation
RMS-DC	Root-Mean-Square to Direct Current
SN	Saddle-Node bifurcation
SPM	Scanning Probe Microscopy / Scanning Probe Microscope
STM	Scanning Tunneling Microscopy / Scanning Tunneling Microscope

Frequently used symbols

α	equilibrium position of microcantilever tip
δ	damping constant of two-well Duffing system
ρ	amplitude of perturbation to initial condition
τ	time delay
μ	center of perturbation to initial condition
ϕ	initial condition in function space
ω	angular frequency of external sinusoidal force given to two-well Duffing system
A	amplitude of external sinusoidal force given to two-well Duffing system
Γ	amplitude of driving force to microcantilever
Δ	damping constant of microcantilever
Ω	angular frequency of driving force to microcantilever
t_0	onset time of control
u	control input
x	displacement of magnetoelastic beam / microcantilever
y	velocity of magnetoelastic beam / microcantilever
K	feedback gain
T	period of external sinusoidal force
$^1\mathsf{D}$	directly unstable periodic orbit in the two-well Duffing system
$^1\mathsf{I}$	inversely unstable periodic orbit in right side
$^1\mathsf{I}'$	inversely unstable periodic orbit in left side
$\mathcal{R}$	the set of real numbers
$^1\mathsf{S}$	$^1\mathsf{I}$ stabilized by control
$^1\mathsf{S}'$	$^1\mathsf{I}'$ stabilized by control
TD	two-well Duffing system with displacement feedback control
TV	two-well Duffing system with velocity feedback control

Chapter 1

Introduction

1.1 Chaos and its control

Chaos is nowadays widely recognized as a universal phenomenon arising in nonlinear dynamical systems [1–8]. Since the pioneer works on chaos by Ueda [1, 9] and Lorenz in the early 1960s [10], irregular and unpredictable dynamics observed in a wide variety of systems have been explained by simple deterministic mathematical models [11–19]. The explosive growth of research through the 1970s and the 1980s had shed light on the dynamical system theory, which was long-established field of mathematics since the end of the 19th century. Excellent theoretical explanation has been provided to the universal mechanism of diverse nonlinear phenomenon, including multiple steady states, bifurcations, fractal basin boundaries, and chaotic dynamics [20, 21]. The early great success has boosted the development of the dynamical system theory. Engineering applications of nonlinear dynamics and chaos simultaneously have come into the view of us.

Most of the applications using chaotic dynamics well known in the present day are based on the novel and sophisticated ideas appearing in the beginning of the 1990s. The controlling chaos [22], chaos synchronization [23], and chaos communication [24] have been the most prominent and kept motivating many researchers to study nonlinear dynamics and chaos up to the present. The controlling chaos, the idea by Ott, Grebogi, and Yorke, opened a new avenue of controlling

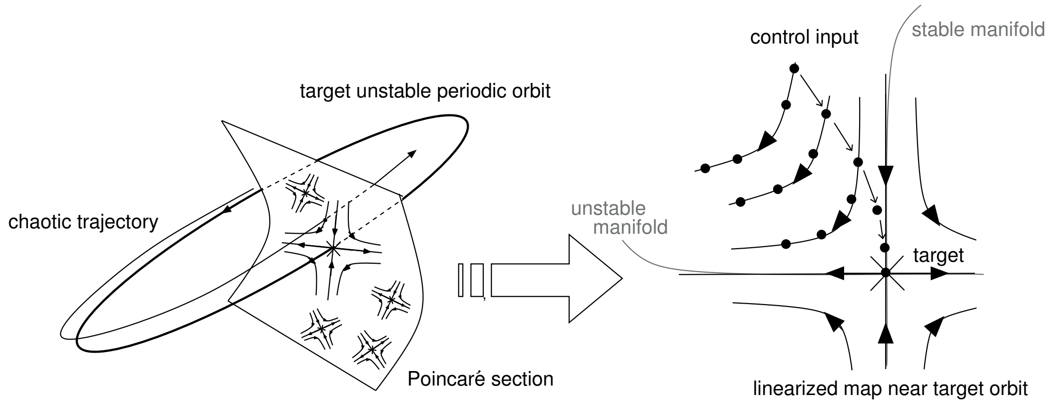

Figure 1.1: The idea of controlling chaos by Ott, Grebogi, and Yorke [22]. A chaotic trajectory approaches an arbitrary unstable periodic orbit along its stable manifold on a Poincaré section. Control input is applied to the trajectory coming close to a selected target orbit so that the trajectory moves on the stable manifold of the target. The controlled trajectory then converges to the target along the stable manifold and the control input simultaneously goes to zero. The linearized map is employed for calculation of the control input.

dynamics especially in front of physicists [25–27]. They introduced a seemingly paradoxical idea: chaotic motion of a system is converted to regular and periodic motion by only a slight modification of the system. The seminal paper in 1990 suggested that small and carefully chosen perturbation to accessible parameters or state variables of a chaotic system can stabilize unstable periodic orbits embedded in the chaotic attractor of the system [22]. The stabilization of unstable periodic orbits in itself was not a new idea at all especially in engineering fields; there arose, however, a definitely different philosophy that intends to make use of features of chaotic attractors. Since unstable periodic orbits is densely embedded in the chaotic attractor, one can stabilize a target orbit arbitrarily chosen from an infinite number of the unstable periodic motions intrinsic to a system. The stabilization of the intrinsic periodic motions is significant, if the motions are needed to keep or improve performance of the system. Any chaotic trajectory is, furthermore, guaranteed to come close to the target orbit in the finite time without external input. The system visits arbitrarily close to a given point or an unstable periodic orbit in the chaotic attractor arbitrarily many times. The target orbit is stabilized by applying only small control input to a trajectory just coming close to the target orbit.

The proposition of controlling chaos suggested that the existence of chaotic dynamics can become a great advantage opposite to what one expected. Ott, Grebogi, and Yorke simultaneously offered a mathematical implementation of the controlling chaos, which is frequently called the OGY method consisting of their initial letters [22]. The OGY method is based on the construction of Poincaré map and its linearized one, which are fundamental tools of the dynamical system theory. As shown in Fig. 1.1, behavior of a system evolving continuously in time in the phase space is translated as behavior of a sequence of points on a cross section of the phase space. The cross section is called Poincaré section. One can then define a map, or discrete dynamical system, called Poincaré map, giving the sequence of points and analyze the map instead of the original continuous dynamical system or vector field. Since a chaotic trajectory approaches an unstable periodic orbit along its stable manifold on the Poincaré section, a small perturbation to the system is able to make the trajectory move on the stable manifold. The trajectory then converges to the periodic orbit along the stable manifold, if the procedure is achieved before the trajectory turns away from the orbit along the unstable manifold. The perturbation simultaneously goes to zero, since the target orbit is intrinsic to the system. The appropriate perturbation is calculated with a linearized map approximating the Poincaré map in the neighborhood of a target orbit.

The OGY method was successfully applied to stabilization of a magnetoelastic ribbon [28], thermal convection loop [29]. A modified method, called the occasional proportional feedback (OPF) method, also stabilized a laser system [30], chemical chaos [31], and even cardiac arrhythmias [32]. The field of controlling chaos has tremendously developed through the 1990s [26]. Several advanced methods have been designed to change chaotic motion of a system to periodic one by stabilizing unstable periodic orbits embedded in chaotic attractors [30, 31, 33–35]. It is interesting to note that the field of controlling chaos was opened not by control engineers but by physicists. One cause may be that the unpredictable nature of chaotic dynamics, termed as *sensitive dependence on initial conditions*, was too emphasized in the early days of research. In the late 1980s, the trend of research passed away especially in control engineering [36]. The OGY method then brought the philosophy of control to physicists and was also reimported to the engineering fields. It is now well known that the OGY method is relevant to the pole assignment method in the modern control theory [36].

1.2 Time-delayed feedback control

The time-delayed feedback control was also proposed by a solid state physicist, Pyragas [34] in 1992 and has attracted much interest of researchers up to the present [37, 38]. The strategy of this control method is to employ the error signal between the present output signals and the past ones measured in a chaotic system, as shown in Fig. 1.2. It was surprising especially for control engineers that the time delay in the feedback loop contributes to stabilization of unstable periodic orbits. The time delay, called *dead time* in the control engineering, often make the stability of control systems lost and therefore has been an anathema to control engineers long before [39–44]. The time delay had been considered as a cause of undesired oscillation and chaos also in other fields [13, 15, 18, 45–47].

Pyragas proposed two different control methods in his seminal paper [34]. His motivation was to extend the OGY method as a continuous time control. This is because the OGY method and its extension are based on the construction of the Poincaré map and therefore involves discretization of continuous dynamical systems. Since the control signal is input intermittently on the specific cross section, the controlled systems often diverge to occasional bursting motion again due to external disturbances and noises [22]. The first method, therefore, employed a time continuous external reference $r(t)$, time series of a target unstable periodic

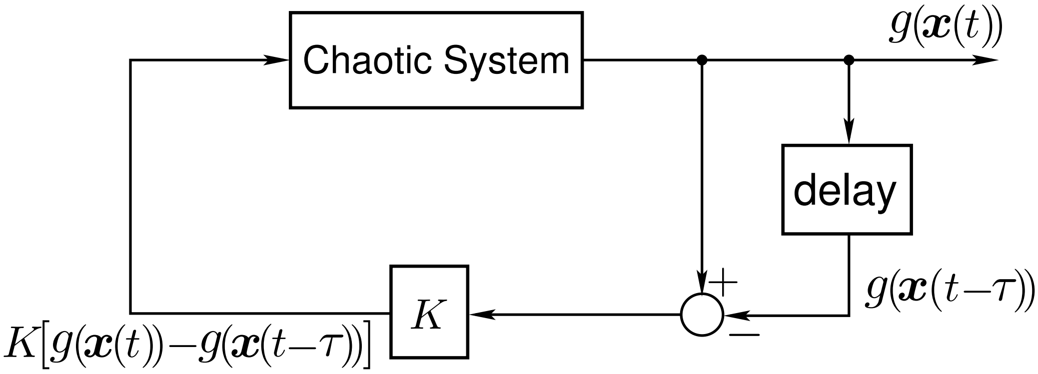

Figure 1.2: Control block of time-delayed feedback control [34]. A chaotic system one wishes to control can be stabilized by feedback of the present output of the system $g(\boldsymbol{x}(t))$ and the past $g(\boldsymbol{x}(t-\tau))$ without any external reference. The time delay τ for the past output is precisely adjusted to the period T of a target unstable periodic orbit embedded in a chaotic attractor. The control input converges to zero as the chaotic system is stabilized at the target period-T state. K is feedback gain, which is an important control parameter to determine intensity of control.

orbit, to generate a feedback signal $K[r(t)-g(\boldsymbol{x}(t))]$. He aimed to make the control robust to external disturbances and noises by continuous control input. In the second method, he replaced the external reference $r(t)$ to the internal delayed output $g(\boldsymbol{x}(t-\tau))$. The delay time are adjusted to the period of the target unstable periodic orbits, so that the error signal converges to null when the controlled system is stabilized to a target unstable periodic orbit. Since the strategy is only relying on the time series of measurable output signals, the control method is a practical way to achieve continuous control of chaotic systems. The control method does not need external reference, the exact model of a chaotic system, identification of its parameters, and complicated processing for reconstruction of the underlying dynamics.

The feasibility of the second method, now called *the time-delayed feedback control*, has experimentally verified mainly in the 1990s for a wide variety of chaotic systems, including electronic circuits [48, 49], laser [50], a gas charge system [51], mechanical oscillator [52], and chemical systems [53, 54], plasma [55, 56], Taylor-Couette flow [57]. It should be emphasized that the time-delayed feedback control can work well in systems with fast time scale [48, 49]. The control method has been applied to a high frequency electric circuit of 10 MHz [49] and a laser system of 365 kHz [50]. In the theoretical side, linearization based approaches have been effectively applied to analyze the stability of target unstable periodic orbits under control input [58–65]. The stability analysis had many applications. Among them, derivation of the odd number condition is well known to give an inherent limitation concerning a class of unstable periodic orbits which cannot be stabilized by the control method. The condition was first derived for discrete time control [66] and subsequently extended to continuous time control [59–61]. Pyragas has recently improved the strategy to overcome this limitation [64]. An extended version of the time-delayed feedback control was also proposed to improve the control performance. Socolar *et al.* proposed a generalized version of the control method using many previous states of a system [49]. Nakajima presented a method for automatic adjustment of delay time and feedback gain [67]. Just reported influence of additional latency in the feedback loop on control performance [62].

In spite of these excellent experimental and theoretical results, there still remain open problems on clarification of the control performance [63]. In particular, there have been very few discussions on the global dynamics of controlled systems and related control characteristics [68, 69]. Dynamics of a controlled system is governed by the global phase structure in function space. The controlled system is described by a difference differential equation due to time delay introduced in the feedback loop [70, 71]. The controlled system is, therefore, treated as an infinite dimensional dynamical system and this causes difficulty in the theoretical treatment of the control performance. No systematic design of feedback gain has been given so far due the the same reason. One important result related to the global dynamics is the experimental study by Hikihara and Ueda on the stabilization of chaos in a magnetoelastic beam [68]. They addressed that the transient dynamics was not so simple as explained by stability analysis. They attempted to understand what occurred in the transient state by treating the dynamics of a system with time delay as a kind of spatio-temporal dynamics.

One serious and motivating problem related to the global dynamics is the possibility of the coexistence of global chaotic dynamics and locally stable target orbits in controlled systems. Since the stability is a only local property of a system, it is natural to suspect that chaotic dynamics of the system persists against control input due to its global nature. The behavior of the controlled system is then kept chaotic, even if the control parameters are appropriately chosen from the viewpoint of stability of target orbits. Of course, the coexistence does not cause any contradiction in physics; however, it is never consistent with the purposes of almost every engineering applications of the time-delayed feedback control, or controlling chaos more generally. The chaotic dynamics persisting in a controlled system makes the transient state irregular and too long, and complicates the domain of attraction for target orbits. The controlled system then easily reverts to a chaotic state even under control, since engineering systems are often exposed to noise, disturbance, and occasional or transient change of the parameters of the system. Once the controlled system is driven out of the neighborhood of a locally stable orbit, the system shows irregular and unpredictable motion because of the coexisting chaotic dynamics governing the global behavior of the system. This chaotic motion continues before the system comes sufficiently close to the stable target orbit again.

The problem presented above is obviously beyond the scope of traditional linearization based analyses and has not been suggested yet. The problem therefore implies that a *missing-link* still exists between the previous theoretical explanation based on linearization and the successful results in the past experiments. The global dynamics of a controlled system is a candidate for it and of great importance related to the fundamentals and practice toward the engineering application of the time-delayed feedback control.

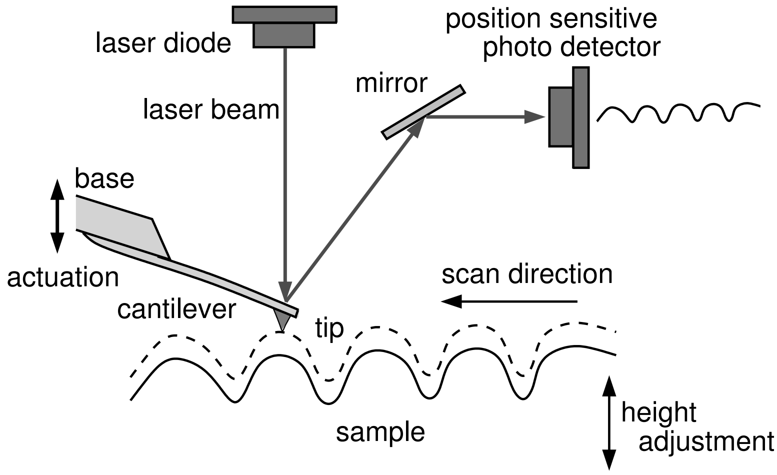

Figure 1.3: Schematic diagram of atomic force microscopy. A sample surface is scanned by a microcantilever sensor with a sharp tip. The microcantilever is deflected by the interaction force between the tip and surface. When the surface is scanned, the distance between apex of tip and surface is kept constant with a positioning device, which adjusts the vertical position of the surface, so that the microcantilever deflection is maintained constant. The time series of signal applied to the positioning device provides a topography of the surface. The deflection is measured by the optical lever method [72] in standard device configuration. In the dynamic-mode, or the dynamic force microscopy, the microcantilever is vibrated at the resonance frequency and the shift of resonance frequency is maintained instead of the deflection.

1.3 Nonlinear dynamics and chaos in nanoengineering systems

The field of micro and nanotechnology, whose importance was early emphasized by Feynman in 1959 [73], are one of the most constantly and greatly advancing fields today and will be so over the 21st century [74]. Although the field is a new and little explored by nonlinear theory, recent trailblazing works have shown that nonlinear dynamics and chaos appear also in this new field [75–82]. The strategy of controlling chaos are now waiting for being applied and thus the novel application to a nanoengineering system called dynamic force microscopy (DFM) is presented in this dissertation.

The atomic force microscopy (AFM) has to be mentioned before describing the DFM, which is one of the major operating modes of the AFM. The AFM was invented in 1985 by Binnig *et al.* [83] four years after the Nobel Prize invention of the scanning tunneling microscopy (STM) in 1981 [84]. Both the AFM and STM are members of the scanning probe microscopy (SPM) family, which enables us to image surfaces with a probe that scans the samples. The image is obtained by a raster scan of the sample surface and recording the interaction between the probe and sample as a function of position of the probe. The fundamental difference between the two methods is that the AFM is based on force sensing and thereby able to image insulating samples as well as conducting and semiconducting specimens. On the other hand, the STM cannot image insulating samples in principle, since the STM detects the tunneling current flowing the probe and surface. A schematic diagram of the AFM is illustrated in Fig. 1.3. The probe of AFM is a microfabricated cantilever with a extremely sharpened tip at its free end. The microcantilever is significantly deflected by a tiny intermolecular or interatomic force acting between the apex of tip and surface. The interaction force is detected by measuring the deflection of the microcantilever. The AFM has a wide variety of applications due to its feasibility to the insulating samples including biological and organic samples.

The DFM is one of the operating modes of the AFM and also called the dynamic-mode AFM. The DFM has been highly developed for this nearly two decades [74, 85, 86]. The microcantilever is mechanically vibrated at the resonance frequency in the DFM [87, 88]. The topography of the sample surface is imaged by raster scan of the surface with keeping the vibration or resonance frequency of the microcantilever constant. One great advantage is that the damage of sample surfaces is significantly reduced as compared to the conventional AFM, now called *contact-mode* AFM. Adhesion of the tip to surfaces is also avoided by vibrating the microcantilever. Another is that force sensitivity is much improved using microcantilever with high quality factor. A broad range of samples have been observed so far in the resolution of atomic or molecular scale without damaging samples including semiconducting [89–91], organic [92], and biological samples even in liquids [93, 94]. In addition, versatile applications of the vibrating microcantilever have been presented, such as profiling of surface properties [95–97], manipulation of single atoms and molecules [98], and control of surface structures [99]. These excellent works allow us to expect that the DFM becomes a key technology for nanoscience and nanoengineering.

On the other hand, growing interests in the physical origin of high resolution imaging have highlighted the nonlinear dynamics of microcantilever sensors vibrating near sample surface [100–105]. In particular, much attention has been paid for microcantilevers in the DFM with amplitude modulation detection (AM-DFM) or tapping mode AFM [87, 106]. The tip of a microcantilever is exposed to a highly nonlinear force in an operating range of AM-DFM [107, 108]. As a result, a bistable behavior occurs in the proximity of sample surfaces [109]. The involving jumping and hysteresis phenomena cause sudden and discontinuous transition of imaging characteristics [107]. In addition, it was reported that the microcantilever exhibits subharmonic oscillation, period-doubling bifurcation [110, 111], and chaotic oscillations [78–82]. The resulting oscillation modes may reduce the force sensitivity of AM-DFM due to undesirable subharmonics and wide spread frequency spectrum, which are neglected in the standard device configuration of the AM-DFM. As for the chaotic oscillation, the operating range of the AM-DFM may be also limited by non-periodic and irregular motion of the microcantilever. It is therefore significant to develop control techniques for microcantilever oscillations for improving the performance of AM-DFM. In this context, some motivated research groups have already proposed application of control techniques to microcantilever oscillation [78, 79, 112].

The time-delayed feedback control described in the previous section is a promising control method to stabilize the chaotic oscillation of microcantilevers. The features of the control method allow us to implement it without identification of parameters of each microcantilever; the parameters such as spring constant are only given as nominal values and often so different from the true value. No analysis on the nonlinear dynamics is needed and only the driving frequency of AM-DFM has to be known to adjust the delay time. The feasibility to high frequency oscillation is also an important advance, since the microcantilever is typically vibrated around 10 kHz to 300 kHz. From the viewpoint of measurement, it is worth noting that no parameter of a microcantilever is modified after control is achieved. In particular, the quality factor is not changed in the steady state and thereby the force sensitivity of AM-DFM is maintained even under control input. This is essentially different from a control method introducing the damping to the oscillation proposed in Refs. [78, 79]. The control method stabilizing the intrinsic orbit of the system thus should be developed from the viewpoint of measurement.

1.4 Purpose and overview of thesis

The background of research described above now enables us to state the two purposes of this dissertation organized by eight chapters. The rest of this section is devoted to explaining the purposes and the structure of this thesis.

The first purpose is to understand the fundamental mechanism of controlling chaos by time-delayed feedback control. In order to achieve this purpose, one must clarify the global phase structure in function space, as emphasized in Section 1.2. In this dissertation, the two-well Duffing system under control is investigated chiefly numerically. The two-well Duffing system is a two-dimensional nonautonomous system, which was originally derived as a model of the first-mode vibration in the magnetoelastic beam system [14]. The global dynamics of the two-well Duffing system is described by a two-dimensional map and it was well analyzed by Moon and Holmes [14], and also by Ueda *et al.* [113]. In addition, the time-delayed feedback control of chaos in the magnetoelastic beam was experimentally achieved by Hikihara and Kawagoshi [52]. These excellent works provide a basis for developing our discussion in this dissertation. Stabilization of the two-well Duffing system is also related to elimination of chaotic vibration from mechanical systems. The results obtained in this dissertation thus can give important knowledge toward engineering applications of the time-delayed feedback control. A part of the results are also generalized based on mathematically tractable properties extracted from the two-well Duffing equation.

Chapters 2 to 6 are devoted to achieving the first purpose. Chapter 2 is a preliminary for the following chapters. The chapter firstly gives a general description of the time-delayed feedback control proposed by Pyragas. The two-well Duffing system is then introduced and its dynamics is summarized based on the previous literatures. The systems under control are described by the differential difference equations, which are a special and important class of the retarded functional differential equations (RFDEs). Mathematical treatment of the systems with time delay are reviewed based on the theory of RFDEs. The theory for periodic systems with time delay is summarized for the purposes of this dissertation.

Chapter 3 numerically investigates the multiple steady states and their bifurcation in the controlled two-well Duffing system as a first step to clarifying the global dynamics of the controlled system. Domains of control parameters causing the multiple steady states are examined by using a parameter plane with respect to feedback gain and onset time of control. The multiple steady states are caused due to the presence of stable orbits coexisting with the target orbits. The investigation on the bifurcation and origin of these coexisting orbits is the basis for the investigation in the following chapters.

Chapter 4 discusses the domain of attraction for target orbits in function space based on the results in Chapter 3. Boundary structures of the domain are numerically examined by giving a perturbation to initial conditions located near the boundary. The boundary structures in function space are displayed in a parameter plane related to the perturbation. We reveal different boundary structures including a self-similar structure. In particular, the persistence of the original chaotic dynamics in the controlled system is suggested by a quite complicated boundary structure arising when trying to stabilize one of the two target orbits selectively.

Chapter 5 is concerned with the global phase structure of the controlled system. The global phase structure in function space is directly probed with a global unstable manifold of an unstable periodic orbit. We show that complicated dynamics in infinite dimension suggested in Chapter 4 is caused by the coexistence of the original chaos producing structure and locally stable target orbits in the controlled system. The coexistence fully explains the mechanism that causes long and irregular transient dynamics and complicates domain of attraction for the target orbits. On the other hand, it is also shown that the global phase structure is so simplified and then no chaotic dynamics is observed, as the feedback gain is increased. We show the control performance is much improved due to the simplification of the global structure for large feedback gain.

In Chapter 6, the results in Chapter 3 and Chapter 5 are generalized as the features of the global dynamics in a periodic system under control. Revisit to the results in the previous chapters gives a clue to generalization. It is suggested that the problem of the global change from the original chaos producing to the simplified structure is reduced to that of the annihilation and degeneration of the non-target unstable periodic orbits from the controlled systems. The annihilation and degeneration of the non-target orbits are then generalized to a periodic system under control incorporating the harmonic balance method. A typical scenario of the change of global structure for increasing feedback gain is characterized and then a promising explanation is given to the ability and performance of the time-delayed feedback control from the viewpoint of global dynamics.

The second purpose of this dissertation is to present the novel application of this control method to the chaotic oscillation of microcantilevers in the DFM. Chapter 7 is devoted to this purpose. The possibility of the application is numerically discussed based on the mathematical model of a microcantilever proposed by Ashhab *et al.* [79] and numerical results by Basso *et al.* [80]. Control input is additionally applied to the model and then stability analysis of a target orbit estimates the domain of control parameters that achieves stabilization of the target unstable periodic orbit. Using the same approach, we also discuss improvement of transient response of oscillating microcantilever sensors. Since the quality factor is maintained in the steady state of the control system, the improved transient response allows us to accelerate the scanning rate of the AM-DFM without reducing their force sensitivity. We also discuss the suppression of another route to chaos, called *grazing bifurcation*, recently experimentally suggested by Hu and Raman [82].

Chapter 8 is the final chapter summarizing the conclusions and future directions of this dissertation.

Chapter 2

Two-well Duffing system under time-delayed feedback control

The two-well Duffing system under the time-delayed feedback control is investigated numerically and analytically from Chapter 3 to Chapter 6. In this chapter, the time-delayed feedback control and related general topics are introduced and summarized as preliminaries to the following chapters. Roles of the time delay inserted in the feedback loop are emphasized. The system under control is described by a difference differential equation and their mathematical treatment is summarized based on the theory of RFDEs. A discrete dynamical system on function space is derived from the time periodic difference differential equations. Supplemental remarks on the time-delayed feedback control are also given.

2.1 Fundamentals of control method

2.1.1 General description

This chapter begins by providing a general description of the time-delayed feedback control. We consider the application of the control method to n-dimensional continuous dynamical systems. Although this setup is enough to achieve the purpose of this and later chapters, it is noted that the control method has been extended to other class of the dynamical systems such as maps (discrete dynamical systems) and spatially extended systems.

A n-dimensional dynamical system is described by an ordinary differential equation including the input and output relation as follows:

$$\begin{cases} \dfrac{\mathrm{d}\boldsymbol{x}}{\mathrm{d}t} = \boldsymbol{f}(t,\, \boldsymbol{x},\, \boldsymbol{u}) \\ \boldsymbol{y} = \boldsymbol{g}(\boldsymbol{x}), \end{cases} \tag{2.1}$$

where t denotes the time, $\boldsymbol{x}$ the n-dimensional state of the system, $\boldsymbol{u}$ the m-dimensional control input, and $\boldsymbol{y}$ the p-dimensional output of the system. The original, or uncontrolled, dynamics of this system is modeled under $\boldsymbol{u}(t) = 0$. The uncontrolled system has its own dynamics, which is here assumed to yield a chaotic attractor. The internal couplings between the input and the state, and also between the state and the output are specified in the description of $\boldsymbol{f}(t,\, \boldsymbol{x},\, \boldsymbol{u})$ and $\boldsymbol{g}(\boldsymbol{x})$, respectively. The full state $\boldsymbol{x}$ cannot be directly obtained in practical situation. In addition, identification of $\boldsymbol{f}(t,\, \boldsymbol{x},\, \boldsymbol{u})$ and $\boldsymbol{g}(\boldsymbol{x})$ is not easy in reality.

As first suggested by Pyragas, unstable periodic orbits embedded in chaotic attractors can be stabilized by using continuous feedback of the error between the present system output and the past one [34]. The chaotic attractor is assumed to include unstable period-T orbits to be stabilized. Control input is then given as follows:

$$\boldsymbol{u} = K[\boldsymbol{g}(\boldsymbol{x}_\tau) - \boldsymbol{g}(\boldsymbol{x})], \tag{2.2}$$

where $\boldsymbol{g}(\boldsymbol{x}) = \boldsymbol{g}(\boldsymbol{x}(t))$ denotes the current output and $\boldsymbol{g}(\boldsymbol{x}_\tau) = \boldsymbol{g}(\boldsymbol{x}(t - \tau))$ the past one. τ is the delay time adjusted to T, that is, the period of the target orbits. $\boldsymbol{u}(t)$ converges to zero if a solution goes to a target orbit. Since $\boldsymbol{u}(t) = \boldsymbol{0}$ implies $\boldsymbol{x}(t-T) = \boldsymbol{x}(t)$, the stabilized orbit coincides with one of the target orbits inherent to the original system. Another unstable periodic orbit can be chosen as a target orbit by simply adjusting the time delay. K is m times p matrix denoting feedback gain. The feedback gain governs the stability of target orbits under the precise adjustment of time delay. However, its systematic design has not been formulated at the present stage.

One great advantage enabled by the time delay is that the control method can be implemented to experimental systems without their exact models and reconstruction of underlying dynamics from experimental data. Identification of a model is not an easy task in general. Moreover, the parameters of a system are often varied by replacing components of the system and changing operating conditions. Time series analysis, such as delay embedding, has to be alternatively performed to reconstruct the dynamics, if the model is not fully identified. On the other hand, only the period of the target unstable periodic orbits is required for the time-delayed feedback control, since the control input $\boldsymbol{u}(t)$ in Eq. (2.6) just relies on the instantaneous value of the measurable output. Without any priori or real time processing, the control signal $\boldsymbol{u}(t)$ is simply obtained by the difference of output signals. The control method has been, therefore, successfully applied to many experimental systems [48–57].

On the other hand, theoretical treatment of the controlled systems becomes much more complicated due to the time delay inserted in the feedback loop. Since a controlled system is described by a difference differential equation, one has to treat the dynamics in function space; the phase space of the system is infinite dimensional. The detail of this topic is explained in Section 2.3.

2.1.2 Theoretical limitation

One thing that should be kept in mind is that the control method has an inherent limitation, which is characterized by a theoretical condition called *the odd number condition*. The odd number condition gives a class of unstable periodic orbits which cannot be stabilized. This limitation is stated as follows [60]:

Any hyperbolic unstable periodic orbit cannot be stabilized by the time-delayed feedback control, if the orbit satisfies the odd number condition, namely, the orbit has an odd number of real characteristic multipliers greater than unity.

The odd number condition was firstly introduced by Ushio for discrete dynamical systems [66] and subsequently generalized for continuous systems by Nakajima *et al.* [59, 60]. Just independently found essentially the same limitation [61]. The odd number condition gives a severe limitation to the application of the control method. Several modified methods have been thus proposed in order to overcome this limitation [64, 114, 115].

2.2 Two-well Duffing system under control method

2.2.1 Mathematical model

The Duffing system is a two dimensional non-autonomous system originating in a model of synchronous machines [116]. Among a variety of its applications, the two-well Duffing system was derived by Moon and Holmes as a model of the first-mode vibration in the magnetoelastic beam system shown in Fig. 2.1 [14]. The two-well Duffing system under the control method is numerically and analytically investigated through the Chapter 3 to the Chapter 6.

The two-well Duffing system controlled by a scalar signal $u(t)$ is given as follows:

$$\frac{\mathrm{d}}{\mathrm{d}t}\begin{bmatrix} x \\ y \end{bmatrix} = \begin{bmatrix} y \\ -\delta y + \alpha x - \gamma x^3 + A\cos\omega t \end{bmatrix} + \boldsymbol{b}u, \tag{2.3}$$

where x and y denote the displacement and velocity of the system, respectively. $\boldsymbol{b}$ denotes a two dimensional constant vector concerning coupling between control input $u(t)$ and the state variables. From Eq. (2.4), $u(t)$ is determined by the difference between the current output and the past one of the system as follows [34]:

$$u = K[g(x_\tau,\ y_\tau) - g(x,\ y)], \tag{2.4}$$

where τ is time delay, K feedback gain. $g(x,\ y)$ and $g(x_\tau,\ y_\tau)$ imply the present and past scalar output, respectively. The onset time of control t_0 is a substantial control parameter, which determines the initial condition of the controlled system. The

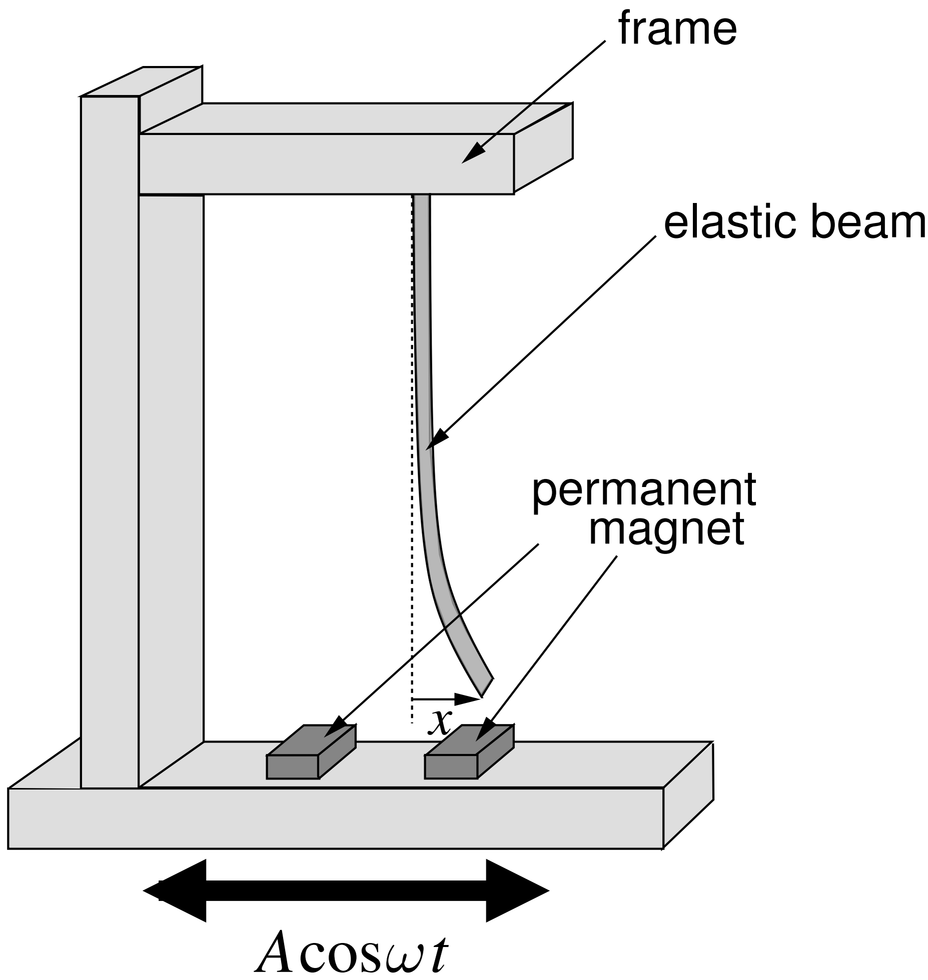

Figure 2.1: The magnetoelastic beam system proposed by Moon and Holmes [14]. The system is composed of a frame, cantilevered ferromagnetic beam, and two permanent magnets. The beam is buckled by the magnets symmetrically-placed below the free end of the beam. The magnets are located so that the beam has three equilibrium positions in the unforced state. The two of them are stable buckled positions and the other is an unstable neutral position between the two magnets. In the figure, the beam is buckled by the right magnet. Chaotic vibration of the beam is observed, when external sinusoidal force is applied to the system. The beam exhibits non-periodic and irregular transition between the three equilibrium positions as shown in Fig. 2.2. The chaotic vibration of the beam is well reproduced by the two-well Duffing equation, which describes the first-mode vibration of the beam. x denotes displacement of the beam.

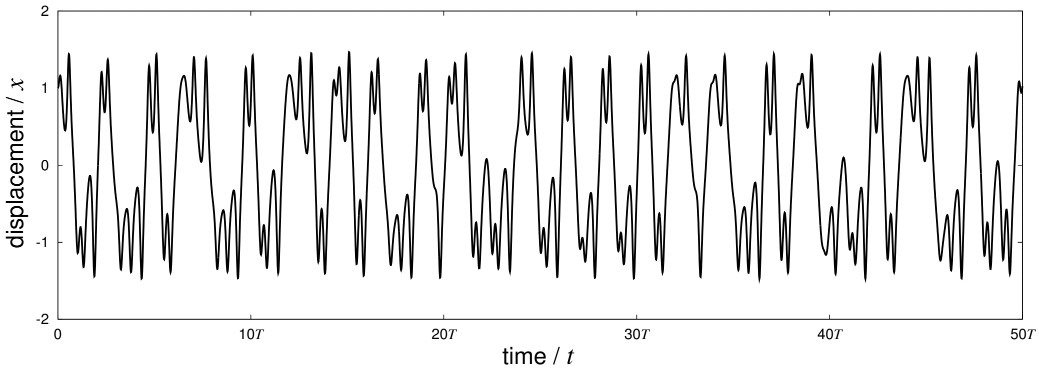

Figure 2.2: Chaotic oscillation in two-well Duffing system.

initial condition at t_0 consists of the following initial values and initial function:

$$\begin{cases} x(t_0) & = x_{t_0} \\ y(t_0) & = y_{t_0} \\ u_{t_0}(\theta) & = u(t_0 + \theta)\,;\ \theta \in [-\tau,\ 0). \end{cases} \tag{2.5}$$

In this paper, we identify the initial condition with a segment of the chaotic trajectory $[\,x(t) \quad y(t)\,]^T$; $t \in [t_0 - \tau,\ t_0]$ generated by Eq. (2.3) under $u(t) = 0$. The reason is a specific initial condition described as Eq. (2.5) is essentially transformed from the segment of the chaotic trajectory through Eq. (2.4) without loss of generality.

The implementation of the control method is specifically described by the coupling $\boldsymbol{b}$ and output signal $g(x,\ y)$. Two simple types of implementation are here introduced. One is *velocity feedback control* specially given by replacing $\boldsymbol{b}$ with $[\,0 \quad 1\,]^T$ and $g(x,\ y)$ with y in Eq. (2.3). The velocity feedback control employs the velocity component for the control signal. The other is *displacement feedback control* represented by Eq. (2.3) under $\boldsymbol{b} = [\,1 \quad 0\,]^T$ and $g(x,\ y) = x$. The displacement feedback control uses the displacement component for the control signal.

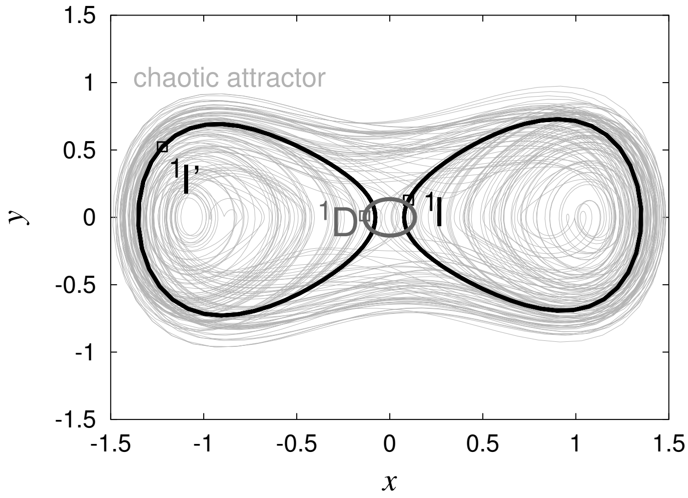

Figure 2.3: Chaotic attractor in two-well Duffing system [113]. $^1\mathsf{I}'$ and $^1\mathsf{I}$ are inversely unstable periodic orbits of target, which are stabilized under sufficiently large feedback gain. $^1\mathsf{D}$ is a directly unstable periodic orbit, which cannot be stabilized due to the odd number condition. The notation of $^1\mathsf{I}'$ and $^1\mathsf{I}$ are replaced to $^1\mathsf{S}'$ and $^1\mathsf{S}$, respectively, for reflecting stability change of the target orbits.

2.2.2 Chaos and target unstable periodic orbits

The investigation is hereafter performed for the system parameters $\alpha = 1.0$ and $\gamma = 1.0$. The forcing frequency is fixed at the normalized resonance frequency $\omega = 1.0 = 2\pi/T$ where T denotes the forcing period. The global dynamics of the two-well Duffing system was investigated by Moon and Holmes [14]. The results were subsequently reconfirmed and greatly extended by Ueda *et al.* [113]. A governing role in the global dynamics is played by the directly unstable periodic orbit denoted by $^1\mathsf{D}$ in Fig. 2.3. Since the stable and unstable manifolds of the orbit generate a homoclinic intersection in the cross section induced by stroboscopic mapping with period-2π, a chaotic invariant set exists in the original system (See, Fig. 2.4 obtained by a software package GAIO [117]). The global dynamics under these parameters was summarized in Ref. [113] . The dynamics was classified with respect to the damping coefficient δ and the forcing frequency A. δ and A

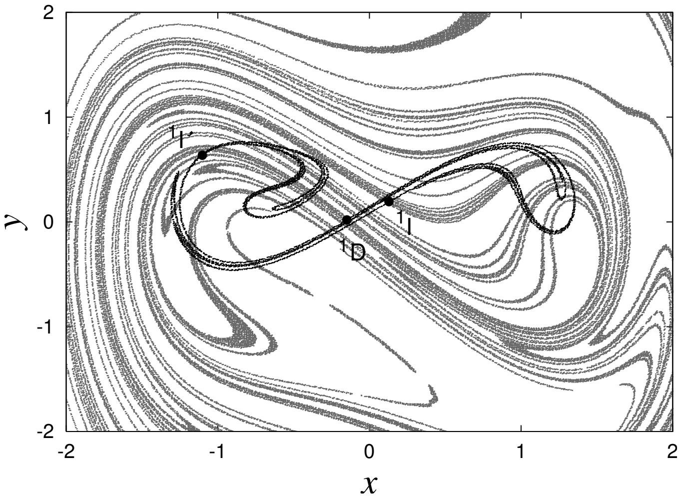

Figure 2.4: Transversal intersection of stable (gray) and unstable manifold (black) of $^1\mathsf{D}$ in two-well Duffing equation. The figure was obtained with GAIO, a software package for dynamical systems [117].

are fixed, so that the two-well Duffing system generates a chaotic attractor under the absence of the control signal. The chaotic attractor includes three unstable periodic orbits with period-2π [113], as shown in Fig. 2.3. Two of them, denoted by $^1\mathsf{I}$ and $^1\mathsf{I}'$, are classified as inversely unstable and the remaining $^1\mathsf{D}$ is directly unstable by the location of their characteristic multipliers in the complex plane [1]. The characteristic multipliers are obtained using the period-2π stroboscopic map. As target orbits for control, $^1\mathsf{I}$ and $^1\mathsf{I}'$ are selected in this paper. $^1\mathsf{I}$ and $^1\mathsf{I}'$ are easily stabilized under $\tau = T = 2\pi$ as shown in Fig. 2.5. It is noted that feedback of velocity signal was employed for experimental stabilization of the magnetoelastic beam by Hikihara and Kawagoshi [68]. In the following numerical study, we adopt the three parameter setups listed in Table 2.1. The time-delayed feedback

[1]This classification is based on the Levinson's classification of periodic solutions in *a system of class D, or a dissipative system for large displacement*. A periodic orbit in the system is called *inversely unstable*, if its two characteristic multipliers ρ_1 and ρ_2 satisfy the relation $\rho_2 < -1 < \rho_1 < 0$. The periodic orbit is called *directly unstable*, when its two multipliers have relation $\rho_1 > 1 > \rho_2 > 0$ [118].

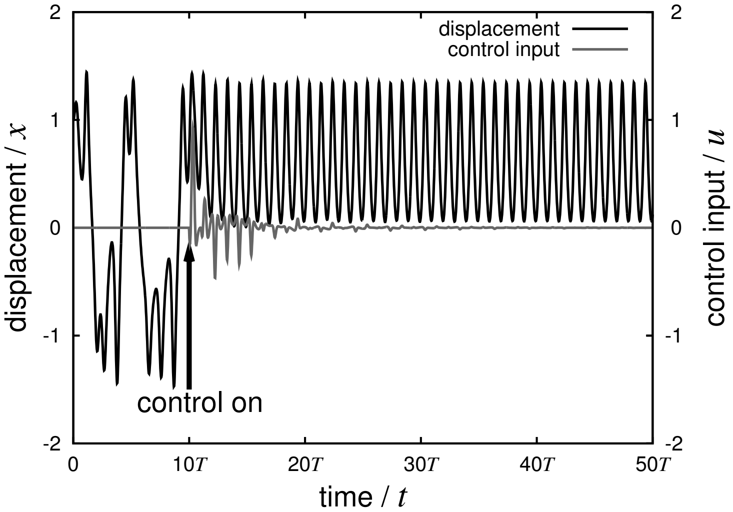

Figure 2.5: Stabilization of two-well Duffing system. τ is adjusted to $T = 2\pi$.

Table 2.1: Combination of the parameters and implementation of time-delayed feedback control for two-well Duffing system

Notation	Parameter (δ, A, ω)	Implementation
TV1	(0.3, 0.34, 1.0)	velocity
TV2	(0.16, 0.27, 1.0)	velocity
TD1	(0.46, 0.4, 1.0)	displacement

control is implemented with velocity feedback in the TV1 and TV2 cases, and the TD1 case employs displacement feedback. The parameter setups are only the difference between the TV1 and TV2. The initial conditions for the uncontrolled systems are adjusted to $[\, x \quad y \,]^T = [\, 1 \quad 0 \,]^T$ at $t = 0$.

2.3 Dynamics in function space

2.3.1 Difference differential equations

From the viewpoint of dynamical system theory, it is crucial that the phase space of the controlled system has infinite dimension due to the time delay included in the feedback loop. Substitution of Eq. (2.4) into Eq. (2.1) leads to a difference differential equation describing the whole dynamics of the controlled system as follows:

$$\frac{\mathrm{d}\boldsymbol{x}}{\mathrm{d}t} = \boldsymbol{f}(t,\ \boldsymbol{x},\ K[\boldsymbol{g}(\boldsymbol{x}_\tau) - \boldsymbol{g}(\boldsymbol{x})]). \tag{2.6}$$

A rough description is here given to elucidate the essential difference from the ordinary differential equations. We know well that only the initial value of $\boldsymbol{x}$ at initial time $t = t_0$ is specified to solve the initial value problem of the ordinary differential equations; however, one must give the value of $\boldsymbol{x}$ on the interval $[t_0 - \tau,\ t_0]$ for the initial value problem of Eq. (2.6), because the right hand derivative $\boldsymbol{f}$ at each time depends on $\boldsymbol{x}_\tau$ as well as $\boldsymbol{x}$. More precisely, the initial condition for Eq. (2.6) must be given by $\phi_{t_0}(\Theta) = \phi(t_0 + \Theta)$, $-\tau \leq \Theta \leq 0$. which belongs to $C = C([-\tau,\ 0],\ \mathcal{R}^n)$, the set of $\mathcal{R}^n$-valued continuous functions.

Figure 2.6 illustrates how a solution arises from an initial condition $\phi_{t_0}(\Theta)$. Let $\boldsymbol{x}_{t_0+i\tau}(\Theta)$ denote the solution on the interval $[t_0,\ t_0+i\tau]$ for $i = 1,\ 2,\ \cdots$. $\boldsymbol{x}_{t_0+\tau}(\Theta)$ is then uniquely determined from the initial data $\phi_{t_0}(\Theta)$. In the same way, $\boldsymbol{x}_{t_0+2\tau}(\Theta)$ for the next interval is uniquely obtained from the previously determined $\boldsymbol{x}_{t_0+\tau}(\Theta)$. The successive iteration of this process enable us to decide $\boldsymbol{x}_{t_0+(i+1)\tau}(\Theta)$ for each i positive integer based on the information of $\boldsymbol{x}_{t_0+i\tau}(\Theta)$ on the previous interval. This iteration process also implies that it is reasonable to define a map or discrete dynamical system $\mathcal{F}$ on C, which is infinite dimensional phase space, to analyze the dynamics of time-delayed feedback controlled systems. This section summarizes the more precise treatment of the difference differential equation, which is especially devoted to the time-delayed feedback controlled systems.

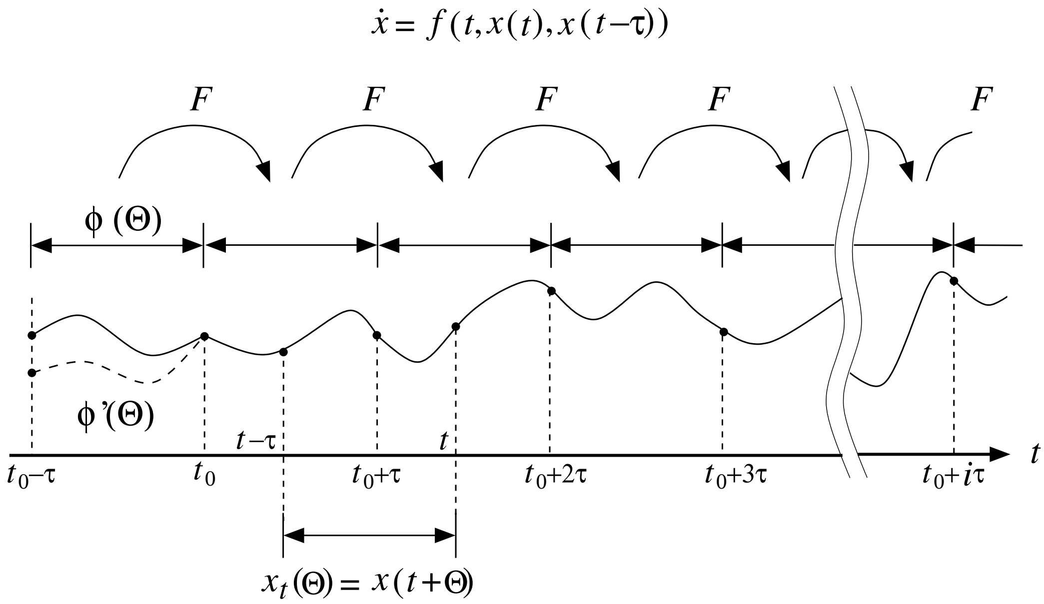

Figure 2.6: Schematic diagram of solution of difference differential equations. Θ varies on $[-\tau,\ 0]$. $\phi(\Theta)$ denotes an initial condition defined on the interval $[t_0-\tau,\ t_0]$ where t_0 is initial time. An unique solution on each interval $[t_0+i\tau,\ t_0+(i+1)\tau]$ is successively determined from the solution on $[t_0+(i-1)\tau,\ t_0+i\tau]$ for $i = 1,\ 2, \cdots$. The initial condition $\phi(\Theta)$ is used for $i = 0$. $\boldsymbol{x}_t(\Theta) = \boldsymbol{x}(t+\Theta)$ is the state of the system at time t. Two distinct initial conditions $\phi'(\Theta)$ and $\phi'(\Theta)$ may give the same solution in contrast to the ordinary differential equations.

2.3.2 Existence and uniqueness of solutions

The difference differential equation (2.6) constitutes a special class of the retarded functional differential equations, which will be denoted by RFDEs. The theory of the RFDEs has been well established [70, 71] and thus provides the fundamental framework to analyze systems under the time-delayed feedback control.

Suppose $\Omega \subseteq \mathcal{R} \times C$ is an open set and C denotes $C([-\tau,\ 0],\ \mathcal{R}^n)$, the set of $\mathcal{R}^n$-valued continuous functions defined on the interval $[-\tau,\ 0]$. C is a Banach space under the norm defined as $|\phi| = \sup_{-\tau\leq\Theta\leq 0} |\phi(\Theta)|$ for $\phi \in C$. For a given function

$\boldsymbol{F} : \Omega \to \mathcal{R}^n$, the relation below is said to be a RFDE on Ω:

$$\frac{\mathrm{d}\boldsymbol{x}}{\mathrm{d}t} = \boldsymbol{F}(t,\ \boldsymbol{x}_t), \tag{2.7}$$

where $\boldsymbol{x}_t = \boldsymbol{x}(t+\Theta)$ and belongs to C as a function of $\Theta \in [-\tau,\ 0]$. It is noted that $\boldsymbol{F}$ gives the right-hand derivative at $(t,\ \boldsymbol{x}_t) \in \Omega$. The RFDE (2.7) is reduced to the difference differential equation (2.6) based on the following relation:

$$\boldsymbol{F}(t,\ \phi) = \boldsymbol{f}(t,\ \phi(0),\ K[\boldsymbol{g}(\phi(-\tau) - \boldsymbol{g}(\phi(0))]), \tag{2.8}$$

The following results for the RFDE thus hold for Eq. (2.6). The validity for Eq. (2.3) follows under the same condition.

An assumption on $\boldsymbol{F}$ is here made that $\boldsymbol{F}$ is continuous and satisfies the Lipschitz condition for each compact set in Ω. This assumption is sufficient to prove the basic theorem on the existence and uniqueness of solutions. Continuous dependence of solutions on initial conditions and $\boldsymbol{F}$ is also proved under the same assumption. The solution through an initial condition $(t_0,\ \phi_{t_0}) \in \Omega$ is written as $\boldsymbol{x}_t(t_0,\ \phi_{t_0}) = \boldsymbol{x}(t+\Theta,\ t_0,\ \phi_{t_0})$, $\Theta \in [-\tau,\ 0]$. $\boldsymbol{x}_t(t_0,\ \phi_{t_0})$ then coincides with the initial condition ϕ_{t_0} at $t = t_0$, and satisfies Eq. (2.7) on the $[t_0,\ t_0 + A)$, $A > 0$; that is,

$$\begin{cases} \boldsymbol{x}_{t_0}(t_0,\ \phi_{t_0})(\Theta) = \phi_{t_0}(\Theta), \quad -\tau \leq \Theta \leq 0, \\ \dfrac{\mathrm{d}\boldsymbol{x}_t(t_0,\ \phi_{t_0})(0)}{\mathrm{d}t} = \dfrac{\mathrm{d}\boldsymbol{x}(t_0,\ \phi_{t_0})(t)}{\mathrm{d}t} = \boldsymbol{F}(t,\ \boldsymbol{x}_t), \quad 0 \leq t < A. \end{cases} \tag{2.9}$$

The derivative in Eq. (2.9), of course, implies the right-hand derivative. One should note that the uniqueness of solutions does not imply a solution of the RFDE never collide with another solution in Ω, in contrast to solutions of ordinary differential equations, which never intersect in the phase space. Two distinct initial conditions ϕ_{t_0} and ϕ'_{t_0} may have the same solution under the present assumption on $\boldsymbol{F}$, as shown in Fig. 2.6. The two solutions identically develop after their collision. The backward extension of solutions is therefore not unique for the RFDEs in general. The solution is continuable, particularly if the Lipschitz condition is satisfied.

2.3.3 Discrete dynamical systems on function space

If there is $T > 0$ such that $\boldsymbol{F}(t+T,\ \phi) = \boldsymbol{F}(t,\ \phi)$ for all $(t,\ \phi) \in \Omega$, then a discrete dynamical system on C is defined as a natural extension of stroboscopic maps for periodic ordinary differential equations. The solution operator of the RFDE $\mathcal{T} : C \to C$ is defined as follows.

$$\mathcal{T}(t,\ t_0)\phi_{t_0} = \boldsymbol{x}_t(t_0,\ \phi_{t_0}), \quad t \geq t_0. \tag{2.10}$$

$\mathcal{T}(t_0,\ t_0) = I$ is obvious and the uniqueness of solutions implies that $\mathcal{T}(t,\ s)\mathcal{T}(s,\ t_0) = \mathcal{T}(t,\ t_0)$ for all $t \geq s \geq t_0$. $\mathcal{T}$ is continuous as a consequence of the continuous dependence described above. $\mathcal{T}$ may not be one-to-one, since the uniqueness of a backward solution is not guaranteed. The periodic property of $\boldsymbol{F}$ implies $\mathcal{T}(t + T,\ t_0 + T) = \mathcal{T}(t,\ t_0)$ for all $t \geq t_0$. Define $\mathcal{F}_{t_0} : C \to C$ as $\mathcal{F}^0_{t_0} = I$, $\mathcal{F}^1_{t_0} = \mathcal{T}(t_0 + T,\ t_0)$, and $\mathcal{F}^k_{t_0} = \mathcal{F}^{k-1}_{t_0}\mathcal{F}_{t_0}$ for $k \geq 2$, then $\mathcal{F}^k_{t_0}$ is described by

$$\begin{aligned}
\mathcal{F}^k_{t_0} &= \mathcal{F}^{k-1}_{t_0}\mathcal{F}_{t_0} \\
&= \mathcal{T}(t_0 + (k-1)T,\ t_0)\mathcal{T}(t_0 + T,\ t_0) \\
&= \mathcal{T}(t_0 + kT,\ t_0 + T)\mathcal{T}(t_0 + T,\ t_0) \\
&= \mathcal{T}(t_0 + kT,\ t_0).
\end{aligned} \tag{2.11}$$

Since $\boldsymbol{F}$ is periodic, one can limit the initial time t_0 to the interval $[0,\ T)$. $\mathcal{F}_{t_0} : C \to C$ is referred to as a discrete dynamical system generated by the periodic RFDE. It is obvious that a periodic solution satisfying $\boldsymbol{x}_{t+kT}(t_0,\ \phi_{t_0}) = \boldsymbol{x}_t(t_0,\ \phi_{t_0})$ is translated as a fixed point on $\mathcal{F}^k_{t_0}$ for $k \geq 1$ or a period-k point on $\mathcal{F}_{t_0}$.

2.3.4 Linearized systems near periodic orbits

The linearized discrete dynamical system is derived in the same way based on the linear variational equation of the RFDE (2.7). Suppose that $\boldsymbol{F}$ has continuous p-th derivative, $p \geq 1$, with respect to $\phi \in \Omega$. One can then obtain the linear variational equation along a solution $\boldsymbol{x}_t(t_0,\ \phi_{t_0})$, $t \geq t_0$:

$$\frac{\mathrm{d}\boldsymbol{\xi}}{\mathrm{d}t} = \mathcal{D}_\phi \boldsymbol{F}(\boldsymbol{x}_t)\boldsymbol{\xi}_t, \tag{2.12}$$

where $\mathcal{D}_\phi$ denotes the derivative with respect to ϕ. $\mathcal{D}_\phi \boldsymbol{F} : C \to \mathcal{R}^n$ is a linear operator, which corresponds to the Jacobi matrix in the finite dimensional case. If $\boldsymbol{x}_t$ is a period-T solution, then $\mathcal{D}_\phi \boldsymbol{F}(t) = \mathcal{D}_\phi \boldsymbol{F}(t+T)$ for all t as a function of t. The same approach in the previous section therefore enables us to derive the linearized discrete dynamical system $\mathcal{DF} : C \to C$ generated by the linear variational equation (2.12). In the same way, $\mathcal{DF}^k$ are obtained for period-k solutions or period-k points.

One important thing is that $\mathcal{DF}$ is a completely continuous operator for $t \geq r$. The elemental theory of functional analysis therefore teaches us that the spectrum $\sigma(\mathcal{DF})$ of $\mathcal{DF}$ consists of only eigenvalues, or point spectra, $\sigma(\mathcal{DF})$ are at most countable, and zero is the only accumulating point of them.

2.3.5 Stability of periodic orbits

The stability of a period-kT solution in the RFDE (2.7) is the same as that of fixed point on the discrete dynamical system $\mathcal{F}_{t_0}^k$. The stability is characterized by the moduli of the eigenvalues of the linearized system $\mathcal{DF}_{t_0}^k$ in the neighborhood of the orbit. The orbit is stable, if the moduli of all the multipliers are less than unity, that is, located inside the unit circle. The orbit is unstable, if there is a multiplier having a modulus greater than unity. The eigenvalues of $\mathcal{DF}_{\sigma_0}^n$ are also called the characteristic multipliers of the orbit.

2.4 Remarks on practical aspects

Output signals have to be delayed to realize the time-delayed feedback controller experimentally. Analog delay lines and digital ones are available for making the target delay time. The former utilizing propagation delays of signals were used for systems with fast time-scale. Pyragas and Tamaševičius used a variable spiral line [48] and Socolar *et al.* employed standard coaxial cables [49] in their electronic circuits operated around the order of a few to ten MHz. Bielawski *et al.* delayed the light with a optical fiber by 2.74 μs. The latter are constructed by A/D(Analog to Digital), D/A(Digital to Analog) converters, and digital memories. Hikihara and Kawagoshi used a personal computer as memory for magnetoelastic beam oscillating at 16 Hz. Pierre *et al.* used FIFO(First In First Out) memory for making delay variable from 0.05 ms to 2 ms. Parmananda *et al.* obtained a computer with data acquisition card having 25 Hz sampling rate for their chemical experiment. The digital delay lines can have great flexibility for adjustment of parameters and well fit to other digital equipments, while it is difficult to apply the fast time-scale systems.

2.5 Supplemental remarks

In the theoretical side, linearization based approaches have been successfully applied to examine and improve the ability of the time-delayed feedback control. Stability of target orbits are one of the most important problem and has been studied in detail. The application extends from derivation of the odd number condition [59–61, 66], stability analysis of target orbits [61], calculation of domain of control [58, 61], influence of additional latency in the feedback loop [62] and so on. It is noted that several important results for discrete time control have been generalized to continuous time control, whereas discrete time control is out of the scope of this dissertation [119–121]. Many modifications of the original Pyragas method have been proposed so far. Among them, an extended control method proposed by Socolar *et al.* is well-known as *extended time-delayed autosynchronization* (ETDAS) as follows [49]:

$$u(t) = K\left[g(\boldsymbol{x}(t)) - (1-R)\sum_{k=1}^{\infty} R^k g(\boldsymbol{x}(t-k\tau))\right], \tag{2.13}$$

where $0 \leq R < 1$. The ETDAS utilizes many previous states of a chaotic system and is easily implemented by recursive input of the error signals. The ETDAS is particularly effective for stabilization of unstable periodic orbits with higher periods. Nakajima also presented a method for automatic adjustment of delay time and feedback gain [67]. The same approach as the time-delayed feedback control was experimentally applied to control of a chaotic absorption in thin YIG films by Ye and Wigen in 1995 [122]. A possibility of the very similar method using time delay to control helicopter rotor blades was proposed by Krodkiewsk and Faragher [123].

Chapter 3

Multiple steady states and bifurcations in controlled systems

As a first step to the global dynamics of controlled systems, this chapter investigates periodic solutions arising in the controlled two-well Duffing systems. The chapter begins with a motivating observation, which suggests the appearance of multiple steady states in the controlled systems. The possibility of the multiple steady states is then examined in a systematic way using a parameter plane with respect to feedback gain and onset time of control. Classification of many different initial conditions by resulting steady states shows coexistence of various stable orbits with the stabilized target orbits. The orbits coexisting with the targets are called *coexisting orbits* in this dissertation. The dynamical properties of the coexisting orbits are discussed on the basis of bifurcation theory. Bifurcation analysis elucidates the mechanism of stability loss and annihilation of the periodic orbits. It is also shown that the coexisting orbits originate from the unstable periodic orbits embedded in the chaotic attractor.

3.1 Motivation

Nonlinear dynamical systems, unlike linear systems, often have multiple steady states and thus different initial conditions lead to different steady states in general.

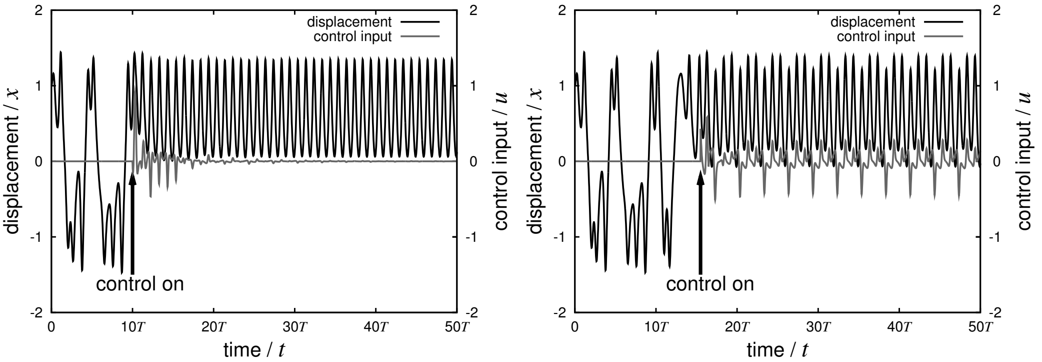

(a) t_0 = 10T (b) t_0 = 15.5T

Figure 3.1: An example of convergence to different periodic orbits in the TV1 case at K = 0.935. Black and gray lines show displacement and control input, respectively. (a) shows convergence to a target period-T orbit when t_0 = 10T and (b) to coexisting period-3T orbit for t_0 = 15.5T. Control is activated at the time pointed by an arrow in each figure. Displacement is irregular and non-periodic before the activation. In (a), control input converging to zero implies the stabilized orbit completely coincides with the target orbit in the chaotic attractor. In (b), control input keeps period-3T in the steady state, showing failure of control in the sense of controlling chaos.

An exception is not made for chaotic systems under the time-delayed feedback control. One can, in fact, readily confirm that solutions of the controlled two-well Duffing systems converge to different periodic orbits by numerical simulation. Each of the solutions goes to a different periodic orbit depending on onset time of control, which determines initial conditions for the controlled systems. For example, Fig. 3.1 shows two solutions which converge to different steady states. The solution in Fig. 3.1(a) converges to one of the two target period-T orbits, which completely coincide with the unstable periodic orbit denoted by ^{1}I in Fig. 2.3. The control input simultaneously goes to a negligible level, after the control was activated at the time pointed by an arrow. On the other hand, the solution in Fig. 3.1(b) converges to a period-3T orbit instead of the target orbits, when the onset timing is changed to another. Since the control input also remains period-3T in the steady

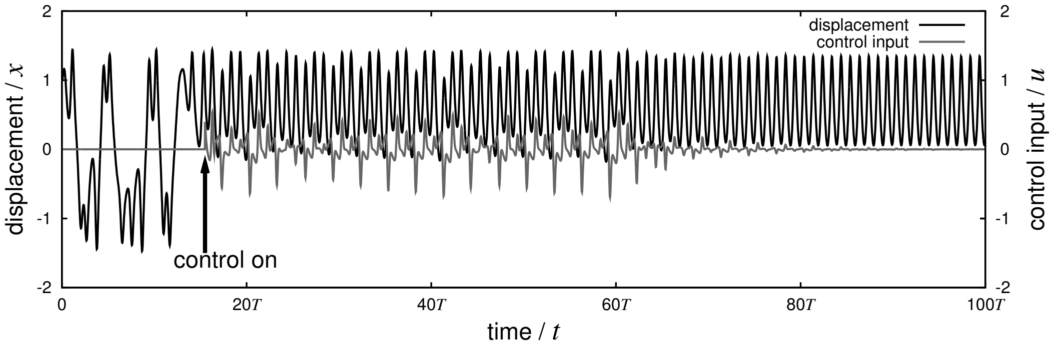

Figure 3.2: An example of transient behavior before convergence to target orbit. Control is turned on at the time pointed by an arrow. Both displacement and control input show transient behavior similar to the period-$3T$ motion observed in Fig. 3.1(b). The same parameters as Fig. 3.1 are used except $K = 0.865$.

state, the stabilized period-$3T$ orbit does not coincide with any unstable periodic orbit inherent to the original two-well Duffing system. The stabilized period-$3T$ orbit is a stable periodic orbit coexisting with the stabilized target orbits. One important problem proposed here is that convergence to such coexisting orbits obviously contradicts the purpose of controlling chaos. Control can fail due to the presence of stable coexisting orbits, which may be even chaotic.

Another problem is that transient dynamics is also affected by the presence of coexisting orbits and related phase structures. One example is shown in Fig. 3.2, where a motion similar to the period-$3T$ solution appears before the final convergence to the target orbit [1]l. The previously mentioned coexisting period-$3T$ orbit seems to be unstable in this case and therefore cannot emerge in the steady state; however there seems to be a transient phase in which the solution comes close to the unstable coexisting period-$3T$ orbit once and then turns from it. The transient dynamics is an important characteristic of controlled systems, but no explanation has been given to various transient behaviors arising in the time-delayed feedback controlled systems.

There exist few reports addressing multiple steady states [124–126] and transient dynamics [68]. These problems are directly connected to the global dynamics of controlled systems and obviously beyond the scope of the conventional linearization based approach. The coexisting orbits are solutions which make structures in the infinite dimensional phase space, whereas the target orbits exist in the original two dimensional space. The investigation of the coexisting orbits is therefore adopted here as the first step to approach the global dynamics in function space.

3.2 Orbits coexisting with targets

3.2.1 Onset timing, initial condition, and feedback gain

As shown in Fig. 3.3(a), an initial condition for a controlled system is determined as a segment of a chaotic trajectory, or a history of the system states, for each onset time of control. Since different initial conditions arise because of chaotic motion before starting control, onset time of control should be regarded as a substantial control parameter to select the steady state of the controlled system. The relationship between onset time and steady state must provide information on the dependence of steady state on initial conditions. In addition, feedback gain is also an important control parameter, which governs the stability of periodic solutions and also the global phase structures. A parameter plane with respect to onset time and feedback gain is thus defined to examine multiple steady states throughout this chapter.

When the control starts at the onset time t_0 under the feedback gain K, each of the determined initial conditions can be mapped to a point (t_0, K) on a coordinated parameter surface illustrated in Fig. 3.3(b). The surface runs along the chaotic trajectory developing from an initial condition (x_0, y_0) for the uncontrolled system and is extended in the direction of K-axis. Classification of points on the surface with resultant steady states enables systematic investigation of the dependence on initial conditions. Figure 3.3(c) is a schematic diagram of a part of the surface made flat for simplicity of visualization. A (σ_0, K)-plane covers the (t_0, K)-surface over the θ_0-th period, where θ_0 is a non-negative integer measured

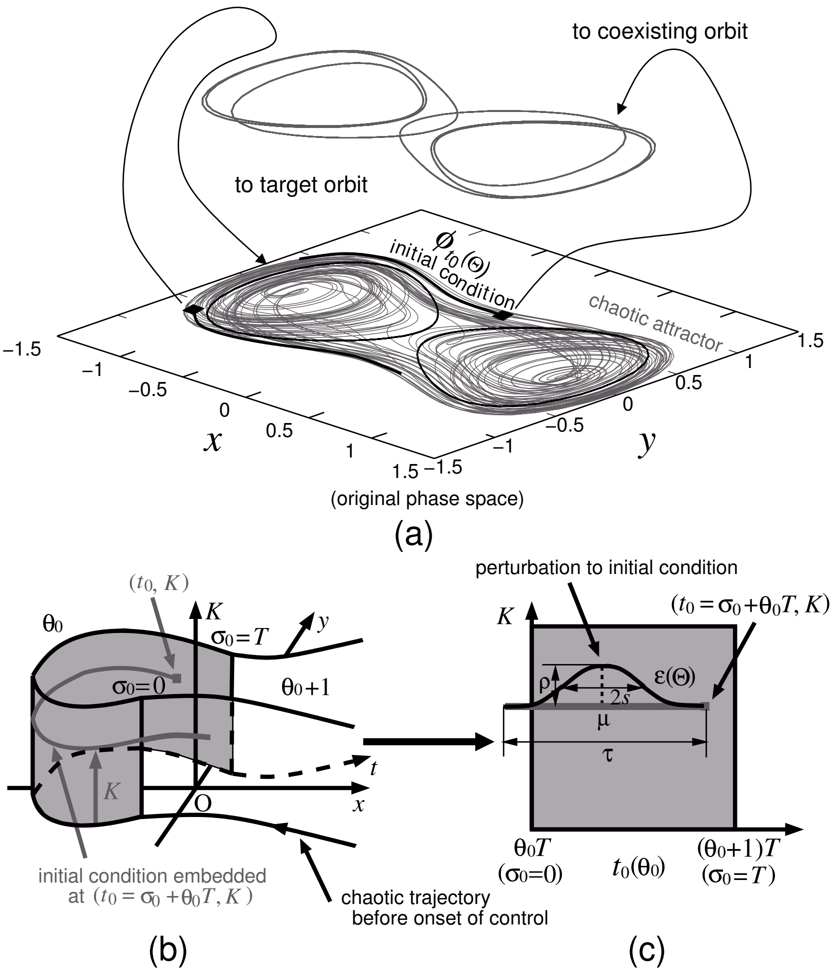

Figure 3.3: A schematic diagram of convergence to coexisting orbits (a) and initial conditions embedded in parameter surface (b) / plane (c) with respect to onset time and feedback gain. As shown in (a), the target orbits exist in the original two-dimensional phase space. In contrast, the coexisting orbits are stabilized in function space with significant control input. A surface in (b) displays a chaotic trajectory generated by the uncontrolled system; the surface is extended in the direction of feedback gain axis. An initial condition at the onset time t_0 under the feedback gain K is related to a point (t_0, K) in the surface. (c) shows (σ_0, K)-plane which covers (t_0, K)-surface from $t_0 = \theta_0 T$ to $t_0 = (\theta_0 + 1)T$ where θ_0 is non-negative integer and σ_0 is included in [0, T). A Gaussian-like curve in (c) shows a schematic diagram of perturbation employed for modifying initial conditions in Chapter 4.

by the period of the sinusoidal external force. σ_0 denotes the onset phase defined for the sinusoidal forcing and thereby is included in $[0, T)$. It is noted that, if the span of onset time of control is sufficiently large, one can expect that the corresponding series of (σ_0, K)-planes cover the whole of the original chaotic attractor in the sense that any chaotic trajectory visits arbitrarily close to a given point on the chaotic attractor in finite time. It is also mentioned that the (σ_0, K)-plane can be associated with the sensitivity of the dependence on initial conditions. An initial condition is slightly modified for each small shift of onset timing. All initial conditions are different due to the non-periodic oscillation before turning on the control.

Steady states obtained by control are classified by tones shown in Fig. 3.4. It is noted that the same tone is used for the steady states with the same period for simplicity of figures. In particular, convergence to the two target orbits $^1\mathsf{I}$ and $^1\mathsf{I}'$ are here denoted by the same toned point, whereas they are distinguished in the later chapter.

3.2.2 General features

The first thing to do is to grasp a general feature of the parameter planes with neglecting fine structures discussed later. The feature is here described only for the TV1 case, but one can observe the same feature in the other two cases. Figures 3.5 shows a series of (σ_0, K)-planes in the TV1 case: the two-well Duffing system with velocity feedback control at $(\delta, A) = (0.3, 0.34)$. The span of onset time of control covers from $\theta_0 = 12$ to $\theta_0 = 23$, i.e. the 12-th period to 23-rd with respect to the sinusoidal external forcing. The extraction for $\theta_0 = 18$ is expanded as Fig. 3.6. There seems to be roughly two different areas. The largest dominant region denotes the set of onset times and feedback gain values where the state of the controlled system converges to one of the target period-T orbits. The target orbits are, in fact, stable under feedback gain sufficiently large. The existence of this large domain proves the ability of the time-delayed feedback control and its robustness to onset times, or initial conditions. On the other hand, the solution

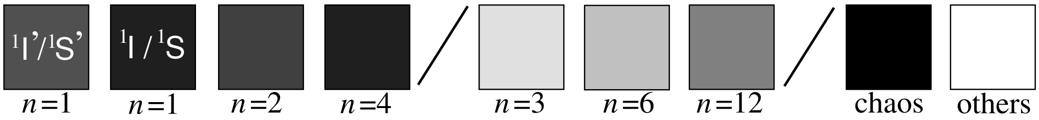

Figure 3.4: Classification of tones with period of steady states in onset time and feedback gain parameter space defined in Fig. 3.3. Each tone denotes convergence to a period-nT orbit.

can never be expected to converge to a target orbit in the black area below the dominant region. This implies the controlled system is chaotic under control. The reason is simply that the feedback gain is too low to change the stability of the target orbits. This domain is not useful from the view point of controlling chaos and will not focused later of this section.

3.2.3 Convergence to coexisting orbits

The general feature described above confirmed that robustness of the stabilization to the onset timing, or initial conditions, as was suggested by many experimental results. There is, however, an important feature that has not been discussed in detail previously. One can see convergence to other periodic orbits, not the target orbits, often occurs in specific ranges of feedback gain. For example, one clearly recognizes the convergence to period-$3T$ orbits at $K = 0.935$, period-$6T$ orbits within the interval $0.9 \lesssim K \lesssim 0.93$, period-$5T$ orbits at $K = 0.675$ and so on. The orbits with longer periods, or possessing subharmonic frequency components, coexist with the target orbits in the controlled system. Figure. 3.7 displays various coexisting orbits observed in the steady state of the TV1 case.

The same situation arises also in the TV2 case: the two-well Duffing system with velocity feedback control at $(\delta, A) = (0.16, 0.27)$. The convergence to period-$6T$ orbits is observed for $1.015 \lesssim K \lesssim 1.035$, period-$12T$ orbits at $K = 1.01$ and so on, as shown in Fig. 3.8 and Fig. 3.9. These coexisting orbits become stable within ranges of feedback gain inherent to each orbit. Once a controlled system converges to a stable coexisting orbit, an additional external force

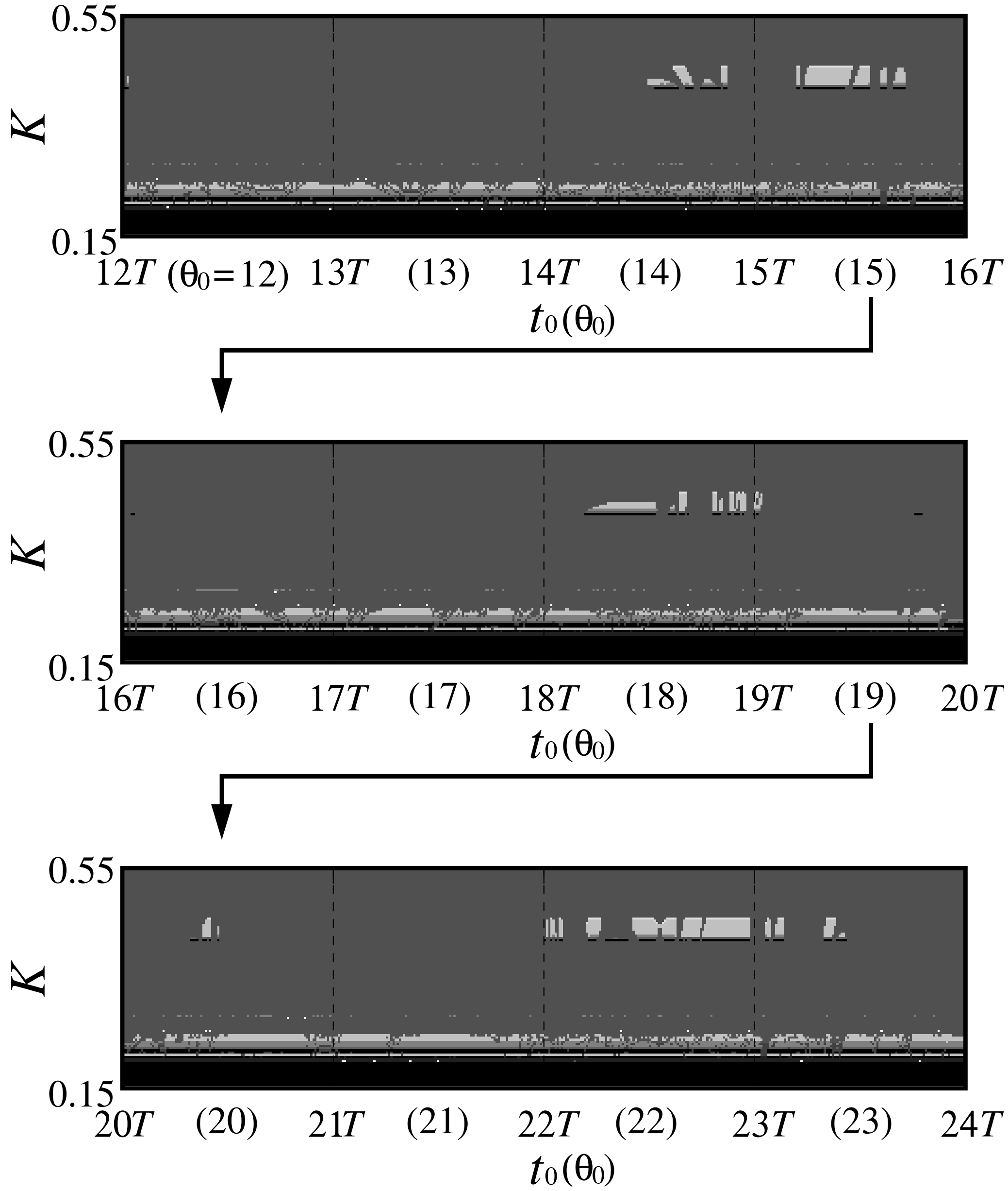

Figure 3.5: Classification of steady states in onset time and feedback gain parameter plane, obtained for the TV1 case from $\theta_0 = 12$ to $\theta_0 = 23$. The classification of tones is shown in Fig. 3.4. The same classification of tones is used from Fig. 3.8 to Fig. 3.11 again.

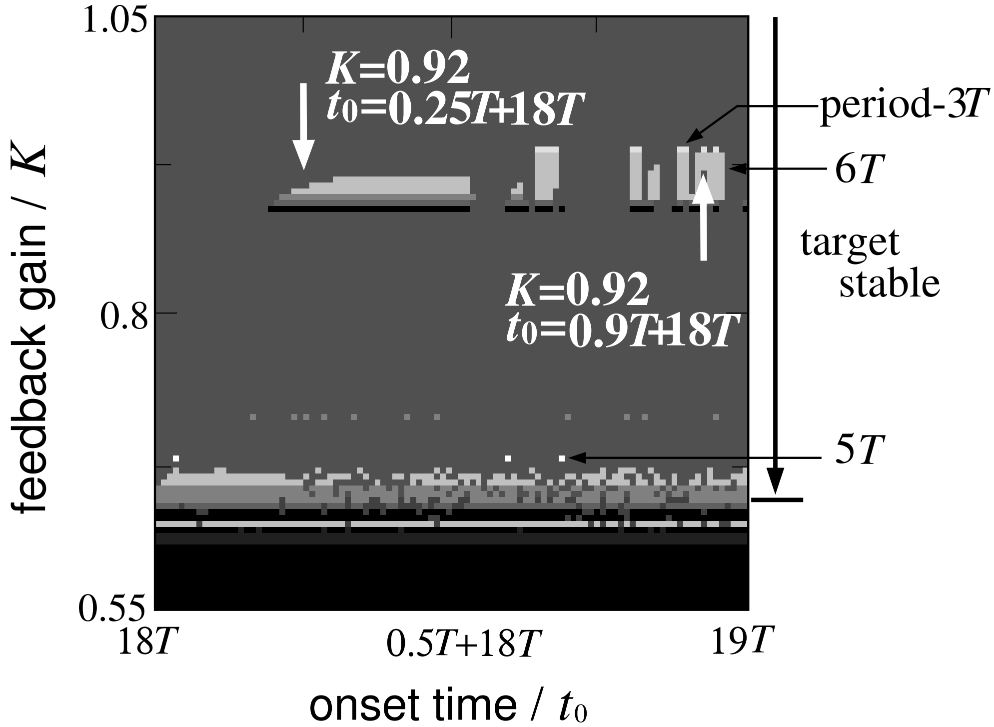

Figure 3.6: Classification of steady states for θ_0 = 18 extracted from Fig. 3.5.

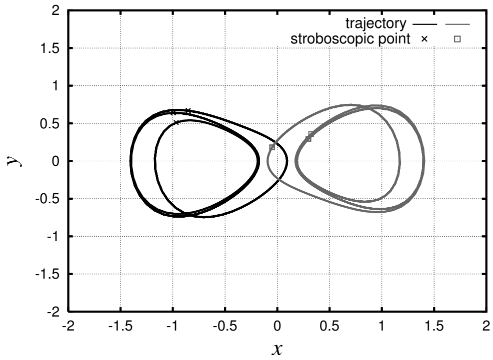

(a) period-3T at $K = 0.935$

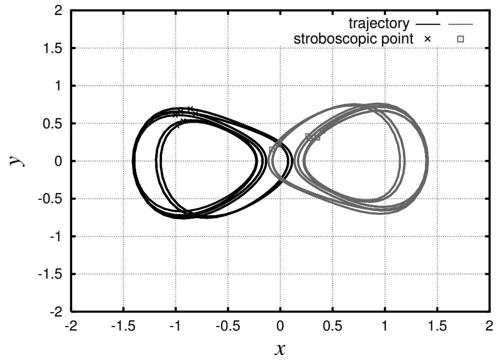

(b) period-6T at $K = 0.92$

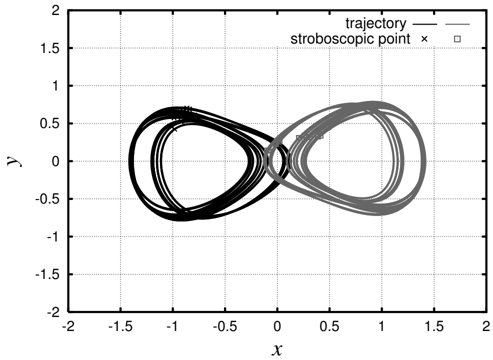

(c) period-12T at $K = 0.892$

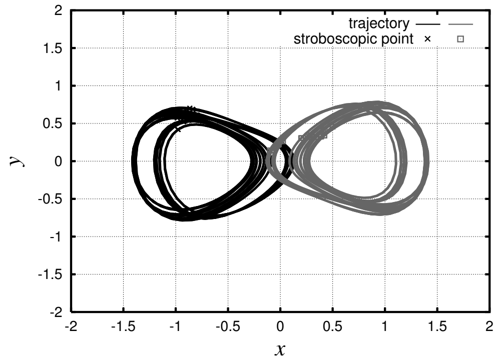

(d) period-24T at $K = 0.89$

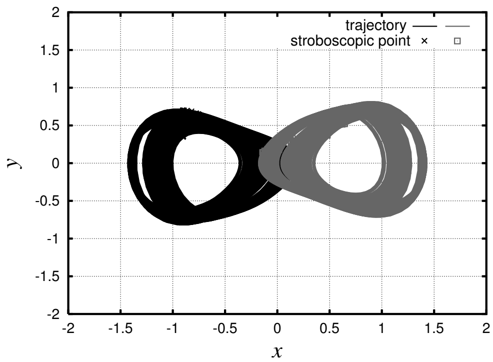

(e) chaos at $K = 0.885$

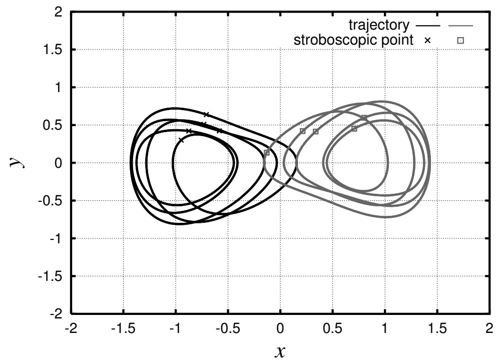

(f) period-5T at $K = 0.675$

Figure 3.7: Coexisting orbits obtained in the TV1 case.

or re-activation of control are requested to make the controlled system go toward a target state. Convergence to coexisting orbits, therefore, implies the failure of control from the viewpoint of controlling chaos.

Convergence to coexisting orbits is also recognized, even when the control method is implemented in another way. Figure 3.10 shows (σ_0, K)-planes in the TD1 case i.e. the two-well Duffing system with displacement feedback control at (δ, A) = (0.46, 0.4). Figure 3.11 is a part of the parameter plane extracted from Fig. 3.10. There are many initial conditions toward coexisting period-$6T$ orbits at $K = 0.28$. The convergence to coexisting period-$4T$, $8T$, and $16T$ orbits is observed at $K = 0.335$, 0.32, and 0.315, respectively. Since both the velocity feedback control and displacement one are implemented without any dependence on the specific information of the two-well Duffing system, one can at least conjecture that convergence to coexisting orbits is not limited phenomena to a particular implementation of the control method.

In this section, convergence to coexisting orbits has been investigated for the controlled two-well Duffing systems. The multiple steady states emerge within certain ranges of feedback gain due to the presence of stable coexisting orbits in the controlled systems. In such ranges, control may fail, because the controlled trajectories converge to coexisting orbits. The convergence to coexisting orbits is commonly observed in the three different cases. This implies that the application of control substantially effects the stability of the coexisting orbits.

3.3 Bifurcation analysis of coexisting orbits

As observed in the Section 3.2, each coexisting orbit seems to have its own stability range for feedback gain. One thing that should be phenomenologically noticed is that a coexisting orbit suddenly disappears at the upper limit of the range and then no multiple steady state presents in the controlled systems. Another is that, at the lower limit, a coexisting orbit loses stability and then another coexisting orbit newly appears. Bifurcation theory is employed to clarify mechanisms for the sud-

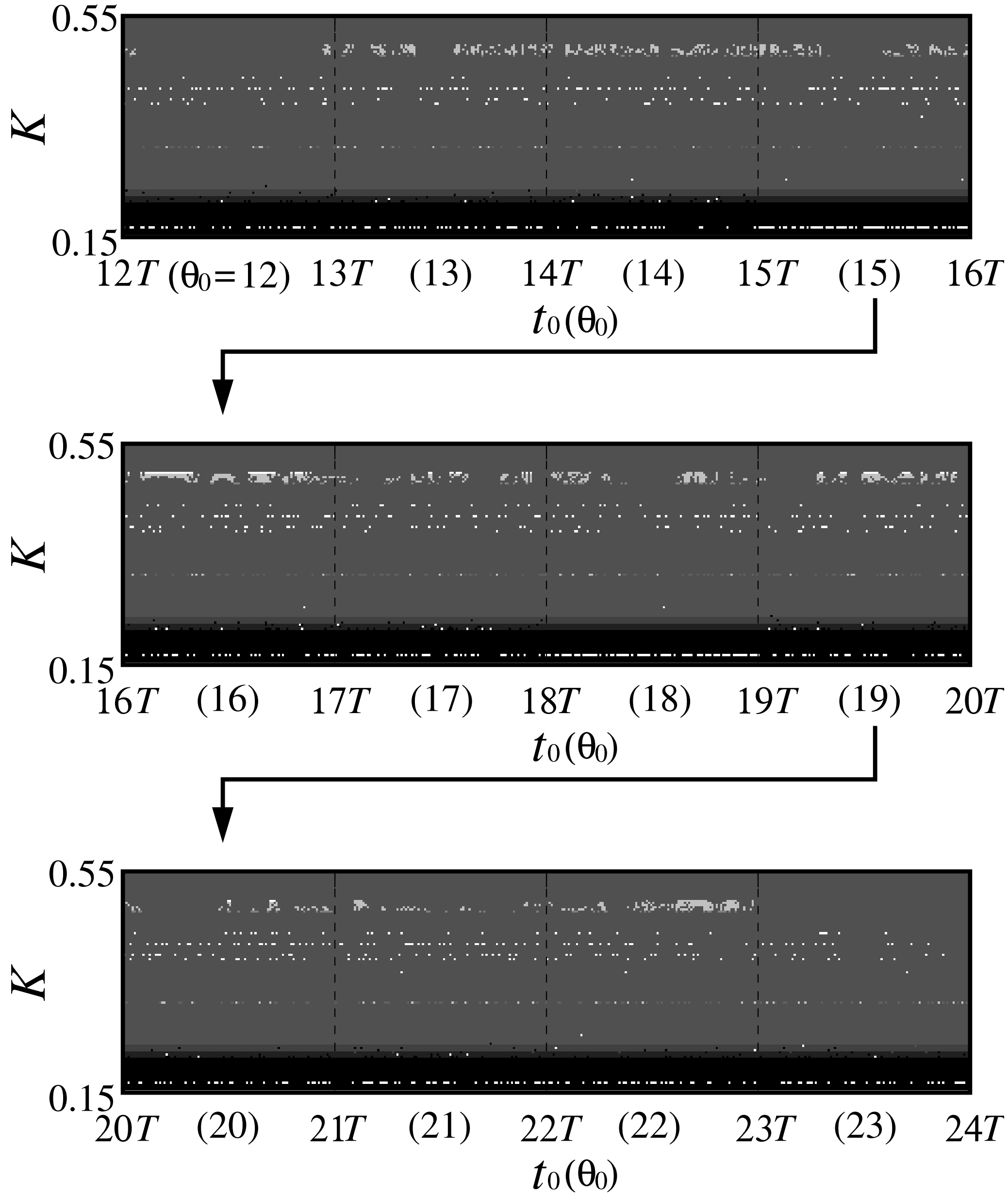

Figure 3.8: Classification of steady states in onset time and feedback gain parameter plane, obtained for the TV2 case from $\theta_0 = 12$ to $\theta_0 = 23$. The classification of tones is shown in Fig. 3.4.

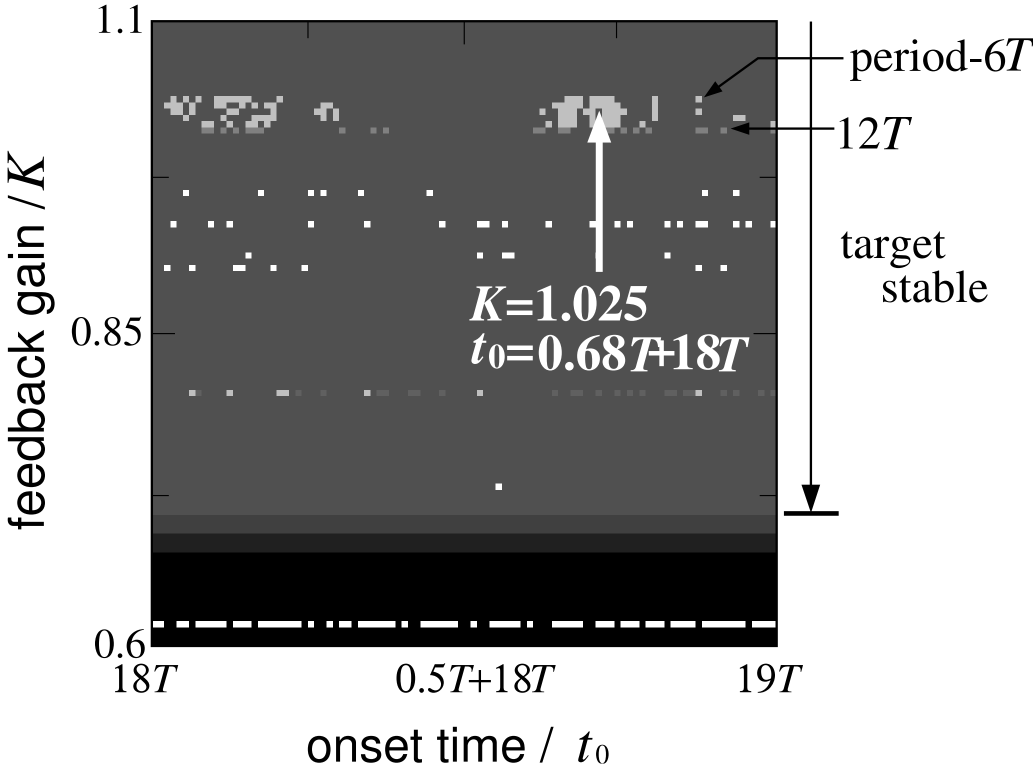

Figure 3.9: Classification of steady states for θ_0 = 18 extracted from Fig. 3.8.

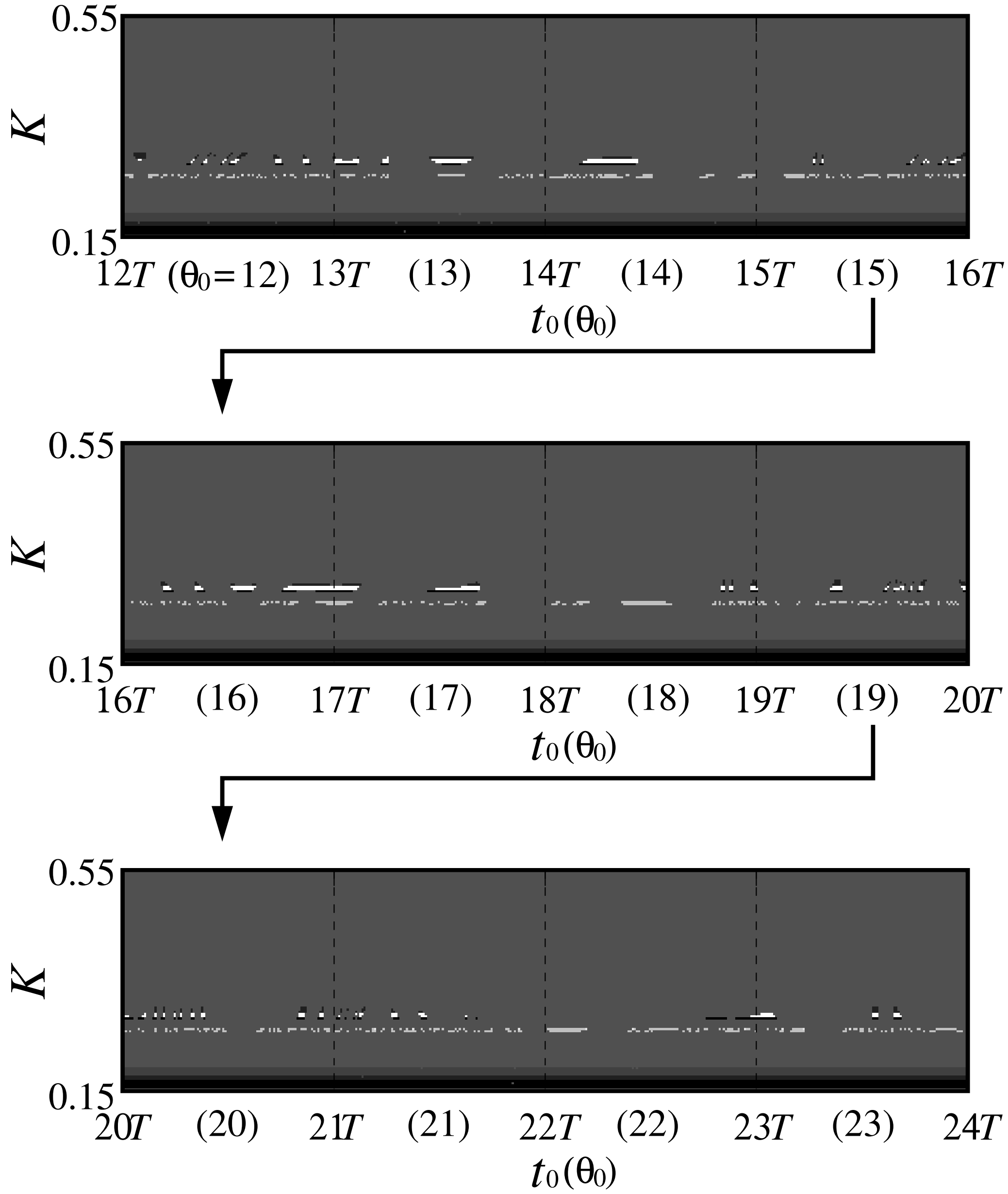

Figure 3.10: Classification of steady states in onset time and feedback gain parameter plane, obtained for TD1 ; two-well Duffing system with displacement feedback control at (δ, A) = (0.46, 0.4) from θ_0 = 12 to θ_0 = 23.

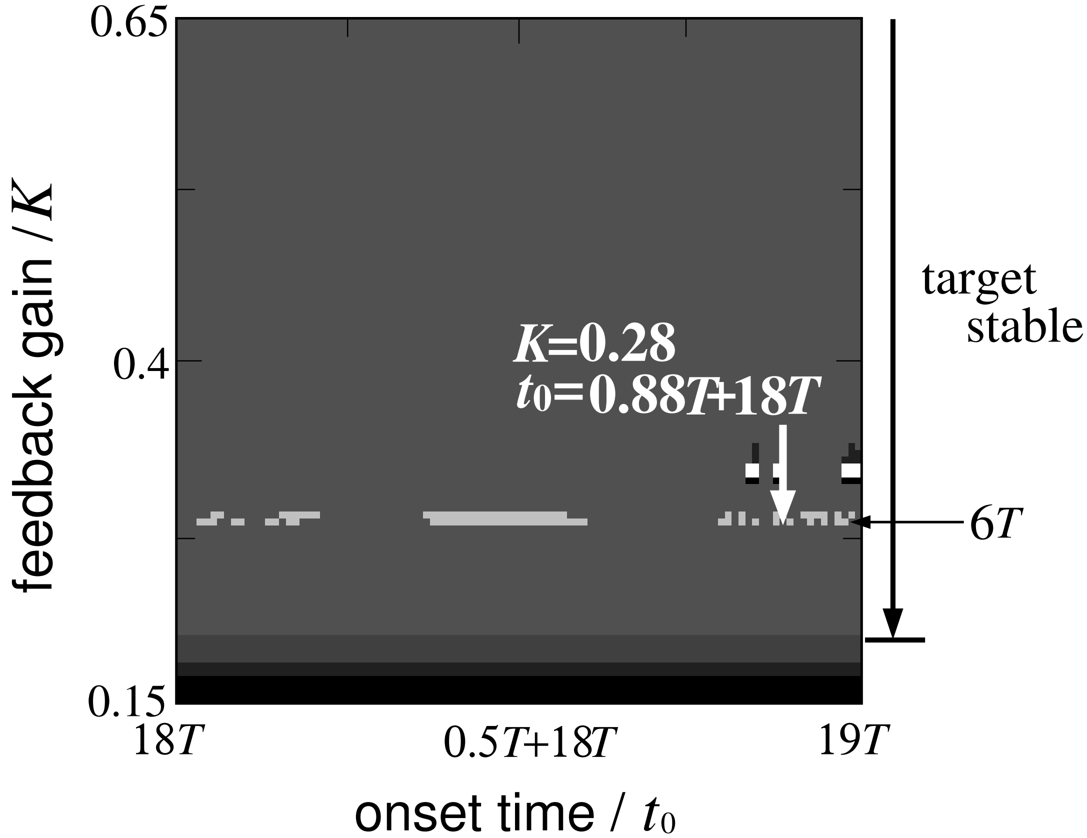

Figure 3.11: Classification of steady states for θ_0 = 18 extracted from Fig. 3.10.

den disappearance and stability loss. The same bifurcation scenario is observed in the different coexisting orbits mentioned in the previous section. The bifurcation of the coexisting period-$3T$ orbits in the TV1 case is therefore overviewed as a typical case in this section.

3.3.1 Generation and annihilation by saddle-node bifurcation

Figure 3.12(a) shows a one parameter bifurcation diagram and related branches of the coexisting period-$3T$ solution in the TV1 case. The bifurcation diagram is shown by light gray points, which are stroboscopic plots of displacement x by the fundamental or excitation period-T. The diagram is obtained by monotonous increase and decrease of feedback gain swept from $K = 0.935$, at which the coexisting orbit was obtained as a steady state from a particular onset time of control. A geometry of the coexisting orbit at $K = 0.935$ is found as the orbit in the right side of Fig. 3.7(a). The black and gray curves denote solution curves of the coexisting *node* and *saddle* later described.

When the feedback gain is increased monotonously from $K = 0.935$, the location (and also the geometry) of the coexisting orbit is gradually changed and its stability is maintained. The coexisting orbit, however, suddenly disappears, when the feedback gain reaches the upper limit of its stability range. This is caused by the saddle-node bifurcation. The bifurcation point is numerically estimated as $K = 0.9382$ and denoted by SN in Fig. 3.12(a). The coexisting orbit loses its stability at the bifurcation point and simultaneously coalesces with another periodic orbit, which has the same period, but is unstable. The stable coexisting orbit and related unstable one is called *node* and *saddle*, respectively, according to the standard notation. As shown in Fig. 3.12(b), a pair of characteristic multipliers of these two orbits visit to unity along the real axis, before their annihilation at the bifurcation point. One of the two for the saddle approaches the unity from the outside of the unit circle and the other for the node from the inside. The coexisting node and saddle are, of course, generated at the same point if the feedback gain is decreased from larger feedback gain. The coexisting node and saddle then no

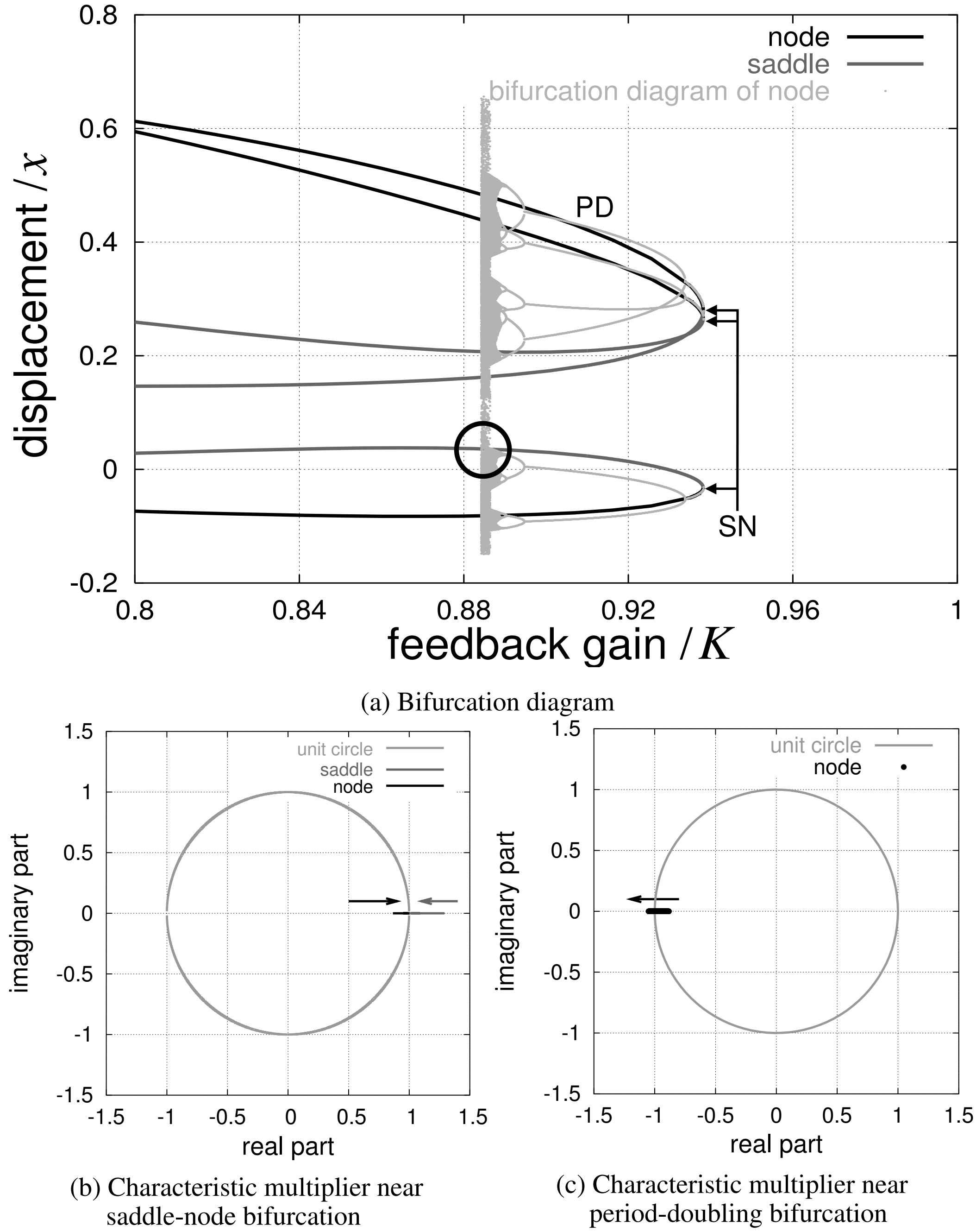

(a) Bifurcation diagram

(b) Characteristic multiplier near saddle-node bifurcation

(c) Characteristic multiplier near period-doubling bifurcation

Figure 3.12: Bifurcation diagram for period-3T coexisting orbits in the TV1 case.

longer exist in the controlled system and therefore only the target orbits remain possible steady states after the bifurcation occurs. The saddle cannot emerge as a steady state. The node is the stable coexisting orbit which has been seen as a steady state previously.

3.3.2 Stability loss by period-doubling bifurcation

The second thing to do is to decrease the feedback gain from $K = 0.935$. One can then see that the coexisting node lose its stability and bifurcate to period-$6T$ orbit in Fig. 3.12(a). Each of the three solution curves emanating from the saddle-node bifurcation point newly generates a pair of branches at $K = 0.9339$. A geometry of the generated period-$6T$ orbit at $K = 0.92$ is shown by curves in the right side of Fig. 3.7(b). The stability loss is caused by the period-doubling bifurcation. One of the characteristic multipliers passes through -1 on the unit circle from inside to outside in this process, as shown in Fig. 3.12(c). The period-doubling bifurcation then successively occurs, as feedback gain continues to decrease. A period-$12T$ coexisting orbit and period-$24T$ one are yielded, as shown in Figs. 3.7(c) and 3.7(d).

3.3.3 Period-doubling route to chaos and its sudden destruction

The coexisting chaotic attractor follows after accumulation of the period-doubling. Once the coexisting chaotic attractor is generated, the chaotic attractor is kept if the feedback gain is slightly decreased. The chaotic attractor is, however, suddenly destroyed as feedback gain continues to decrease. The multiple steady states then no longer present in the controlled system unless other coexisting orbits appear again. Although the mechanism of the destruction cannot be clarified in this dissertation, one suggestive observation is that the chaotic attractor is destroyed when the bifurcation diagram collides with one of the branches of the saddle inside black circle in Fig. 3.12(a). The situation is consistent to a typical scenario observed that in low dimensional systems firstly illustrated by Ott, Grebogi and Yorke [127, 128]. According to their paper, a chaotic attractor and its domain of attraction is suddenly destroyed with *boundary crisis*; a chaotic attractor collides with an unstable orbit which is on the boundary of the domain of attraction of the chaotic attractor. The possibility of boundary crisis in function space is thereby not excluded, but it is difficult to confirm the collision of the chaotic attractor having finite volume in the infinite dimensional phase space.

3.4 Origin of coexisting orbits

A remaining question on the coexisting orbits is where the nodes and saddles come from. The answer is that they originate from unstable periodic orbits embedded in the original chaotic attractor.

This is concluded by Fig. 3.13(a), which traces the unstable coexisting period-$3T$ nodes and saddles analyzed so far. The solution curves are obtained by numerically identifying the unstable periodic orbits with decreasing the feedback gain from the saddle-node bifurcation point to zero. Black and gray curves denote solution curves of the node and saddle, respectively. The solution curves of the saddle collide with those of the node because of the saddle-node bifurcation at the upper limit of stability range, as mentioned before. In the opposite side, all the curves extend to $K = 0$ without vanishing from the phase space. Although the extending curves can correspond to the orbit located outside the original chaotic attractor, Figures 3.15 and 3.14 clearly prove the orbits of the traced nodes and saddles are truly included in the original chaotic attractor. One can simultaneously check that the characteristic multipliers converge to zero except the two multipliers, as the feedback gain is decreased. Since the controlled system becomes two dimensional, only the two multipliers are kept substantial and remaining ones degenerate to redundant ones. The two multipliers of the node converge to $-84.16 + i0$ and $-0.000095 + i0$. The nodes therefore coincide with inversely unstable period-$3T$ orbits embedded in the chaotic attractor. As for the saddles,

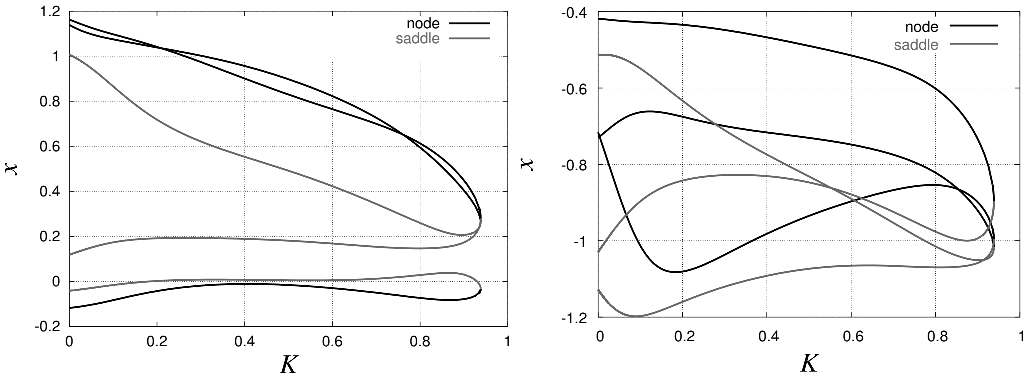

(a) (b)

Figure 3.13: Results for numerical trace of coexisting period-3T orbits in the TV1 case.

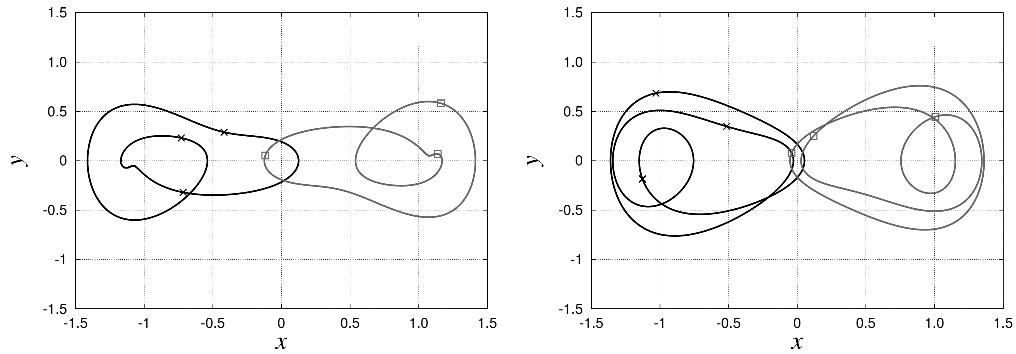

(a) node (b) saddle

Figure 3.14: Coexisting period-3T orbits embedded in the original chaotic attractor generated in the TV1 case.

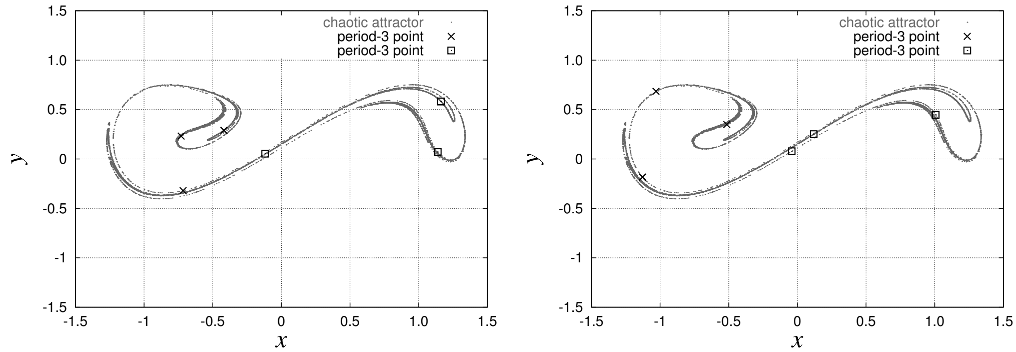

(a) node (b) saddle

Figure 3.15: Coexisting period-3T orbits embedded in the original chaotic attractor on stroboscopic map.

the multipliers become $247.7 + i0$ and $-0.000007 + i0$, showing that they arise from directly unstable period-$3T$ orbits.

3.5 Concluding remarks

In this chapter, we have discussed the multiple steady states arising in the controlled two-well Duffing systems. The three different controlled systems were examined and they are different in system parameters and implementation of the control method. The possibility of multiple steady states is important in practice, because controlling chaos may fail due to the presence of stable coexisting orbits. Stabilization of the target orbits is, in fact, not robust to initial conditions in many ranges of feedback gain. Onset timing determining initial conditions therefore plays a governing role to make the control succeeded. Bifurcation analysis of the coexisting orbits revealed a typical scenario of annihilation by the saddle-node bifurcation and period-doubling route to chaos. Numerically confirmed their persistence for feedback gain clarified the multiple steady states are caused by the stabilization of non-target unstable periodic orbits embedded in the original chaotic attractor. The non-target orbits persist against increasing control input by changing their geometries and stability, but are finally annihilated by saddle-node bifurcation under large feedback gain. Among the non-target orbits, only the inversely unstable periodic orbits can be stabilized under particular range of feedback gain. It should be emphasized that the multiple steady states arising here are caused by control input. Although the multiple steady states are often observed in the uncontrolled two-well Duffing system [113], the applied control input was not too large to drive out the controlled trajectories to outer regions. It is also noted that the bifurcation of the target orbits was not discussed in this chapter. This topic is, however, important for understanding the global dynamics of the controlled system. The appendix below is thus devoted to summarizing the bifurcation of the target orbits in the controlled two-well Duffing system.

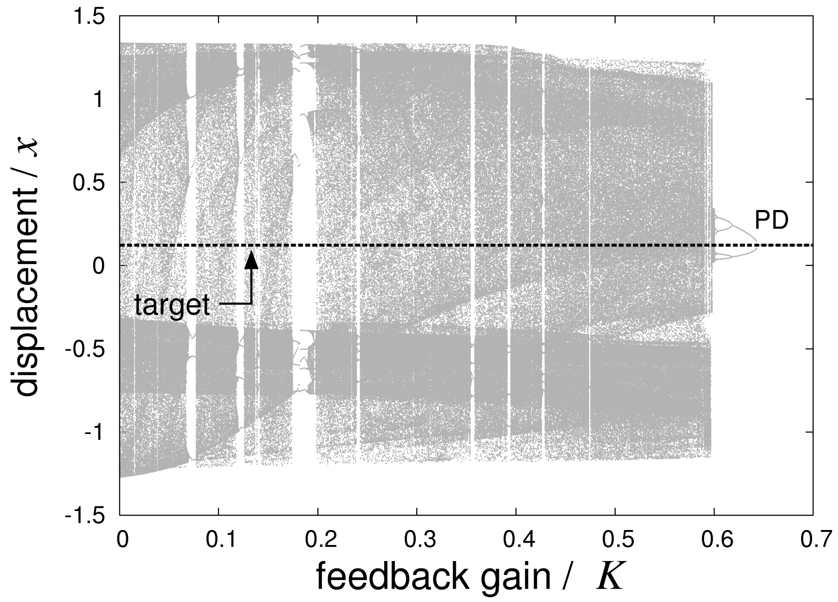

Figure 3.16: Bifurcation diagram of target orbit ^{1}I in the TV1 case.

Appendix to bifurcation of target orbits

As an example, a one-parameter bifurcation diagram of the target orbit ^{1}I is shown by gray points in Fig. 3.16 for the TV1 case. Stability of the target orbit is lost by the period-doubling bifurcation at $K = 0.6448$ and then a period-doubling sequence to chaos occurs, as feedback gain is decreased monotonously. Hikihara *et al.* experimentally found the same fact in the controlled magnetoelastic beam system [124]. As feedback gain is further reduced, the global phase structure in function space seems to be changed and finally the original chaotic attractor is recovered at $K = 0$. The detail of this topic is discussed in Chapter 5. A black dotted line denotes the target orbit in Fig. 3.16. In contrast to the coexisting orbits, the existence, location, and geometry of the target orbits are maintained for any feedback gain. Only the stability is changed due to the control input. It is noted that the target orbits can be made unstable by too large feedback gain. In the TD1 case, stable quasi-periodic orbits are generated by the Neimark-Sacker bifurcation of the target orbits (See, Fig. 6.2 in Chapter 6).

Chapter 4

Domain of attraction for target orbits and its boundary structures

The multiple steady states encountered in Chapter 3 limit the size of domain of attraction for target orbits, which is characterized by the structures of the infinite dimensional phase space. In this chapter, we discuss the domain of attraction for target orbits especially focusing on its boundary structures in function space. Sensitive dependence of steady states on onset timing motivates us to examine features of the boundary structures. A series of external disturbances are given to initial conditions near the boundaries. The perturbation to initial conditions reveals that the domain of attraction possibly has self-similar structures in its boundaries.

4.1 Sensitive dependence on initial conditions

The starting point of this chapter is placed at a more careful observation of the parameter planes already defined and discussed in Chapter 3. The existence of coexisting orbits was shown in the different controlled two-well Duffing systems. One thing worth discussing here is a difference in the distribution of the points which denote convergence to coexisting orbits. Since the parameter planes were defined with respect to onset time, the distribution gives a clue to dependence on initial conditions in function space. An initial condition is slightly modified for each small shift in the direction of t_0-axis of the parameter plane.

The first example is found in the TV1 case, where one can see the points to the coexisting orbits clustered within the interval of feedback gain $0.9 \lesssim K \lesssim 0.935$ of Fig. 3.6. The same kind of distribution is also observed in Fig. 3.5 for $\theta_0 =$ 14, 15, 18, 19, 20, 22 and 23. The clustered distribution suggests that the controlled system has robustness to initial conditions in the sense that the solutions go to the same coexisting orbit when the onset timing is slightly shifted. In contrast, the points to coexisting orbits are scattered within $1.015 \lesssim K \lesssim 1.035$ as for the TV2 case, as shown in Fig. 3.8 and Fig. 3.9. The steady state obtained by control alternates between the target orbits and coexisting ones, sensitively depending on small modification of initial conditions.

The observation above implies a difference in the robustness, or sensitivity, of the dependence on initial conditions. The scattered distribution, in particular, seems to reflect sensitive dependence on initial conditions, which often suggests the existence of chaotic dynamics in a dynamical system. The result of control is then unpredictable against the purpose of the controlling chaos; however, no discussion has been found so far [63]. The domain of attraction is a quite important characteristic of controlled systems, because its size and structure govern the robustness to noises and external disturbances.

4.2 Boundary structures

4.2.1 Perturbation to initial conditions

Since the dependence on initial conditions must reflect boundary structures of the domain of attraction, it is reasonable to focus on initial conditions near the boundaries. Figure 4.1 illustrates the idea to examine boundary structures near an initial condition in function space. An initial condition near a boundary is selected from a point in a parameter plane calculated in Chapter 3. A perturbation is then given to the selected initial condition to generate many different initial conditions near the boundary. Systematic estimation of the effect of perturbation

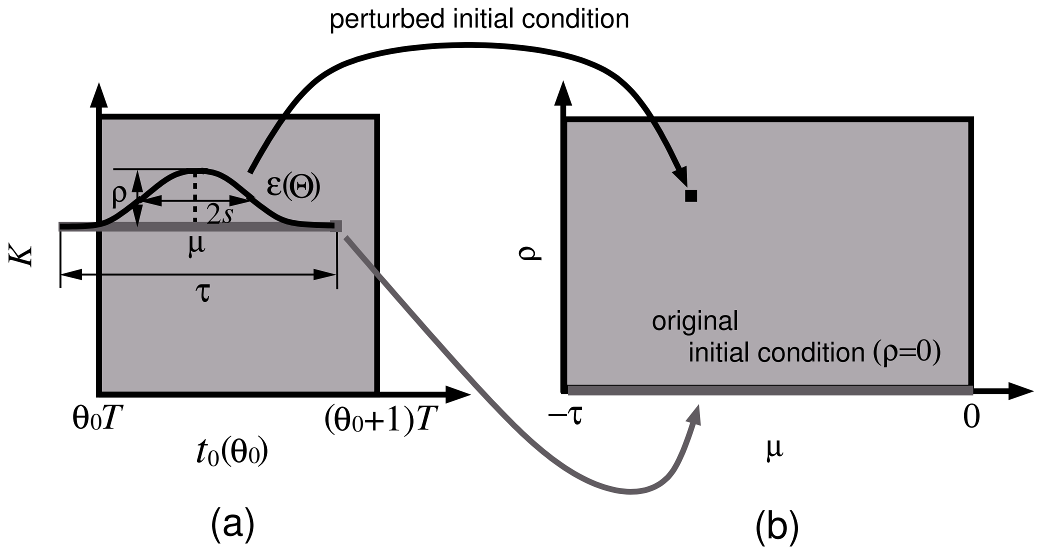

Figure 4.1: A schematic diagram of the method employed to examine boundary structures of domain of attraction. (a) shows a part of the parameter plane defined in Chapter 3. An initial condition is selected from the parameter plane and then perturbed by an external disturbance. A function for the perturbation has Gaussian-like shape in the direction of time and is parameterized by maximum variation of displacement ρ, its center μ, distribution s. Steady states for perturbed initial conditions are classified in a parameter plane with respect to $(\mu,\, \rho)$.

on the convergence provides us substantial information of the domain of attraction in function space.

An external vector disturbance $\boldsymbol{\varepsilon}(\Theta) = \left[\varepsilon(\Theta),\, \dot{\varepsilon}(\Theta)\right]^T$, $-\tau \le \Theta \le 0$ is here considered to perturb a selected initial condition $\boldsymbol{\phi}_{t_0}(\Theta) = \boldsymbol{\phi}(t_0 + \Theta)$, which is a segment of a chaotic trajectory arising just before onset time t_0 and coordinated by $\Theta \in [-\tau,\, 0]$ with reference to the onset time t_0. Each component of the perturbation is defined in the same coordinate as follows:

$$\begin{cases} \varepsilon(\Theta;\, \rho,\, \mu,\, s) = \rho \exp\left[-\left(\dfrac{\Theta-\mu}{s}\right)^2\right], \\ \dfrac{\mathrm{d}\varepsilon(\Theta;\, \rho,\, \mu,\, s)}{\mathrm{d}\Theta} = -\dfrac{2}{s}\left(\dfrac{\Theta-\mu}{s}\right)\varepsilon(\Theta;\, \rho,\, \mu,\, s). \end{cases} \tag{4.1}$$

The displacement component $\varepsilon(\Theta)$ has a Gaussian-like shape in the direction of time axis. The perturbation $\varepsilon(\Theta)$ is physically interpreted as a small force is externally given to the mechanical oscillator in a period just before onset of control. ρ is the amplitude of the perturbation and works as a good indicator of the variation from the original initial condition. The time scale of the variation is given by s and s is fixed at $\tau/2 = T/2$ in the present paper to suppress too fast velocity variation. The perturbation is evaluated at every center of displacement variation μ with introduction of the (μ, ρ)-space. Each point in the (μ, ρ)-space corresponds to an initial condition perturbed by different amplitude and center. Classification of points in the (μ, ε)-space with resulting steady states allows us to discuss the structures of domain of attraction around the selected initial condition. It is noted that the perturbed initial conditions $\phi_{t_0}+\varepsilon$ cannot be generated by the uncontrolled system without external disturbance. This is because ε does not have a uniform approximation by the linear combination of exponential solutions in general. One cannot expect that ε satisfies the variational equation of the original systems.

4.2.2 Structures far from boundary

There should be no perturbation to change a steady state if a selected initial condition is located away from the boundaries of the domain of attraction. This seems to be trivial but has to be checked to validate the proposed method before proceeding to examine boundary structures. We here choose an initial condition pointed by an arrow in the left side of the Fig. 3.6. The pointed initial condition is obtained when control is activated at $t_0 = 0.8T + 18T$. The feedback gain is here adjusted at $K = 0.92$, at which the coexisting period-6T orbits exist as mentioned in Section 3.2.3. The initial condition seems to lie apart from the boundaries of the domain of attraction, because no point to coexisting period-6T orbits is present near the selected initial condition. The steady state corresponding to the selected initial condition is therefore expected to have robustness to external disturbance to the controlled system. Figure 4.2(a) shows the domain of attraction around this initial condition in the (μ, ρ)-space. One can see that no boundary appears and

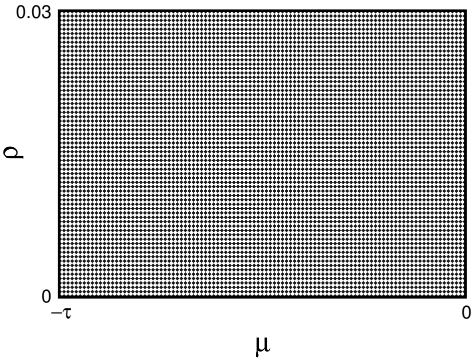

(a) Domain of attraction for
$(t_0, K) = (0.25T + 18T, 0.92)$

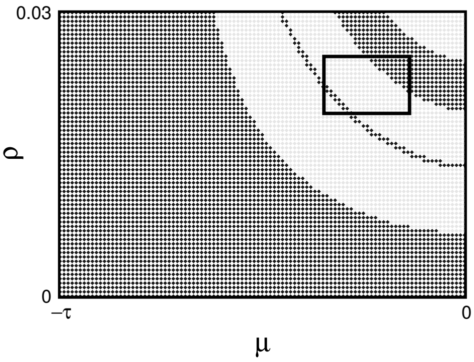

(b)Domain of attraction for
$(t_0, K) = (0.9T + 18T, 0.92)$

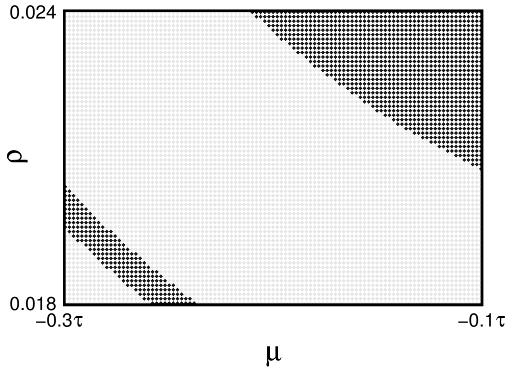

(c) Enlargement of (b)

Figure 4.2: Domain of attraction on (μ, ρ)-space in the TV1 case. Dark and light gray points denote convergence to target period-T orbits and coexisting period-$3T$ ones, respectively. (a) and (b) are obtained around initial conditions pointed by arrow in the left side and the right side in Fig. 3.6, respectively. (c) displays enlargement of boundaries within a rectangular area in (b).

the domain is completely governed by convergence to a target orbit, as shown by black points. The external disturbance has no influence on results of control.

4.2.3 Smooth boundary structures

The next initial condition to be perturbed is pointed by an arrow in the right side of Fig. 3.6. The point lies close to the one to a coexisting period-$6T$ orbit in contrast to the previous selection. The pointed initial condition is therefore expected to be near the boundaries between the domain of attraction for the target orbit and for the coexisting one. One can, in fact, confirm that the domain of attraction around this initial condition is found to have clear boundaries as shown in Fig. 4.2(b). The boundaries smoothly curve from right side to top. An important feature is that a part of the boundaries is clearly enlarged as shown in Fig. 4.2(c). No additional boundaries appear in the enlarged region. It is obvious that this simple structure cannot yield the sensitive dependence on initial conditions opposite to the next case.

One additional thing is that the observed boundaries are concentrated around $\mu = 0$ and no one is found around $\mu = -\tau$. The boundaries smoothly curving from right side to top right suggests that the steady state is governed by the state of the system at onset time. The past state is not dominant factor to determine the steady state in the present setup, since the perturbation with μ near zero has little effects on $\phi_{t_0}(0)$ i.e. the current state.

4.2.4 Self-similar boundary structures

The boundaries in Fig. 4.3 have a self-similar structure quite contrast to the previous smooth boundaries. An initial condition is selected from Fig. 3.9. The selected initial condition is indicated by an arrow in Fig. 3.9. Around the arrow, the point to coexisting period-$6T$ orbits are scattered. The boundaries exhibit rough curves in distinction to the previous smooth case in Fig. 4.2(b) and Fig. 4.2(c). More precisely, many fine striped structures run along each of the boundaries.

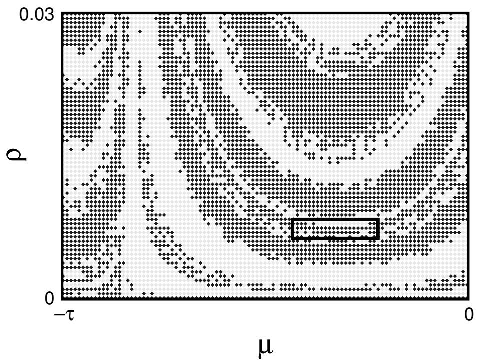

(a) Domain of attraction for
$(t_0,\ K) = (0.68T + 18T,\ 1.025)$

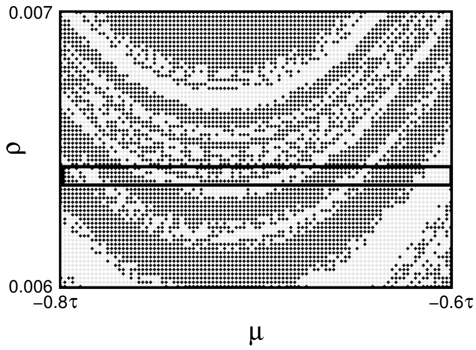

(b) Enlargement of (a)

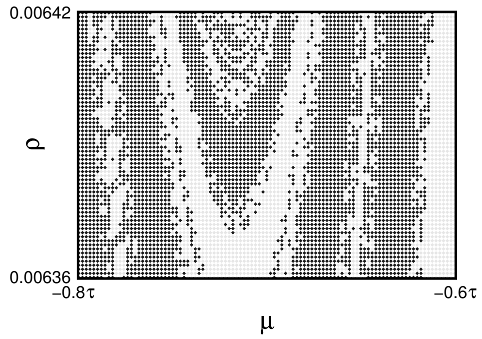

(c) Enlargement of (b)

Figure 4.3: Domain of attraction on $(\mu,\ \rho)$-space in the TV2 case. Dark and light gray points represent convergence to target period-T orbits and coexisting period-$6T$ ones, respectively. (b) and (c) are enlargement of rectangular areas in (a) and (b), respectively. They show self-similar structures around initial condition pointed by an arrow in Fig. 3.6(b).

The self-similarity of the boundaries is confirmed by enlarging the fine stripes. When one enlarges a part of the stripes, the same fine stripes appear again, as shown in Fig. 4.3(b). A part of this enlarged domain also have the same structure, which is found by enlarging again, as displayed in Fig. 4.3(c). Self-similar structures are yielded in the phase space of chaotic dynamical systems in general. The difference is that the domain of attraction is here defined in function space apart from the target orbits. More precisely, the (μ, ρ)-spaces represent the domain of attraction around the selected initial condition along the temporal axis. The self-similarity in the (μ, ρ)-spaces implies the sensitive dependence of steady states on amplitude and timing of small external disturbance to the selected initial condition. The controlled system therefore loses the robustness for the initial condition. The global structure governing the system cannot be simple in function space.

Figure 4.4 shows a self-similar structure in the TD1 case. We examine the domain of attraction near the initial condition pointed by an arrow in Fig. 3.11. Many fine stripes are found along the boundaries from lower left to right side in Fig. 4.4(a). The enlargement of a part of the stripes displays fine striped structures again, as shown in Fig. 4.4(b). On the other hand, there is a difference from the previous case that smooth boundaries are partly observed in the upper left of Fig. 4.4(a). The enlargement also shows smooth boundaries as compared with the previous rough case of Fig. 4.3. It seems that the self-similarity is truncated or localized in function space.

The above self-similar structures reveal the convergence to target orbits sensitively depends on initial condition in function space. In other words, successful prediction of controlling chaos is difficult before the control is achieved. It is clearly understood that this unpredictability is a disadvantage for engineering use of the control method, though no detailed discussion for the characteristics has been obtained.

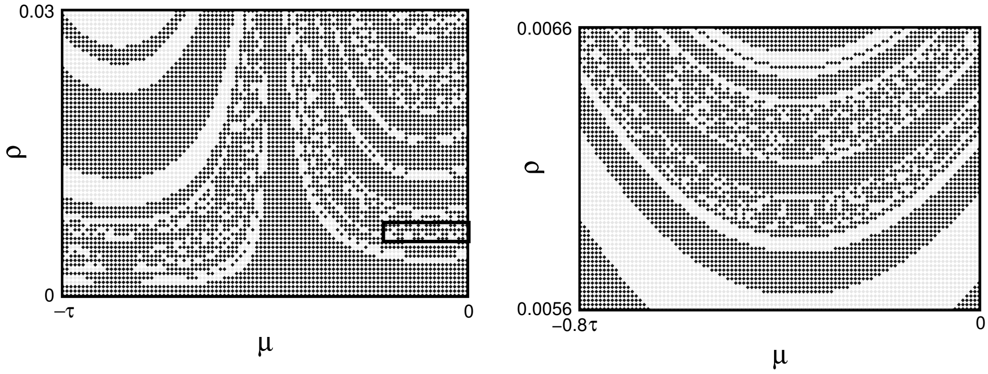

(a) Domain of attraction for
$(t_0, K) = (0.88T + 18T, 0.28)$

(b) Enlargement of (a)

Figure 4.4: Domain of attraction on (μ, ρ)-space in the TD1 case. Dark and light gray represent convergence to target period-T orbits and coexisting period-$6T$ ones, respectively. (b) is enlargement of rectangular area in (a). They displays self-similar structures around the initial condition pointed by an arrow in Fig. 3.11.

4.3 Boundary structures and selective stabilization of two target orbits

The two-well Duffing system has the two target orbits denoted by $^{1}\mathrm{I}$ and $^{1}\mathrm{I}'$ due to its symmetry, and they have not been explicitly distinguished in the foregoing discussion. The domain of attraction for each of the orbits is important, when one has to specify one of the two as a unique target in advance of control. Both $^{1}\mathrm{I}$ and $^{1}\mathrm{I}'$ are stable in the controlled system, since the control method itself has no ability to make one stable and keep the other unstable without any additional strategy. The problem is from where to choose an appropriate initial condition in function space to achieve convergence to the prespecified orbit. The more fundamental is whether such a choice is possible or not. This section seeks a clue to these problems by applying the same approach to the TV1 and TV2 cases.

Figure 4.5(a) shows the classification of stabilized orbits for $\theta_0 = 15$ in the TV1 case. An additional dark tone classifies convergence to $^{1}\mathrm{I}$ (dark gray) and that to $^{1}\mathrm{I}'$ (light gray). One can clearly see a boundary of the two areas. The steady state is dominant by $^{1}\mathrm{I}$ in the left dark gray area. On the other hand, the steady

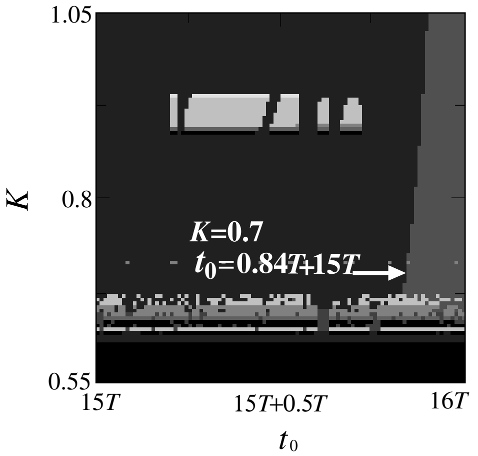

(a) Classification of steady states for $\theta_0 = 15$

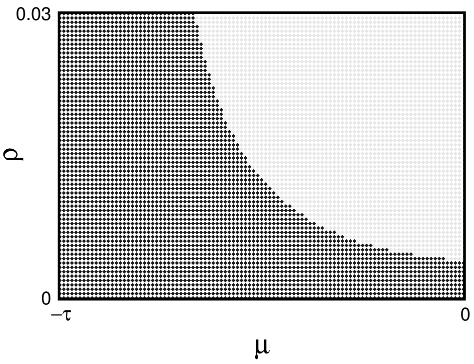

(b) Domain of attraction for $(t_0, K) = (0.84T + 15T, 0.7)$

Figure 4.5: Classification of stabilized orbits ((a)) and domain of attraction ((b)) in the TV1 case. In (a), classification distinguishes two symmetric target orbits with additional dark tone. (b) is obtained around the initial condition pointed by the arrow in (a).

state is changed to ${}^1\mathsf{I}'$ in the right light gray region. The boundary is smooth and no qualitative difference is shown between high and low amplitude of feedback gain. The smoothness reflects the structure of the domain of attraction shown in Fig. 4.5(b). The domain is obtained around the initial condition pointed by an arrow in Fig. 4.5(a). No qualitative difference is shown, corresponding to the (σ_0, K)-plane. The structure in the boundary region keeps its smoothness, as feedback gain is varied.

On the other hand, a completely different situation arises in Fig. 4.6(a) showing the classification for $\theta_0 = 18$ in the TV2 case. The classification in the area of large feedback gain has a smooth boundary between convergence to ${}^1\mathsf{I}'$ and that to ${}^1\mathsf{I}$. The boundary, however, loses its smoothness as the feedback gain is decreased. One can see that the points to ${}^1\mathsf{I}'$ and ${}^1\mathsf{I}$ are finely mixed in the low area. The situation is made more clear in the domain of attraction on the (σ, μ) space. Figure 4.6(b) shows a smooth boundary of the domain near the initial condition selected at $(t_0, K) = (0.94T + 18T, 1.1)$. No complicated structure is observed

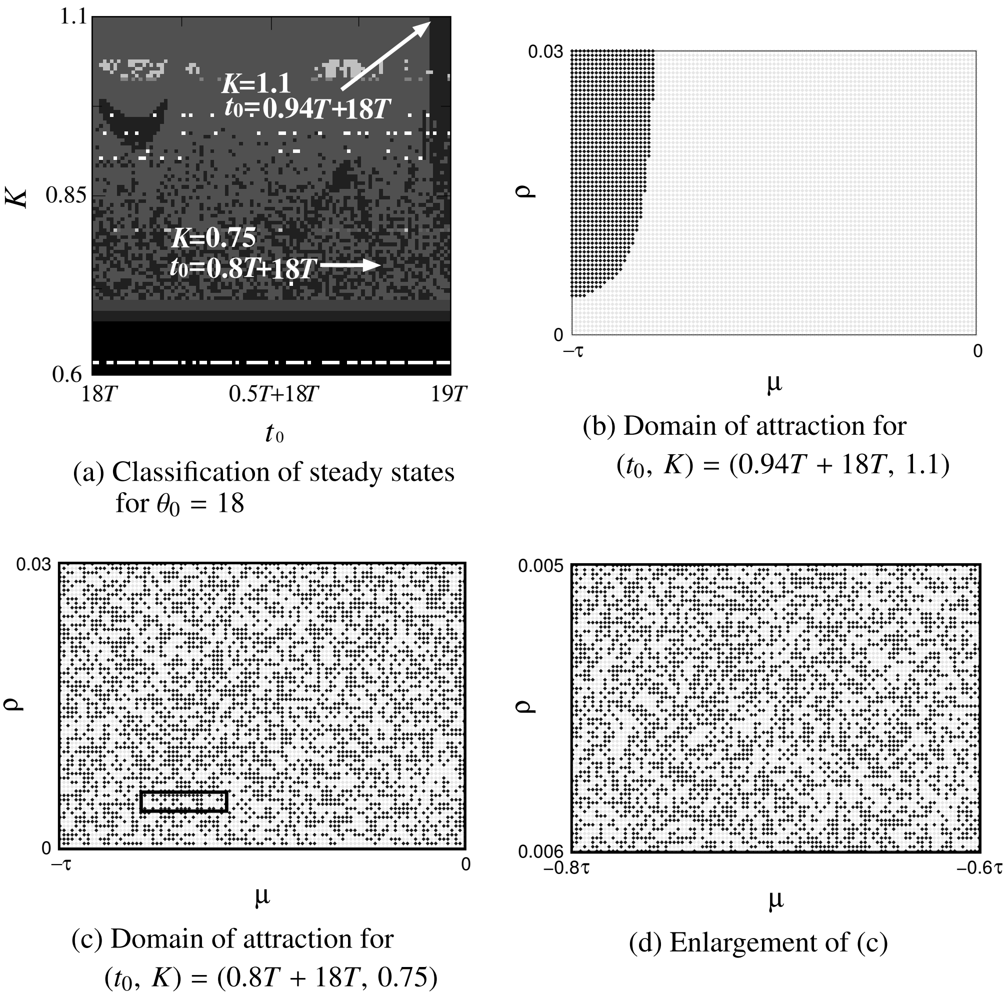

(a) Classification of steady states for $\theta_0 = 18$

(b) Domain of attraction for $(t_0, K) = (0.94T + 18T, 1.1)$

(c) Domain of attraction for $(t_0, K) = (0.8T + 18T, 0.75)$

(d) Enlargement of (c)

Figure 4.6: Classification of stabilized orbits ((a)) and domain of attraction ((b), (c), and (d)) in the TV2 case. In (a), classification distinguishes two symmetric target orbits $^1\mathsf{I}$ and $^1\mathsf{I}'$ with additional dark tone. (b) is obtained at $K = 1.1$ around initial condition at $t_0 = 0.94T + 18T$ pointed by an arrow in (a). A boundary is smooth and no additional structure is seen. (c) is domain of attraction for $K = 0.75$ and $t_0 = 0.8T + 18T$. (d) displays enlargement of rectangular area in (c). (c) and (d) show stabilized states almost randomly alternate between $^1\mathsf{I}$ and $^1\mathsf{I}'$ by external disturbance or noise.

in this case. In contrast, Fig. 4.6(c) reveals a completely different structure in the boundary. The points to ${}^1\mathsf{I}'$ and ${}^1\mathsf{I}$ are mixed and the same structure holds even in an enlargement shown in Fig. 4.6(d). This mixed structure is obtained near the particular initial condition corresponding to $(t_0,\ K) = (0.8T+18T,\ 0.75)$ indicated in Fig. 4.6(a); however, one can easily understand that Fig 4.6(a) has the mixed structure covering over the whole onset time of control in the area of low feedback gain. It is therefore inevitable that the steady state of the controlled system almost randomly alternate between ${}^1\mathsf{I}$ and ${}^1\mathsf{I}'$ depending on onset timing of control and influence of external disturbances. This also suggests that the global dynamics in function space is much more complicated than expected in many previous literatures.

In this section, we have discussed the domain of attraction for the target orbits with additional classification of ${}^1\mathsf{I}$ and ${}^1\mathsf{I}'$. The results show the domain of attraction possibly has a very complicated structure causing super high sensitive dependence on initial conditions. It is therefore so difficult to select one of the target orbits as the steady state before starting control.

4.4 Concluding remarks

In this chapter, domain of attraction in function space has been investigated by perturbation to the initial conditions near the boundaries. The numerical results suggested that the existence of chaotic dynamics in function space, going beyond the scope of the conventional approach using linearization techniques. The initial conditions, of course, have infinite degrees of freedom to be changed; nevertheless the Gaussian-like perturbation gave a clue to discuss how the convergence to the target orbits depends on the past state of the system. The domain of attraction in the parameter plane showed that steady states depend on initial conditions in different ways. In particular, the self-similar structures in the boundaries explained the sensitive dependence on initial conditions related to the scattered distribution of points to coexisting orbits. The self-similar structures also imply that convergence to the targets, or success of control, sensitively depends on onset time of control and external disturbance to controlled systems from the practical viewpoint. Another quite complicated structure was clarified in Section 4.3 related to the selective stabilization of the two target orbits. The boundary between the two domains reveals that the targeting scheme based on linearization does not work well. It should be emphasized that one has to take global dynamics of the controlled systems into account. The exact model of a chaotic system is often unknown in practical situation and thereby one possibly activates control apart from the neighborhood of the target orbits. The controlled dynamics is then governed by the global phase structure instead of the stability given to the target orbits. In the next chapter, we continue to investigate the global dynamics of the controlled systems.

Chapter 5

Global structures and related control characteristics

This chapter presents a detailed investigation on the global phase structure of the controlled two-well Duffing system. We discuss a qualitative change of the global phase structure and clarify controllability of the target orbits from the viewpoint of the global dynamics. A global unstable manifold of a periodic orbit focused on throughout this chapter provides a clue to the global phase structure in function space. In particular, we reveal the mechanism behind the difficulty in the selective stabilization of the two target orbits found in Chapter 4. Persistence of the original chaotic dynamics complicates boundary structures of the domain of attraction and transient dynamics. An improved control performance is also discussed based on the global phase structure greatly simplified under large feedback gain.

5.1 Unstable manifold and global dynamics

One can easily imagine that the full nonlinear dynamics in function space is extremely difficult to investigate in general due to its high dimensional nature. Clarification of finite dimensional unstable manifolds and infinite dimensional stable ones are required to achieve the complete description of the global phase structure. One possible way to understanding the controlled dynamics is therefore to

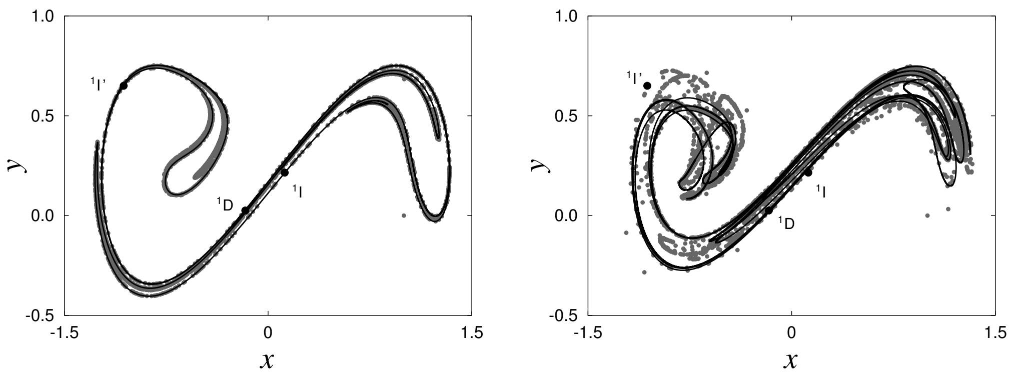

(a) $K = 0.0$ (b) $K = 0.3$

Figure 5.1: Unstable manifold of $^1\mathsf{D}$ (projection on two dimensional stroboscopic plane) in the $\mathsf{TV1}$ case. In (a) and (b), target orbits are unstable and chaotic attractor is generated, as shown by gray stroboscopic points.

concentrate on dynamical structures which play a governing role in the global dynamics in function space. A one-dimensional global unstable manifold is here focused on, because this unstable manifold is expected to provide substantial information on the global phase structure in function space. One should keep in mind that the unstable manifold maintains its existence and dimension even under control input due to the odd number condition. Conventional numerical techniques can apply to calculation of the unstable manifold in function space. The same approach has been used recently in analysis of a laser system modeled by a difference differential equation [129].

The original two-well Duffing system is a good starting point of the investigation, because control input can be treated as a perturbation to the original system. The original dynamics was fully captured numerically and analytically in the previous literatures. The global dynamics of the two-well Duffing system was firstly investigated by Moon and Holmes [14], and subsequently reconfirmed and extended greatly by Ueda *et al.* [113]. A governing role in the global dynamics is played by the directly unstable periodic orbit denoted by $^1\mathsf{D}$ in Fig. 2.3. Since the stable and unstable manifolds of the orbit generate a homoclinic intersection

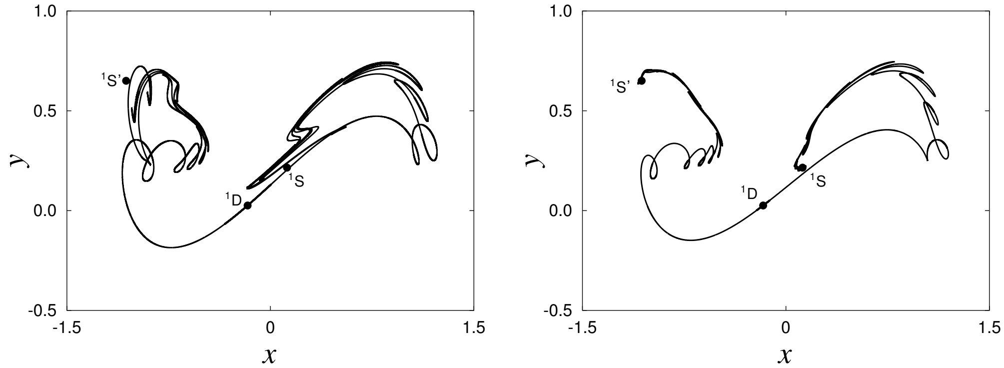

(c) $K = 0.7$ (d) $K = 1.0$

Figure 5.1(Continued): In (c) and (d), targets are stable and stroboscopic points show transient behavior before convergence to a target orbit. Notation of target orbits are changed to $^1\mathsf{S}$ and $^1\mathsf{S}'$ for their stability change. Arrows in (c) and (d) indicate the same stroboscopic point at which the control is activated.

in the cross section induced by stroboscopic mapping with period-T, a chaotic invariant set exists in the original system. The closure of the unstable manifold coincides with the chaotic attractor, in which the target orbits and $^1\mathsf{D}$ are embedded. One can, in fact, check this in Fig 5.1(a), where the unstable manifold and the chaotic attractor are shown in the TV1 case at $K = 0$. The system examined is formally identical to the controlled system at zero feedback gain. One can easily confirm that the closure of the unstable manifold coincides with the chaotic attractor shown by gray stroboscopic points. The chaotic invariant set exists at this stage, since the unstable manifold of $^1\mathsf{D}$ transversely intersects the stable manifold of $^1\mathsf{D}$ [14, 113], as mentioned above. The regions of phase space are stretched and folded along the unstable manifold with its temporal evolution.

Once control is activated under $K > 0$, the original dynamics is perturbed by control input. The dimension of the system is then increased from the original two to infinite due to the presence of delayed input. On the other hand, the global phase structure itself is still governed by the unstable manifold of $^1\mathsf{D}$ because of the odd number condition. The dynamical property of $^1\mathsf{D}$ does not change under control input, that is, $^1\mathsf{D}$ keeps a unique real characteristic multiplier greater than unity without any additional unstable multipliers for $K > 0$. As a result, $^1\mathsf{D}$ keeps the global unstable manifold tangent to the one-dimensional unstable subspace of $^1\mathsf{D}$ under control input. Figure 5.1(b) shows the unstable manifold at $K = 0.3$, where the target orbits are still unstable and then the chaotic attractor is generated under control input. One can clearly see that the unstable manifold inherits the global stretch and fold structure from the original unstable manifold at $K = 0$. The two branches of the unstable manifold initially develop in the opposite direction each other. Both branches are, however, folded and then come close to $^1\mathsf{D}$ again parallel to themselves. The regions of the phase space are stretched around $^1\mathsf{D}$ and folded around the left and right sides in Fig. 5.1(b) with temporal evolution, as was observed in Fig. 5.1(a) at $K = 0$. The difference is that the unstable manifold is here projected from the function space to the original two dimensional stroboscopic plane. This is the reason that the unstable manifold appears to intersect itself.

The two target orbits $^1\mathsf{I}$ and $^1\mathsf{I}'$ are made stable by further increasing feedback gain. The unstable manifold at $K = 0.7$ is shown in Fig. 5.1(c). The stabilized target orbits are here denoted by the $^1\mathsf{S}$ and $^1\mathsf{S}'$, respectively. It seems that the global chaotic dynamics no longer exists in the controlled system, since neither global stretch and fold are observed nor return of the unstable manifold parallel to itself is found. The homoclinic intersection is broken, and stretch and fold are localized near the target orbits. The two branches developing from $^1\mathsf{D}$ stay around the different target orbits under the effects of the localized stretch and fold. The localization implies that the controlled trajectories driven along the unstable manifold has no possibility to approach the target orbit in the opposite side from their initial region.

The global phase structures is finally changed completely from the previous three cases. A clear picture of this situation is exemplified by the unstable manifold at $K = 1.0$ shown in Fig. 5.1(d). A quite simple structure is obtained as compared with structures in Fig. 5.1(a), Fig. 5.1(b), and Fig. 5.1(c). Neither global nor local stretch and fold are observed. The two branches converge to the different target orbits, twisting around them, under no influence of stretch and fold. It is therefore evident that some global bifurcations break up the homoclinic intersection and subsequently destroy the localized stretching and folding structures.

This section has overviewed the qualitative changes of the unstable manifold of $^1\mathsf{D}$. The first clear image was given as to how the control input works on the global phase structure in function space. The original structure causing chaotic dynamics is destroyed and then simplified, as feedback gain is increased. The scenario is here illustrated as a typical one using the $\mathsf{TV1}$ setup with varying the feedback gain. The same scenario is observed in other parameter setups and also in the Duffing system [130]. This suggests the scenario is generalized to a certain class of dynamical systems. The detail of this topic is discussed in Chapter 6.

5.2 Persistence of chaos with stable targets

The previous section has shown that control input changes the global phase structure as well as the stability of the target orbits. It is then expected that a controlled trajectory quickly converges to one of the target orbits, if the feedback gain is sufficiently large to give stability to the targets and also vanish the original chaotic dynamics. One interesting question arising here is that how the controlled system behaves if the target orbits are locally stabilized but the original chaotic dynamics persists against control input. In this section, this question is discussed by applying the same approach to the $\mathsf{TV2}$ case.

Figure 5.2 displays the unstable manifold of $^1\mathsf{D}$. One can easily check the coincidence of the unstable manifold with the original chaotic attractor at $K = 0.0$ in Fig. 5.2(a) and the chaotic attractor is then inherited by the perturbed dynamics at $K = 0.3$ in Fig. 5.2(b). The target orbits are unstable in both cases. As the feedback gain is further increased, the two target orbits become stable. There is, however, a crucial difference from the previous $\mathsf{TV1}$ case in that the unstable manifold still keeps the stretch and fold structure. Figure 5.2(c) shows the unstable manifold for $K = 0.75$ slightly over the threshold value for the stability

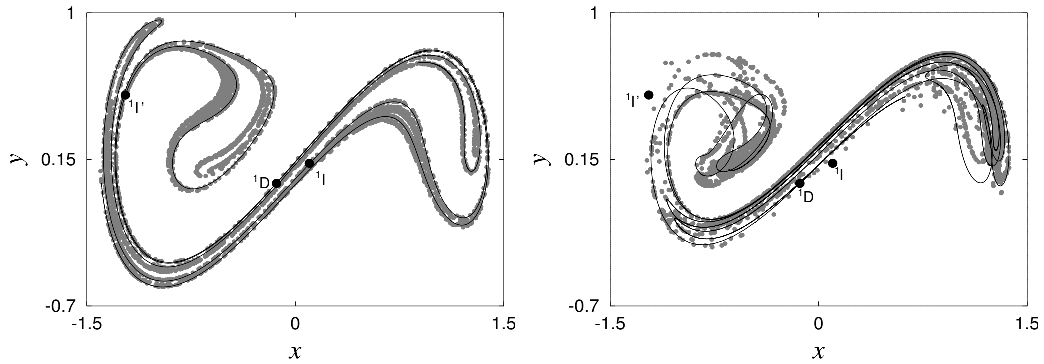

(a) $K = 0.0$ (b) $K = 0.3$

Figure 5.2: Unstable manifold of ^{1}D (projection on two dimensional stroboscopic plane) in the TV2 case. In (a) and (b), target orbits are unstable and chaotic attractor is generated, as shown by gray stroboscopic points. In (c) and (d), targets are stable and stroboscopic points show transient behavior before convergence to a target orbit.

change. The two branches of the unstable manifold start from ^{1}D in the opposite direction from each other. They are, however, folded and then come close to ^{1}D again parallel to the branches themselves. The branches further grow in the opposite direction from each other. The regions of phase space are stretched near ^{1}D and then folded around the left and right hand sides in Fig. 5.2(c) with the temporal evolution. This implies that the phase space inherits the characteristics that produce the chaotic dynamics for $K = 0$ and $K = 0.3$, while the original chaotic attractor is destroyed because of the stability change of the target orbits. By the same approach, we can confirm the same scenario as in the previous section. The homoclinic intersection is destroyed and the completely simplified unstable manifold connects the target orbits and ^{1}D, as shown in Fig. 5.2(d).

This section presented a quite interesting case where the original chaotic dynamics can coexist with target orbits are stable. These results indicate that the controlled dynamics exhibit completely different behavior depending on the global phase structure. In the next section, influences on control performance are discussed.

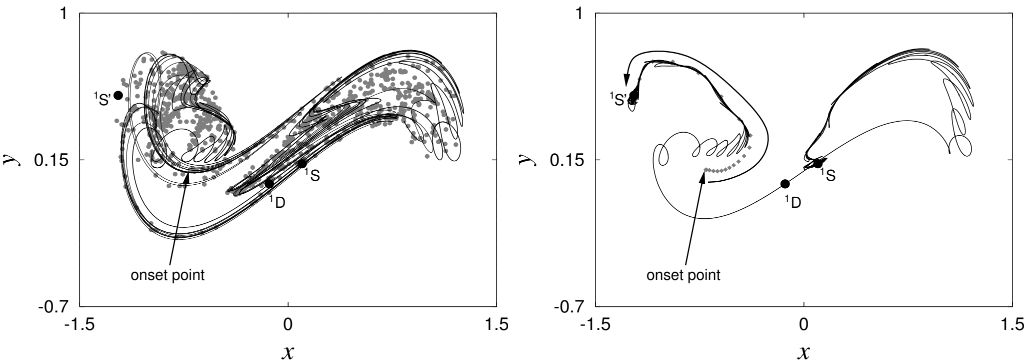

(c) $K = 0.75$ (d) $K = 1.1$

Figure 5.2(Continued): In (c) and (d), targets are stable and stroboscopic points show transient behavior before convergence to a target orbit. Notation of target orbits are changed to $^1\mathsf{S}$ and $^1\mathsf{S}'$ for their stability change. Arrows in (c) and (d) indicate the same stroboscopic point at which the control is activated.

5.3 Influence on control performance

From the viewpoint of control, it is expected that controlled trajectories quickly converge to a target orbit selected preliminarily. However, when the chaotic dynamics persists against the control input, the trajectories wander irregularly between $^1\mathsf{S}$ and $^1\mathsf{S}'$ along the unstable manifold even when the target orbits become stable. In Fig. 5.2(c), we can confirm this by the fact that a trajectory after onset of control is driven along the unstable manifold, as shown by stroboscopic points. Figure 5.3 shows the resulting temporal change of displacement x and control input u. One can see that the controlled trajectory irregularly goes back and forth between $^1\mathsf{S}$ and $^1\mathsf{S}'$ many times, before it eventually converges to $^1\mathsf{S}$.

The steady states obtained by the control are not predictable due to this long and irregular transient behavior. Figure 5.4 shows classification of stroboscopic points by the steady states. Each of the classified stroboscopic point here denotes the state of the system at the onset time of control, which was taken every period-T so that each of the chosen state is on the stroboscopic plane. The stroboscopic points correspond to different initial conditions including the state at the onset time. Different initial conditions for controlled dynamics were determined at every onset time, depending on a segment of a chaotic trajectory generated just before the onset. The controlled trajectories for the chosen initial conditions converged to either ${}^1\mathsf{S}$ or ${}^1\mathsf{S}'$ after transient response. In Fig. 5.4, the stroboscopic points are classified with black and gray tones, which imply convergence to ${}^1\mathsf{S}$ and ${}^1\mathsf{S}'$, respectively. The black and gray points are finely mixed one another all over the original chaotic attractor. The steady states therefore almost randomly alternate between ${}^1\mathsf{S}$ and ${}^1\mathsf{S}'$ with onset timing of control and influence of external disturbance. In addition, since the two types of points are mixed even in the neighborhood of the target orbits, the controlled system is possibly stabilized to the target orbit in the opposite side from the other target, near which the control is activated. The targeting scheme based on linearization has therefore no possibility of effective convergence in the practical situation. These characteristics are obviously disadvantages for engineering use of the control method. However, no detailed discussion for these characteristics has been obtained.

Corresponding to the simple global phase structure in Fig. 5.2(d), the domain of attraction becomes quite simple for $K = 1.1$, as shown in Fig. 5.5. The classification implies that the targeting scheme is effective. Most of the trajectories converge to the target orbit located in their initial sides in the xy-plane, though there are some onset points leading the convergence to the opposite side. The trajectories go into two different sides in the process of approaching to ${}^1\mathsf{D}$. Transient behavior is also much simpler than at $K = 0.75$. Figure 5.6 shows the rapid convergence to a target orbit is achieved under the large amplitude of the feedback gain.

We note that the classification adopted here has tested only initial conditions derived from a chaotic trajectory. In fact, the steady state for a chosen initial condition can be different, if the state of the uncontrolled system is partly modified in the time interval $[t_0 - \tau, t_0]$, where t_0 is onset time of control. Nevertheless, the classification has provided us substantial information on the structure of domain of attraction. Since the uncontrolled system is chaotic, we can classify strobo-

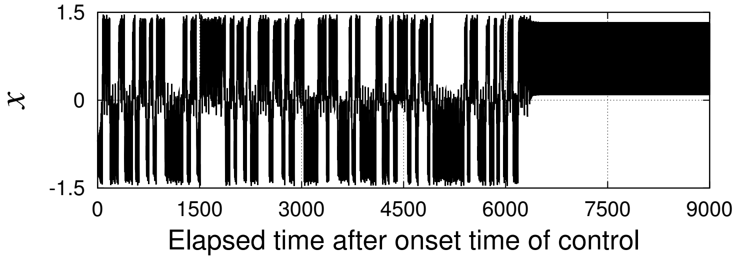

(a) displacement

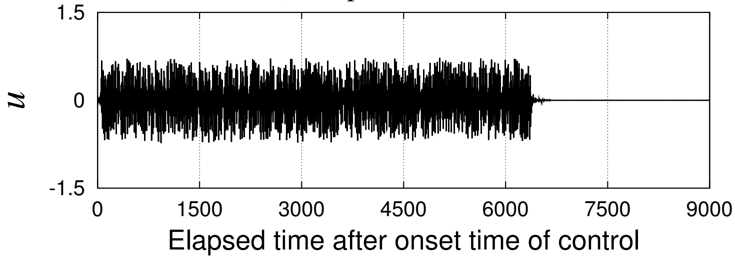

(b) control input

Figure 5.3: Transient behavior in time domain for $K = 0.75$. Scale of time axis (not renormalized) is the same in (a) displacement and (b) control input. Controlled trajectory irregularly goes back and forth between two target orbits before final convergence to $^1\mathrm{S}$, corresponding to chaotic motion of stroboscopic points in Fig. 5.2(c). The same time scale is used in Fig. 5.6

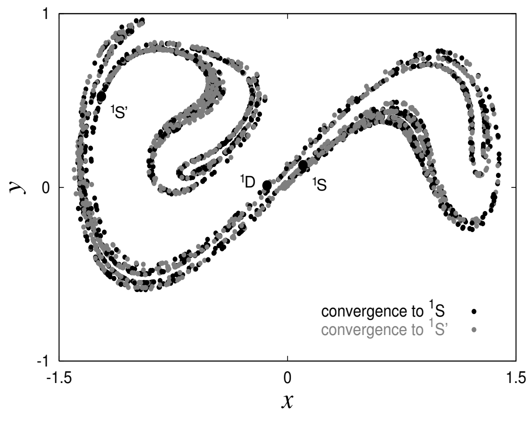

Figure 5.4: Domain of attraction for target orbits at $K = 0.75$. Black and gray points show convergence to $^1\mathrm{S}$ and $^1\mathrm{S}'$, respectively. They are finely mixed one another all over original chaotic attractor.

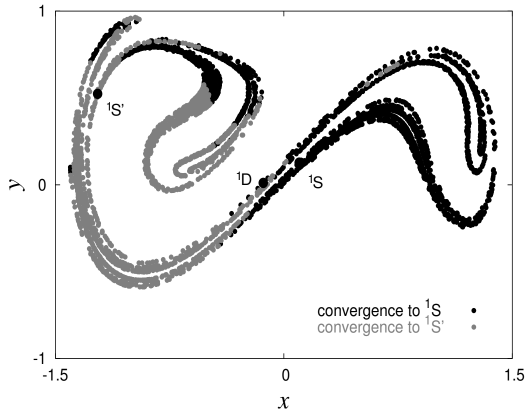

Figure 5.5: Domain of attraction for target orbits at $K = 1.1$. Black and gray points show convergence to $^1\mathsf{S}$ and $^1\mathsf{S}'$, respectively. Most of controlled trajectories converge to target orbit in their initial sides.

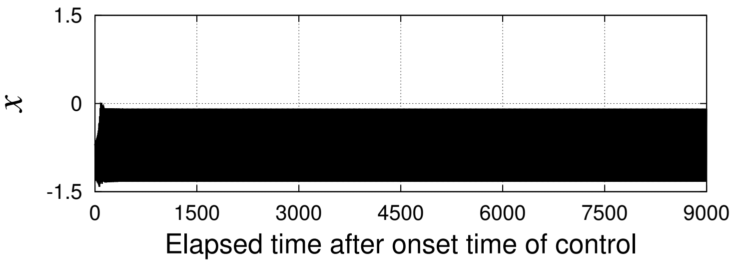

(a) displacement

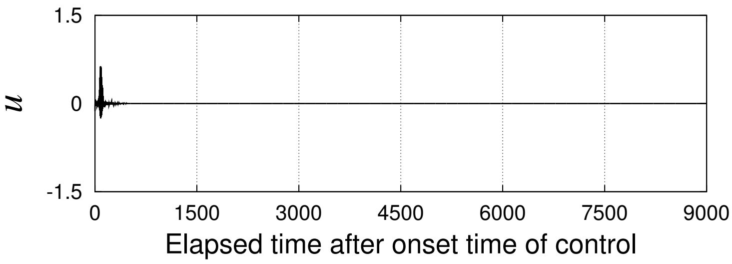

(b) control input

Figure 5.6: Transient behavior for $K = 1.1$. Time scale (not renormalized) is the same as in Fig. 5.3. Corresponding to simple global structure in Fig. 5.2(d), controlled trajectory quickly converges to $^1\mathsf{S}'$ without any irregular behavior.

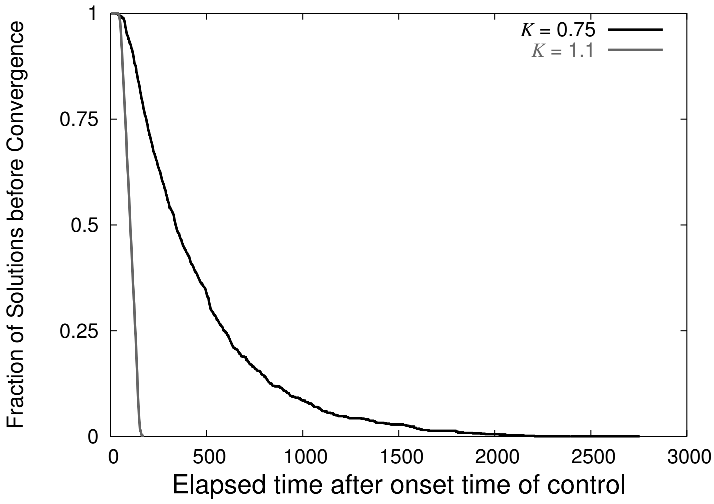

Figure 5.7: Fraction of controlled trajectories before convergence to target orbits in the TV2 case.

scopic points densely plotted over the original chaotic attractor. This implies that the classification in this dissertation was performed for the system under no remarkable external disturbances which can modify the chosen initial conditions within the time interval.

Here transient time is numerically compared with that for $K = 1.1$. Figure 5.7 shows fraction of the controlled trajectories before convergence. We determined the fraction for 1010 different initial conditions uniformly selected from the original chaotic attractor. The criterion of the convergence was that modulus of control signal keeps under 10^{-2} for one period of external forcing. In Fig. 5.7, the decrease of the fraction for $K = 0.75$ is very slow as compared with that for $K = 1.1$. 77 % of the solutions does not converge, when all the solutions for $K = 1.1$ achieve the convergence. 34% of the solutions still keep transient states after 500 period from the onset time of control. The possibility of these long and irregular transient states is obviously disadvantage for the purpose of control.

In this section, we have shown that the transient behavior and domain of attraction accurately reflect the difference in the two global phase structures obtained in

Section 5.1 and Section 5.2. In particular, we have clarified these control characteristics are significantly deteriorated when the original chaotic dynamics persists in the controlled system with the stable target orbits. It should be emphasized that one inevitably takes the global dynamics into account to estimate control performance. This is because the exact model of a chaotic system is often unknown and then control is possibly activated in the region where the linearizion around a target orbit is not justified. The system after activation may exhibit long-term irregular behavior due to the persisting chaotic dynamics, even when the feedback gain is appropriately designed or optimized from the point of stability of target orbits. In other words, one should pay attention to the global dynamics besides stability in understanding the behavior of controlled systems and designing control parameters.

5.4 Concluding remarks

In this chapter, we have numerically discussed the global phase structure of the controlled two-well Duffing system. The one-dimensional unstable manifold gave us substantial information on the global dynamics in function space. A typical scenario was described; the global phase structure changes from the original chaos producing to the simplified structure, as feedback gain is increased. This simplified structure implies that no chaotic behavior occurs even in the transient state. On the other hand, we found a quite interesting case where the original chaotic dynamics persists in the controlled system even when the target orbits are stable. As was pointed out in Section 1.2, the persistence of chaos highly complicates the domain of attraction for the target orbits and causes long chaotic transient behavior. These destructive influences on control performance clearly show the global dynamics in infinite dimensional space should be considered for further extension of the control method. Persistence of chaos, or coexistence of global chaotic dynamics with locally stable target orbits, seems to occur, especially when feedback gain is adjusted near the threshold value of the stability change of the target orbits.

A low pass filter inserted to feedback loop may therefore deteriorate the control performance, while the reduction of high frequency components improves steady state characteristics of the controlled system.

Note that controlling chaos involves the destruction of chaotic attractors as its intrinsic nature. In principle, stability change of target orbits can be achieved without any global bifurcations that ravel the complicated phase structure originally producing a chaotic attractor. As a result, a long chaotic transient occurs as in the case of *boundary crisis* [127, 128], while the different mechanism works behind the destruction. It implies, if chaotic dynamics persists, the success of controlling chaos is governed by a probabilistic law unless control is activated based on the exact knowledge of the local dynamics around target orbits. It seems that the probabilistic law appears as waiting time for the approach of the trajectory to a target orbit.

We lastly recall that chaotic transient [127, 128, 131] and changes in the basin boundaries [132–134] have been connected to the collision and intersection of stable and unstable manifolds emanating from unstable periodic orbits especially in low dimensional systems. However, it is difficult, at least numerically, to identify the collision and intersection of manifolds in the systems with time delay, because the stable manifolds have infinite dimension although the unstable manifolds keep finite dimension in general. This is a reason that made us consider only the unstable manifold of ${}^{1}\mathsf{D}$, nevertheless it has provided essential features of the global dynamics and related control characteristics.

Chapter 6

Annihilation of periodic orbits and general features of global dynamics

This chapter aims to clarify a general feature of the global dynamics in systems under the time-delayed feedback control. The review through the previous chapters suggests a close connection between the annihilation of coexisting orbits in Chapter 3 and the change of the global phase structure in Chapter 5. The global dynamics of the controlled systems is analytically discussed through the effects of control input on the non-target orbits. The harmonic balance analysis of a controlled periodic system demonstrates that the non-target orbits are annihilated or degenerated to the target orbits as feedback gain is increased. Annihilation and degeneration are numerically confirmed in the controlled two-well Duffing system with velocity feedback control.

6.1 Effects of control on non-target orbits

One obvious feature of the control method is that the controlled system has the same number of the target period-T orbits as the uncontrolled system. Nothing other than their stability is changed by control input, as long as the time delay τ is precisely adjusted to T. In particular, the location and the existence are maintained for any feedback gain due to the control input converging to zero under the period-

T states. On the other hand, a question is raised as to how the control input effects on an infinite number of non-target orbits. The control input does not converge to zero for the non-target orbits, and thereby the location and existence cannot be kept in the controlled system. The question must be closely associated with the global dynamics of the controlled system, because the non-target orbits are also embedded in the chaotic attractor together with the targets.

The previous chapters left us the two keys to answer this question. The first is that the coexisting orbits are derived from the non-target unstable periodic orbits embedded in the chaotic attractor and then annihilated by the saddle-node bifurcation in high feedback gain. This was shown by the bifurcation analysis in Chapter 3. The second is that the high feedback gain simultaneously breaks the original chaotic dynamics, as shown in Chapter 5. The greatly simplified unstable manifold of ${}^1\mathsf{D}$ suggests that no periodic orbit persists except the period-T orbits ${}^1\mathsf{I}$, ${}^1\mathsf{I}'$, and ${}^1\mathsf{D}$. The existence of the coexisting orbits therefore seems to be a good indicator to determine whether the original chaotic dynamics persists in the controlled system or not. In particular, no chaotic dynamics arises in the greatly simplified global structure, after all the coexisting orbits are annihilated. One can, in fact, confirm that the unstable manifold in the TV1 case becomes a completely simple curve shown in Fig. 5.1(d) at $K = 1.0$, which is slightly greater than $K = 0.9382$, the saddle-node bifurcation point of the coexisting period-$3T$ orbits. The scenario is summarized in Fig. 6.1. The same scenario is checked in the other cases and this fact motivates us to expect that annihilation of the coexisting orbits and associated simplified global dynamics is a general feature of time-delayed feedback controlled systems. In the next section, we show that the above scenario is generally observed in controlled periodic systems under some assumptions. More precisely, the following of this chapter demonstrates the orbits whose periods are integer multiples of the fundamental period are expected to annihilate or degenerate to the target orbits in the controlled systems.

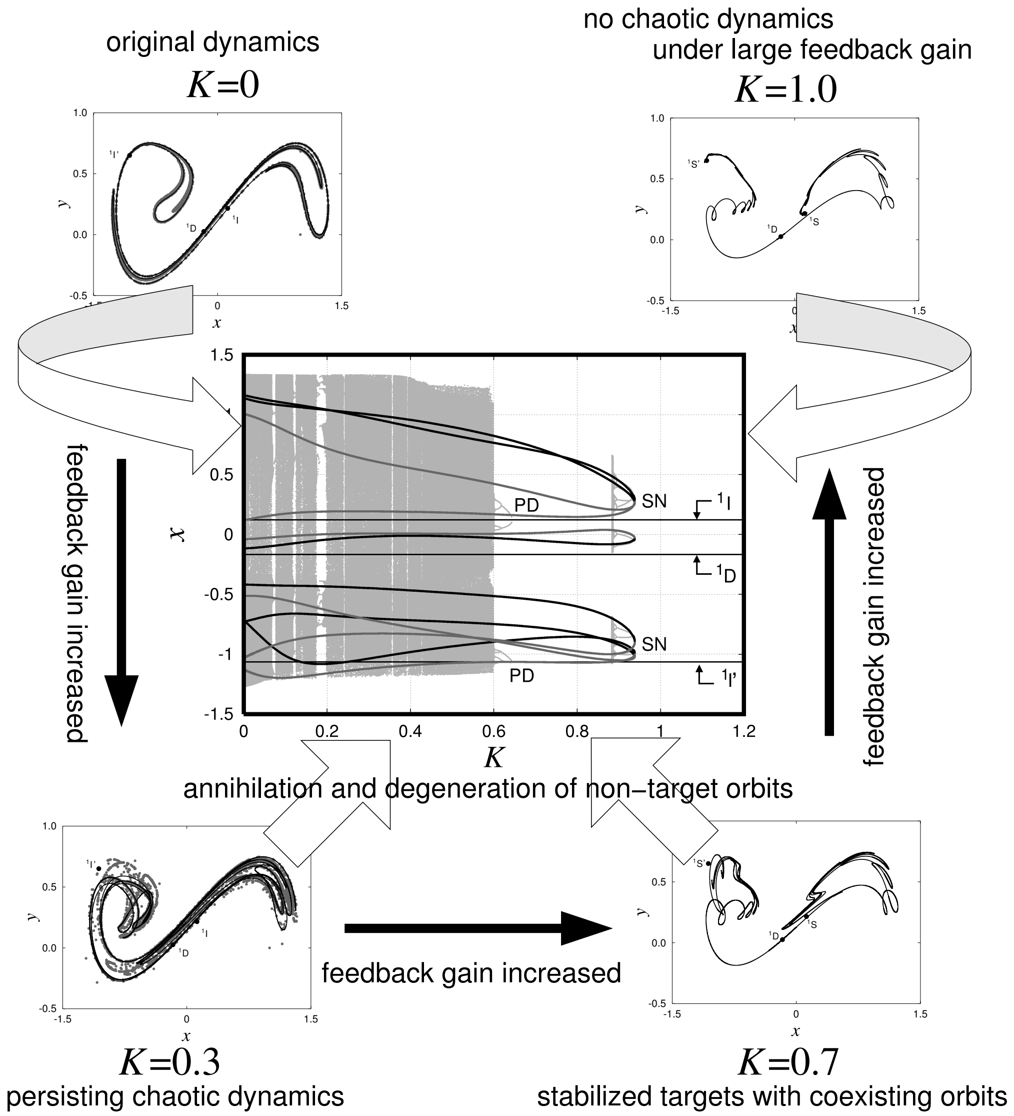

Figure 6.1: Summary of global dynamics of controlled two-well Duffing system shown in Chapter 3 and Chapter 5. The original complicated global structure is simplified as non-target orbits are annihilated from the controlled system. The non-target orbits are initially embedded in the chaotic attractor and then disappear by the saddle-node bifurcation as feedback gain is increased. The same scenario is observed in other cases.

6.2 Harmonic balance analysis of periodic system under control

6.2.1 Harmonic balance method

The harmonic balance method is here applied to discuss the existence of periodic orbits in a controlled periodic system. The harmonic balance method has been a well known approach to analyze nonlinear oscillations in physical systems [135]. A periodic solution of a nonlinear system is represented as a truncated Fourier series expansion with unknown Fourier coefficients. The approximated solution is obtained by determining the coefficients as a solution of nonlinear algebraic equations which are derived by substituting the Fourier series to the differential equation. Although the harmonic balance method is not mathematically rigorous, we here assume that the existence of approximation implies that of true solution without concerning about the rigor. A perspective to mathematical justification is mentioned in the last of this chapter.

6.2.2 Derivation of determining equation

Consider a n-dimensional periodic system under time-delayed feedback control:

$$\begin{cases} \dfrac{\mathrm{d}\boldsymbol{x}}{\mathrm{d}t} = \boldsymbol{f}(t,\, \boldsymbol{x}) + \boldsymbol{u}, \\ \boldsymbol{u} = K[\boldsymbol{x}_\tau - \boldsymbol{x}], \end{cases} \tag{6.1}$$

where $T > 0$ is the least period satisfying $\boldsymbol{f}(t + T,\, \boldsymbol{x}) = \boldsymbol{f}(t,\, \boldsymbol{x})$ for all t, and $\omega = 2\pi/T$. The frequency component of ω is hereafter called *the fundamental frequency component*. We assume that $\boldsymbol{f} : \mathcal{R} \times \mathcal{R}^n \to \mathcal{R}^n$ is a $\mathcal{R}^n$-valued vector polynomial function with respect to $\boldsymbol{x} \in \mathcal{R}^n$ and the maximum degree of polynomials is $p \geq 1$. $\boldsymbol{f}(t,\, \boldsymbol{x})$ is also continuous and sufficiently smooth in t. The time delay τ is here adjusted to the fundamental period T of the system. K denotes n-dimensional diagonal feedback gain matrix, $K = \mathrm{diag}(K_1,\, K_2,\, \cdots,\, K_n)$, $K_{\max} \geq K_j \geq 0$. The above equation is obtained as a special form of Eq. (2.6) and also includes the Duffing systems under control. One can assume that all state variables are measurable without loss of generality. The restriction related to a limited number of measurable outputs can be relaxed by setting the corresponding components of the matrix to zero. One may also rescale the matrix components, when the output $\boldsymbol{g}(\boldsymbol{x})$ is proportional to the current state $\boldsymbol{x}$. For the further discussion, Eq. (6.1) is rewritten as follows:

$$\frac{\mathrm{d}\boldsymbol{x}}{\mathrm{d}t} - \boldsymbol{f}(t,\, \boldsymbol{x}) = K[\boldsymbol{x}_\tau - \boldsymbol{x}]. \tag{6.2}$$

A solution $\boldsymbol{x}(t)$ of the system (6.1) is said to be a period-mT solution, if $\boldsymbol{x}(t)$ satisfies $\boldsymbol{x}(t) = \boldsymbol{x}(t + mT), m \geq 1$, m integer, for all t. For $m \geq 2$, $\boldsymbol{x}(t)$ has $1/m$-order subharmonic component and its higher harmonics. $\boldsymbol{x}(t)$ represents the target solution for $m = 1$. $\boldsymbol{x}(t)$ is periodic and continuously differentiable in t. $\boldsymbol{x}(t)$ can be then represented by the following Fourier series expansion:

$$\boldsymbol{x}(t) = \boldsymbol{a}_0 + \sum_{k=1}^{\infty} \left(\boldsymbol{a}_{2k-1} \cos \frac{k}{m}\omega t + \boldsymbol{a}_{2k} \sin \frac{k}{m}\omega t \right), \tag{6.3}$$

where $\boldsymbol{a}_i = (a_{i1},\, a_{i2},\, \cdots,\, a_{in})^T \in \mathcal{R}^n$, $i = 0,\, 1,\, 2,\, \cdots$, denotes the Fourier coefficient vector satisfying

$$||\boldsymbol{a}||^2 = \sum_{i=0}^{\infty} ||\boldsymbol{a}_i||^2 = \sum_{i=0}^{\infty} \sum_{j=1}^{n} |a_{ij}|^2 < \infty. \tag{6.4}$$

The true solution $\boldsymbol{x}(t)$ is approximated by the following truncated Fourier series expansion $\hat{\boldsymbol{x}}(t)$ according to the harmonic balance method [135]:

$$\hat{\boldsymbol{x}}(t) = \boldsymbol{a}_0 + \sum_{k=1}^{N} \left(\boldsymbol{a}_{2k-1} \cos \frac{k}{m}\omega t + \boldsymbol{a}_{2k} \sin \frac{k}{m}\omega t \right), \tag{6.5}$$

where N is the maximum order of frequency component which should be taken into account to obtain approximate solutions. An arbitrary small error between $\boldsymbol{x}(t)$ and $\hat{\boldsymbol{x}}(t)$ can be achieved by taking sufficient large N. From Eq. (6.5), the $\dfrac{\mathrm{d}\hat{\boldsymbol{x}}}{\mathrm{d}t}$

and $\hat{\boldsymbol{x}}(t-\tau) - \hat{\boldsymbol{x}}(t)$ are obtained as follows:

$$
\begin{aligned}
\frac{\mathrm{d}\hat{\boldsymbol{x}}}{\mathrm{d}t} &= \frac{\omega}{m}\sum_{k=1}^{N}\left(k\boldsymbol{a}_{2k}\cos\frac{k}{m}\omega t - k\boldsymbol{a}_{2k-1}\sin\frac{k}{m}\omega t\right), \qquad (6.6)\\
&\hat{\boldsymbol{x}}(t-\tau) - \hat{\boldsymbol{x}}(t)\\
&= \sum_{k=1}^{N}\Big[\left\{\boldsymbol{a}_{2k-1}\left(\cos\frac{k}{m}\omega\tau - 1\right) - \boldsymbol{a}_{2k}\sin\frac{k}{m}\omega\tau\right\}\\
&\times\cos\frac{k}{m}\omega t + \left\{\boldsymbol{a}_{2k-1}\sin\frac{k}{m}\omega\tau + \boldsymbol{a}_{2k}\left(\cos\frac{k}{m}\omega\tau - 1\right)\right\}\\
&\times\sin\frac{k}{m}\omega t\Big]. \qquad (6.7)
\end{aligned}
$$

Substituting Eqs. (6.5) (6.6) and (6.7) into Eq. (6.2) and equating each frequency component, one can derive the following $2N+1$ equations determining the Fourier coefficient vectors:

$$
\hat{\boldsymbol{\mathcal{F}}}_i^m(\boldsymbol{a}) = K\hat{\boldsymbol{\mathcal{U}}}_i^m(\boldsymbol{a}), \qquad (6.8)
$$

where $\boldsymbol{a} = (\boldsymbol{a}_0^T,\ \boldsymbol{a}_1^T,\ \cdots,\ \boldsymbol{a}_{2N}^T)^T \in \mathcal{R}^{n\times(2N+1)}$ and $i = 0,\ 1,\ \cdots,\ 2N$. The j-th component of $\hat{\boldsymbol{\mathcal{F}}}_i^m(\boldsymbol{a})$ and $\hat{\boldsymbol{\mathcal{U}}}_i^m(\boldsymbol{a})$ are here denoted by $\hat{\mathcal{F}}_{ij}^m(\boldsymbol{a})$ and $\hat{\mathcal{U}}_{ij}^m(\boldsymbol{a})$, respectively. $\hat{\boldsymbol{\mathcal{F}}}_i^m(\boldsymbol{a})$ is defined for the direct current component as follows:

$$
\hat{\boldsymbol{\mathcal{F}}}_0^m(\boldsymbol{a}) = -\frac{1}{mT}\int_0^{mT}\boldsymbol{f}(t,\ \hat{\boldsymbol{x}}(t))\mathrm{d}t. \qquad (6.9)
$$

For the k-th frequency component, we obtain

$$
\begin{cases}
\hat{\boldsymbol{\mathcal{F}}}_{2k-1}^m(\boldsymbol{a}) = \dfrac{\omega}{m}k\boldsymbol{a}_{2k} - \dfrac{2}{mT}\displaystyle\int_0^{mT}\boldsymbol{f}(t,\ \hat{\boldsymbol{x}}(t))\cos\frac{k}{m}\omega t\mathrm{d}t,\\
\hat{\boldsymbol{\mathcal{F}}}_{2k}^m(\boldsymbol{a}) = -\dfrac{\omega}{m}k\boldsymbol{a}_{2k-1} - \dfrac{2}{mT}\displaystyle\int_0^{mT}\boldsymbol{f}(t,\ \hat{\boldsymbol{x}}(t))\sin\frac{k}{m}\omega t\mathrm{d}t,
\end{cases} \qquad (6.10)
$$

for $k = 1,\ 2,\ \cdots,\ N$. As for the control input, the direct current component is given by

$$
\hat{\boldsymbol{\mathcal{U}}}_0^m(\boldsymbol{a}) = 0, \qquad (6.11)
$$

and the k-th order component is

$$\begin{cases} \hat{\boldsymbol{\mathcal{U}}}^m_{2k-1}(\boldsymbol{a}_{2k-1},\, \boldsymbol{a}_{2k}) = \left\{\boldsymbol{a}_{2k-1}\left(\cos\dfrac{k}{m}\omega\tau - 1\right) - \boldsymbol{a}_{2k}\sin\dfrac{k}{m}\omega\tau\right\}, \\ \hat{\boldsymbol{\mathcal{U}}}^m_{2k}(\boldsymbol{a}_{2k-1},\, \boldsymbol{a}_{2k}) = \left\{\boldsymbol{a}_{2k-1}\sin\dfrac{k}{m}\omega\tau + \boldsymbol{a}_{2k}\left(\cos\dfrac{k}{m}\omega\tau - 1\right)\right\}. \end{cases} \tag{6.12}$$

The assumption on $\boldsymbol{f}(t,\, \boldsymbol{x})$ implies that $\hat{\boldsymbol{\mathcal{F}}}^m_i(\boldsymbol{a})$ is a finite dimensional polynomial of degree at most p with respect to $\boldsymbol{a}$. This shows that there exist positive constants M_0 and M_p such that

$$|\hat{\mathcal{F}}^m_{ij}(\boldsymbol{a})| < M_0 + M_p\|\boldsymbol{a}\|^p \tag{6.13}$$

for any $\boldsymbol{a} \in \mathcal{R}^{n\times(2N+1)}$, $i,\, j$ (See, Appendix of this chapter). For simplicity of notation, define the sets of suffix Λ^m_{f} and Λ^m_{s} as

$$\begin{cases} \Lambda^m_{\mathrm{f}} = \{i\,|\, i = 0,\ i = 2qm - 1,\ i = 2qm,\ q = 1,\, 2,\, \cdots,\, q_{\max}\}, \\ \Lambda^m_{\mathrm{s}} = \overline{\Lambda^m_{\mathrm{f}}} \cap \{i\,|\,0 \le i \le 2N + 1\}, \end{cases} \tag{6.14}$$

where $q_{\max}$ is the maximum integer satisfying $N = q_{\max}m + r, 0 \le r < m$, and r integer. Λ^m_{f} denotes the suffix corresponding to the direct current, the fundamental, and its higher harmonic components. Λ^m_{s} is for the subharmonics. Since

$$\cos\frac{i}{m}\omega\tau - 1 = \sin\frac{i}{m}\omega\tau = 0 \tag{6.15}$$

for $i \in \Lambda^m_{\mathrm{f}}$, we have the relation

$$\hat{\boldsymbol{\mathcal{F}}}^m_i(\boldsymbol{a}) = \hat{\boldsymbol{\mathcal{U}}}^m_i(\boldsymbol{a}) = 0 \text{ for all } i \in \Lambda^m_{\mathrm{f}}. \tag{6.16}$$

This relation is a consequence of the control input, which does not include, the direct current component, the fundamental component and its higher harmonics in the steady state. The relation (6.16) constitute a constraint condition for solving the remaining equations for subharmonic components for $i \in \Lambda^m_{\mathrm{s}}$. The condition determines a hyper surface $\mathcal{S}^m$ in $\mathcal{R}^{n\times(2N+1)}$ below.

$$\mathcal{S}^m = \left\{\boldsymbol{a} \in \mathcal{R}^{n\times(2N+1)}\,|\,\hat{\boldsymbol{\mathcal{F}}}_i(\boldsymbol{a}) = \boldsymbol{0},\ i \in \Lambda^m_{\mathrm{f}}\right\}. \tag{6.17}$$

The remaining equation for subharmonics is here called *the determining equation* on $\mathcal{S}^m$. We say $\boldsymbol{a}(K) \in \mathcal{S}^m$ is a solution of Eq. (6.8), if $\boldsymbol{a}$ satisfies the determining equation

$$\begin{cases} \hat{\mathcal{F}}^m_{2k-1}(\boldsymbol{a}) = K\hat{\boldsymbol{\mathcal{U}}}^m_i(\boldsymbol{a}_{2k-1}, \boldsymbol{a}_{2k}), \\ \hat{\mathcal{F}}^m_{2k}(\boldsymbol{a}) = K\hat{\boldsymbol{\mathcal{U}}}^m_i(\boldsymbol{a}_{2k-1}, \boldsymbol{a}_{2k}). \end{cases} \tag{6.18}$$

Since a hyperplane is defined by $\hat{\boldsymbol{\mathcal{U}}}^m_i(\boldsymbol{a}_{2k-1}, \boldsymbol{a}_{2k})$ linear with respect to $\boldsymbol{a}_{2k-1}$ and $\boldsymbol{a}_{2k}$, the solution $\boldsymbol{a}(K)$ is found in the intersection of the hyperplane by $\hat{\boldsymbol{\mathcal{U}}}^m_i(\boldsymbol{a})$ and the hypersurfaces by $\hat{\mathcal{F}}^m_i(\boldsymbol{a})$ and $\mathcal{S}^m$. One has to notice that the determining equation is assumed to have solutions corresponding to those in the uncontrolled system, when $K_{\max} = 0$. The original solutions are denoted by $\boldsymbol{a}(0) = \boldsymbol{a}^* \in \mathcal{S}^m$. One should keep in mind that $\hat{\boldsymbol{\mathcal{U}}}^m_{2k-1}(\boldsymbol{a}_{2k-1}, \boldsymbol{a}_{2k}) = \hat{\boldsymbol{\mathcal{U}}}^m_{2k}(\boldsymbol{a}_{2k-1}, \boldsymbol{a}_{2k}) = \boldsymbol{0}$ for $k \neq 0$ and $k \neq qm$, if and only if $\boldsymbol{a}_{2k-1} = \boldsymbol{a}_{2k} = \boldsymbol{0}$. This is easy to prove using Eq. (6.12). Since K is diagonal, the same fact also holds in each component, that is, $\hat{\mathcal{U}}^m_{2k-1,j}(a_{2k-1,j}, a_{2k,j}) = \hat{\mathcal{U}}^m_{2k,j}(a_{2k-1,j}, a_{2k,j}) = 0$ for $k \neq 0$ and $k \neq qm$, if and only if $a_{2k-1,j} = a_{2k,j} = 0$.

6.2.3 Invariance of target orbits

We first confirm that the existence and location of target orbits are maintained for any feedback gain. For the target orbits, i.e., $m = 1$, the determining equation (6.8) has zero right-hand side in each component; that is,

$$\hat{\mathcal{F}}^m_i(\boldsymbol{a}) = \boldsymbol{0} \tag{6.19}$$

for all i. The solutions $\boldsymbol{a}(K)$ are obviously identical to the original solutions $\boldsymbol{a}^*$ for any K and thereby keep their existence and original location, as feedback gain is increased. This is an immediate consequence of the control input (2.4), which does not include the direct, the fundamental, and its higher harmonics in the steady state; the control input works as a notch filter for these frequency components [49].

6.2.4 Annihilation of coexisting orbits

As for periodic solutions with $m \geq 2$, one can show that they do not exist for large feedback gain under assumptions on the structure of the dynamical system (6.1) below:

(A1) The solutions of Eq. (6.1) is uniformly ultimately bounded under $K_{\max} = 0$ and this also holds for any feedback gain K satisfying $K_{\max} < \kappa$; that is, there is a constant $\beta(K_{\max}) > 0$, $K_{\max} < \kappa$, such that for any $\alpha > 0$, there is a constant $t_1(\alpha) > 0$ such that $\|\boldsymbol{x}(\sigma, \phi)(t)\| \leq \beta(K_{\max})$ for $t \geq \sigma + t_1(\alpha)$ for all $\sigma \in \mathcal{R}$, $\phi \in C$, $|\phi| \leq \alpha$. κ is a threshold feedback gain $\kappa > 0$ sufficiently large for the following discussion.

(A2) There exist constants γ, $0 \leq \gamma < 1$ and $\mu > 0$ such that the $\beta(K_{\max}) \leq \beta(0) + \mu K_{\max}^{\gamma/p}$ for $K_{\max} < \kappa$ where p is the maximum degree of the polynomials in $\boldsymbol{f}(t, \boldsymbol{x})$.

The assumptions imply the solutions of the original system enter into the sphere of radius $\beta(0)$ centered at the origin and the situation is little changed under control within the threshold feedback gain κ. Although κ depends on a system to be controlled, it is ideally assumed that κ takes a sufficiently large value to discuss a general feature of the global dynamics. Since the periodic solutions satisfy $\|\boldsymbol{x}(t)\| \leq \beta(K_{\max})$ from the assumption (A1), the Bessel's inequality and the assumption (A2) define bounds for the solutions of the determining equation as

$$\begin{aligned}
\|\boldsymbol{a}\| = \sqrt{\sum_{i=0}^{2N+1} \|\boldsymbol{a}_i\|^2} &\leq \sqrt{\frac{2}{mT}\int_0^{mT} \|\boldsymbol{x}(t)\|^2 \mathrm{d}t} \leq \sqrt{\frac{2}{mT}\int_0^{mT} \beta(K_{\max})^2 \mathrm{d}t} \\
&\leq \sqrt{2}\beta(K_{\max}) \\
&\leq \sqrt{2}(\beta(0) + \mu K_{\max}^{\gamma/p})
\end{aligned} \tag{6.20}$$

for $K_{\max} < \kappa$. The solutions can thus exist in $\mathcal{B}^m(K_{\max})$ given by

$$\mathcal{B}^m(K_{\max}) = \mathcal{S}^m \cap \left\{\boldsymbol{a} \in \mathcal{R}^{n\times(2N+1)} \,|\, \|\boldsymbol{a}\| \leq \sqrt{2}(\beta(0) + \mu K_{\max}^{\gamma/p})\right\}, \tag{6.21}$$

the set of $\boldsymbol{a} \in \mathcal{R}^{n\times(2N+1)}$ satisfying the bounds (6.20) and the constraint condition (6.16). The assumption (A2) determines the rate of increase of $\beta(K_{\max})$ for feedback gain, which depends on the dissipative nature of the original system and feedback signal.

The above assumptions enable us to show the nonexistence of solutions including subharmonic components. For a given $\delta > 0$, we here try to find a solution in $\mathcal{B}^m(K_{\max}) \cap \mathcal{B}^m_\delta$ where

$$\mathcal{B}^m_\delta = \left\{ \boldsymbol{a} \in \mathcal{R}^{n\times(2N+1)} \,\Big|\, \sum_{i\in\Lambda^m_{\mathrm{s}}}^{N} \|\boldsymbol{a}_i\|^2 > \delta,\ \delta > 0 \right\} \tag{6.22}$$

for $K_{\max}$ sufficiently large. For any $\boldsymbol{a} \in \mathcal{B}^m(K_{\max}) \cap \mathcal{B}^m_\delta$, one can find $i \in \Lambda^m_{\mathrm{s}}$, j, and constant $\lambda > 0$ which satisfies $|\hat{\mathcal{U}}^m_{ij}(a_{2k-1,\,j},\, a_{2k,\,j})| > \lambda = \lambda(\delta)$, where $i = 2k-1$ or $i = 2k$, since there is $i \in \Lambda^m_{\mathrm{s}}$ such that $\boldsymbol{a}_i$ has at least one non-zero component due to $\delta > 0$. Then, there exists $K_j = K_{\max}(\lambda) > 0$ such that

$$\begin{aligned} |\hat{\mathcal{F}}^m_{ij}(\boldsymbol{a}) - K_{\max}\hat{\mathcal{U}}^m_{ij}(a_{2k-1,\,j},\, a_{2k,\,j})| &\geq \left| |\hat{\mathcal{F}}^m_{ij}(\boldsymbol{a})| - |K_{\max}\hat{\mathcal{U}}^m_{ij}(a_{2k-1,\,j},\, a_{2k,\,j})| \right| \\ &= \left| |\hat{\mathcal{F}}^m_{ij}(\boldsymbol{a})| - K_{\max}|\hat{\mathcal{U}}^m_{ij}(a_{2k-1,\,j},\, a_{2k,\,j})| \right| \\ &> 0 \end{aligned} \tag{6.23}$$

for any $\boldsymbol{a} \in \mathcal{B}^m(K_{\max}) \cap \mathcal{B}^m_\delta$, where K_j is replaced with $K_{\max}$ without loss of generality. This immediately follows from the inequality below. Since $\lambda > 0$ is independent of $K_{\max}$, $(\gamma-1)/p < 0$, and $|\hat{\mathcal{F}}^m_{ij}(\boldsymbol{a})|$ is estimated by Eq. (6.13) and the assumption (A2), a sufficient large $K_{\max}$ implies

$$\begin{aligned} |\hat{\mathcal{F}}^m_{ij}(\boldsymbol{a})| - K_{\max}|\hat{\mathcal{U}}^m_{ij}(a_{2k-1,\,j},\, a_{2k,\,j})| &< |\hat{\mathcal{F}}^m_{ij}(\boldsymbol{a})| - \lambda K_{\max} \\ &< M_0 + M_p\|\boldsymbol{a}\|^p - \lambda K_{\max} \\ &\leq M_0 + \sqrt{2}M_p(\beta(0) + \mu K_{\max}^{\gamma/p})^p - \lambda K_{\max} \\ &= K_{\max}\left[-\lambda + \frac{M_0}{K_{\max}} + \sqrt{2}M_p\left(\frac{\beta(0)}{K_{\max}^{1/p}} + \mu\frac{1}{K_{\max}^{(1-\gamma)/p}} \right)^p \right] \\ &< 0 \end{aligned} \tag{6.24}$$

for any $\boldsymbol{a} \in \mathcal{B}^m(K_{\max}) \cap \mathcal{B}^m_\delta$. It is thus concluded that no solution of the determining equation (6.8) including subharmonic components is found in $\boldsymbol{a} \in \mathcal{B}^m(K_{\max}) \cap \mathcal{B}^m_\delta$ for sufficiently large $K_{\max}$. The above discussion applies to any $m \geq 2$ and therefore the period-mT solutions in the uncontrolled system must be annihilated, as feedback gain is increased. Note that the above discussion implicitly assumes that appropriate components of $\boldsymbol{x}$ are measured so that we can choose K_j as $K_{\max}$ to annihilate the solutions with subharmonics components.

6.2.5 Degeneration to target orbits

There seems to be another possibility that the periodic solutions with subharmonic components coincides with the target orbits for large feedback gain. The situation occurs if all subharmonic components vanish, as the feedback gain is increased. Since no existence of the solutions was proved by supposing the persistence of subharmonics with arbitrarily given $\delta > 0$, the remaining possibility is that the solutions converge to those in $\mathcal{B}^m \cap \mathcal{B}^m_0$. The solutions in $\mathcal{B}^m_0$, however, satisfy

$$\begin{aligned}\hat{\boldsymbol{x}}(t) &= \boldsymbol{a}_0 + \sum_{q=1}^{q_{\max}} \Big(\boldsymbol{a}_{2qm-1} \cos q\omega t + \boldsymbol{a}_{2qm} \sin q\omega t \Big), \\ &= \hat{\boldsymbol{x}}(t+T). \end{aligned} \tag{6.25}$$

$\hat{\boldsymbol{x}}(t)$ thus coincides with the target period-T orbits; that is, the period-mT solutions with vanishing subharmonics must be degenerated to the target orbits as feedback gain is increased. Although the rate of the convergence to targets is difficult to estimate, it is natural to expect that $\hat{\boldsymbol{x}}(t)$ converges to the targets in finite $K_{\max}$, if the degree of the polynomials in $\boldsymbol{f}(t, \boldsymbol{x})$ is $p \geq 2$. The behavior of the solution $\boldsymbol{a}$ for $K_{\max}$ in the neighborhood of the the targets can be reduced to the solutions of a quadratic equation.

6.2.6 General features of the global dynamics

The previous sections have given a general explanation to the effects of the control input on the unstable periodic orbits embedded in the chaotic attractor. The control input maintains the existence, location, and number of the target orbits and simultaneously annihilates or degenerates the non-target orbits with $1/m$-order subharmonics and its higher harmonics from the controlled system. The original chaotic dynamics then does not exist in the controlled system under sufficiently large feedback gain, since all of the non-target orbits derived from the chaotic attractor are annihilated or degenerated to the target orbits. This allows us to expect the realization of a simple global phase structure and resulting improved control performance, which were observed in Chapter 5. The annihilation and degeneration are thus a promising explanation for why the experiments have succeeded so far from viewpoint of the global dynamics. It is noted that the assumptions (A1) and (A2) give structures of systems tractable for the control method from the viewpoint of the global dynamics; however, (A2) should be more sophisticated for the theoretical application. It is noted that the generation of new periodic orbits and their bifurcation are not forbidden in the previous discussion. In particular, the discussion excluded the periodic solutions with an irrational frequency and quasi-periodic solutions. These solutions can be an alternative steady state for the target orbits, which should be unstable for too large feedback gain. In fact, we can find a stable quasi-periodic solution in the TD1 case as shown in Fig. 6.2. The quasi-periodic solution is generated by the Neimark-Sacker bifurcation of a target orbit after the annihilation and degeneration of all non-target orbits.

6.3 Numerical example

We here apply the harmonic balance method to approximate period-$3T$ orbits and period-$2T$ ones in a two-well Duffing system under velocity feedback control as follows:

$$\begin{cases} \dfrac{\mathrm{d}x}{\mathrm{d}t} = y(t), \\ \dfrac{\mathrm{d}y}{\mathrm{d}t} = -\delta y(t) + x(t) - x(t)^3 + A\cos\omega t + u(t), \\ u(t) = K[y(t-\tau) - y(t)]. \end{cases} \tag{6.26}$$

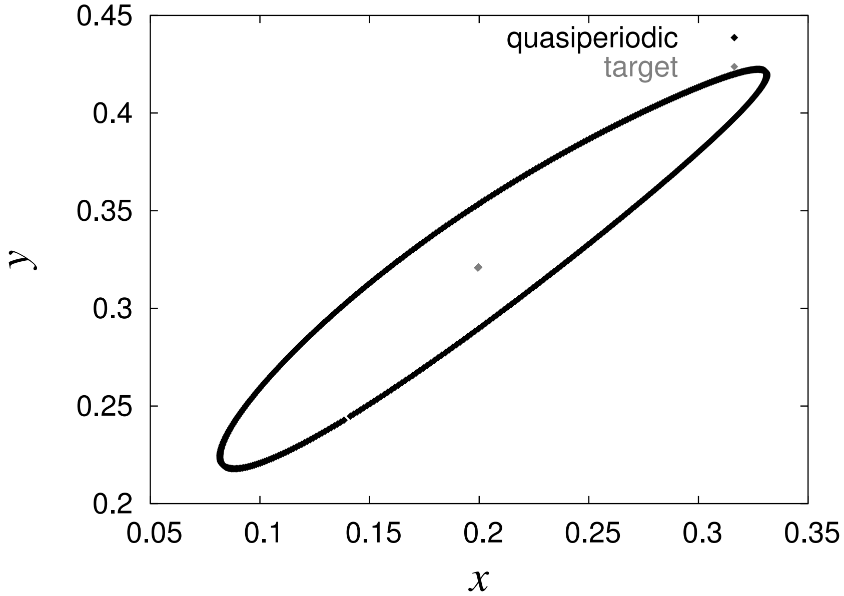

Figure 6.2: Quasi-periodic orbit in the TD1 case at $K = 0.9$ on stroboscopic map. The orbit is generated by the Neimark-Sacker bifurcation of the target orbit after annihilation and degeneration of all non-target orbits.

The solutions of the two-well Duffing system is uniformly ultimately bounded and there is $\kappa > 0$ such that the controlled system holds this property for $K < \kappa$ (See, the appendix of this chapter). The parameters of the TV1 case are used to find the roots of the determining equations.

Consider a truncated Fourier series with $1/3$ subharmonics as follows:

$$x(t) = A_0 + A_1 \cos \frac{1}{3}t + B_1 \sin \frac{1}{3}t + A_2 \cos t + B_2 \sin t. \tag{6.27}$$

Substituting Eq.(6.27) into Eq.(6.26) and equating each component, one can derive the following equations:

$$A_0\left(A_0^2 + \frac{3}{2}A_1^2 + \frac{3}{2}B_1^2 + \frac{3}{2}A_2^2 + \frac{3}{2}B_2^2\right) - A_0 = 0, \tag{6.28}$$

$$\begin{aligned} 3A_1\left(A_0^2 + \frac{1}{4}A_1^2 + \frac{1}{4}B_1^2 + \frac{1}{2}A_2^2 + \frac{1}{2}B_2^2\right) - \frac{10}{9}A_1 + \frac{\delta}{3}B_1 & \\ + \frac{3}{4}A_2(A_1^2 - B_1^2) + \frac{3}{2}A_1B_1B_2 = \frac{K}{2}\left(\frac{A_1}{\sqrt{3}} - B_1\right)&, \end{aligned} \tag{6.29}$$

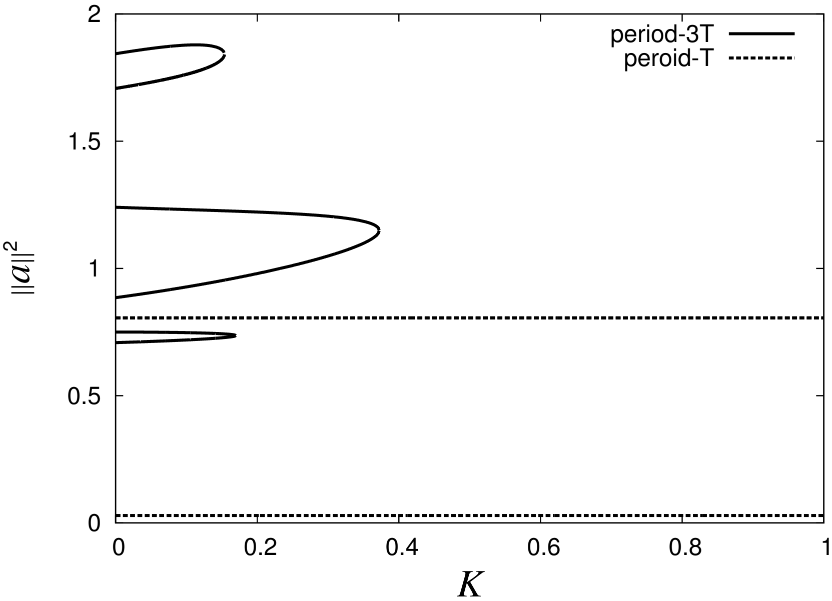

Figure 6.3: Amplitude characteristic of approximated non-target period-3T orbits (solid) and target period-T orbits (dashed). The approximated non-target solutions are extinct in high feedback gain, whereas the target solution persists for any feedback gain.

$$\begin{aligned} &3B_1\left(A_0^2+\frac{1}{4}A_1^2+\frac{1}{4}B_1^2+\frac{1}{2}A_2^2+\frac{1}{2}B_2^2\right)-\frac{\delta}{3}A_1-\frac{10}{9}B_1 \\ &\qquad +\frac{3}{4}B_2(A_1^2-B_1^2)-\frac{3}{2}A_1A_2B_1=\frac{K}{2}\left(A_1+\frac{B_1}{\sqrt{3}}\right), \end{aligned} \tag{6.30}$$

$$\begin{aligned} &3A_2\left(A_0^2+\frac{1}{4}A_1^2+\frac{1}{4}B_1^2+\frac{1}{2}A_2^2+\frac{1}{2}B_2^2\right) \\ &\qquad +\frac{1}{4}B_1(3B_1^2-A_1^2)-2A_2+\delta B_2-B=0, \end{aligned} \tag{6.31}$$

$$\begin{aligned} &3B_2\left(A_0^2+\frac{1}{2}A_1^2+\frac{1}{2}B_1^2+\frac{1}{4}A_2^2+\frac{1}{4}B_2^2\right) \\ &\qquad +\frac{1}{4}B_1(B_1^2-3A_1^2)-\delta A_2-2B_2=0, \end{aligned} \tag{6.32}$$

Figure 6.3 shows amplitude characteristics of approximated target period-T orbits and non-target period-3T orbits obtained by numerically solving the determining

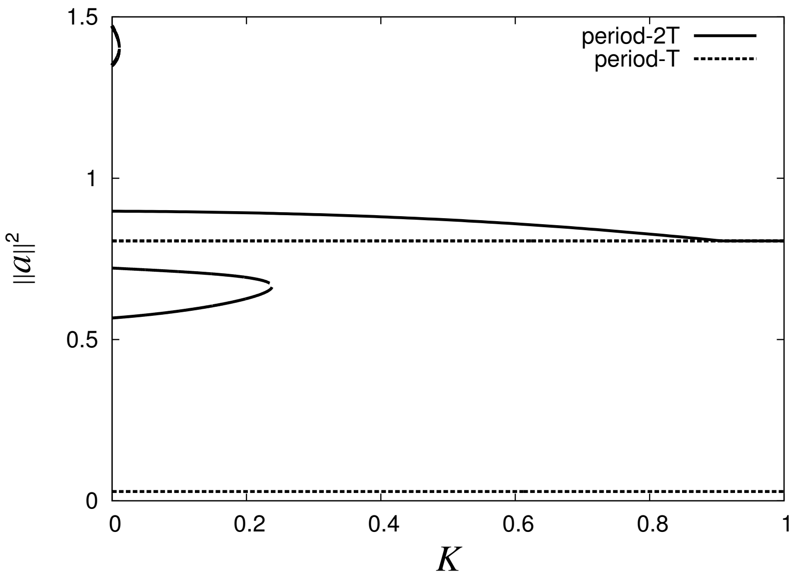

Figure 6.4: Amplitude characteristic of approximated non-target period-$2T$ orbits (solid) and target period-T orbits (dashed). One of the non-target orbits converges to a target orbit. The other two are annihilated as feedback gain is increased.

equations (6.28) to (6.32). Each solid curve shows an amplitude characteristic of a period-$3T$ orbit. We observe six period-$3T$ curves having roots in $K = 0$ and then confirm that each curve is annihilated with colliding with another one, as feedback gain is increased. On the other hand, the orbits with period-T denoted by the dashed line do not change their location for any feedback gain.

The approximated period-$2T$ solutions exhibit the degeneration to the target orbits. The truncated Fourier expansion and the determining equations are listed below:

$$x(t) = A_0 + A_1 \cos t + B_1 \sin t + A_2 \cos \frac{1}{2}t + B_2 \sin \frac{1}{2}t. \tag{6.33}$$

$$4A_0^3 + A_0(-4 + 6A_2^2 + 6A_1^2 + 6B_2^2 + 6B_1^2) + 6A_1B_1B_2 + 3A_2(A_1^2 - B_1^2) = 0, \quad (6.34)$$

$$3A_1^3 + A_1(-5 + 12A_0^2 + 12A_0A_2 + 6A_2^2 + 3B_1^2 + 6B_2^2) + 12A_0B_1B_2 + 2\delta B_1 = -4KB_1, \quad (6.35)$$

$$3B_1^3 + B_1(-5 + 12A_0^2 - 12A_0A_2 + 6A_2^2 + 3A_1^2 + 6B_2^2) + 12A_0A_1B_2 - 2\delta A_1 = 4KA_1, \quad (6.36)$$

$$3A_2^3 + A_2(-8 + 12A_0^2 + 6A_1^2 + 6B_1^2 + 3B_2^2) + 6A_0(A_1^2 - B_1^2) + 4B_2\delta - 4B = 0, \quad (6.37)$$

$$3B_2^3 + B_2(-8 + 12A_0^2 + 6A_1^2 + 6B_1^2 + 3A_2^2) + 12A_0A_1B_1 - 4A_2\delta = 0. \quad (6.38)$$

In Fig. 6.4, we can see one of the period-$2T$ curves coincides with a period-T curve, while the other two curves are annihilated. The results are consistent with that of the harmonic balance analysis and also qualitatively agrees with the previous results in Chapter 3.

6.4 Concluding remarks

In this chapter, we have discussed the effect of control input on the non-target unstable periodic orbits embedded in the original chaotic attractor. The frequency domain approach clarified general features of the global dynamics observed in the previous chapters. It is noted that a standard frequency domain approach was also employed for analysis on the time-delayed feedback controlled system [136]. The crucial difference is that the effects on the non-target orbits were discussed in this chapter and then elucidated the general features of the global dynamics. The increase of feedback gain makes the non-target orbits annihilated or degenerated to the target orbits. The annihilation and degeneration suggests that the global phase structure under control become simple as feedback gain is increased. It is also noted that the harmonic balance method can be mathematically rigorous. Although the existence of approximated solutions was discussed in this chapter, the harmonic balance method, or more generally the describing function method, can rigorously prove the existence of periodic solutions under appropriate assumptions on the nonlinear part of the system [137, 138]. The framework proposed here can therefore provide a useful tool to analyze the global dynamics of time-delayed feedback controlled systems.

Appendix to derivation of bounds for polynomials

The bounds (6.13) for the polynomials of degree p is obtained as follows. The polynomials are written by

$$h(\boldsymbol{x}) = h(x_1,\ x_2,\ \cdots,\ x_n) = \sum_{k=0}^{p} \left(\sum_{p_1+\cdots+p_n=k} a_{p_1\cdots p_n} x_1^{p_1} x_2^{p_2} \cdots x_n^{p_n} \right),$$

where $x_i \in \mathcal{R}, i = 1,\ 2,\ \cdots,\ n$. $p_i \geq 0$ is an integer, and $a_{p_1\cdots p_n}$ denotes coefficients of each term. For the estimation below, we introduce the maximum norm $\|\boldsymbol{x}\|_\infty = \max|x_i|$, which is equivalent to the Euclid norm $\|\boldsymbol{x}\| = \sqrt{\sum_{i=1}^{n}|x_i|^2}$, since $\|\boldsymbol{x}\|/\sqrt{n} \leq \|\boldsymbol{x}\|_\infty \leq \|\boldsymbol{x}\|$ and $\|\boldsymbol{x}\|_\infty \leq \|\boldsymbol{x}\| \leq \sqrt{n}\|\boldsymbol{x}\|_\infty$. For any $\boldsymbol{x} \in \mathcal{R}^n$, the triangle inequality is applied and then we have

$$\begin{aligned}
&|h(\boldsymbol{x})| \\
&\quad \leq \left| \sum_{p_1+\cdots+p_n=p} a_{p_1\cdots p_n} x_1^{p_1} x_2^{p_2} \cdots x_n^{p_n} + \sum_{k=0}^{p-1} \left(\sum_{p_1+\cdots+p_n=k} a_{p_1\cdots p_n} x_1^{p_1} x_2^{p_2} \cdots x_n^{p_n} \right) \right| \\
&\quad \leq \sum_{p_1+\cdots+p_n=p} |a_{p_1\cdots p_n}| |x_1|^{p_1} |x_2|^{p_2} \cdots |x_n|^{p_n} \\
&\qquad\qquad + \sum_{k=0}^{p-1} \left(\sum_{p_1+\cdots+p_n=k} |a_{p_1\cdots p_n}| |x_1|^{p_1} |x_2|^{p_2} \cdots |x_n|^{p_n} \right).
\end{aligned}$$

Since $|x_i| \leq \|\boldsymbol{x}\|_\infty$, we continue the estimation by introducing the relation $|x_i|^{p_i} \leq \|\boldsymbol{x}\|_\infty^{p_i}$, which implies $|x_1|^{p_1} \cdots |x_n|^{p_n} \leq \|\boldsymbol{x}\|_\infty^{p_1+\cdots+p_n} = \|\boldsymbol{x}\|_\infty^k$, as follows:

$$\begin{aligned} |h(\boldsymbol{x})| &\leq \left(\sum_{p_1+\cdots+p_n=p} |a_{p_1\cdots p_n}| \right) \|\boldsymbol{x}\|_\infty^p + \sum_{k=0}^{p-1} \left(\sum_{p_1+\cdots+p_n=k} |a_{p_1\cdots p_n}| \right) \|\boldsymbol{x}\|_\infty^k \\ &= N_p \|\boldsymbol{x}\|_\infty^p + \sum_{k=0}^{p-1} N_k \|\boldsymbol{x}\|_\infty^k, \end{aligned}$$

where $N_k = \sum_{p_1+\cdots+p_n=k} |a_{p_1\cdots p_n}|$. If we assume $\|\boldsymbol{x}\|_\infty > 1$, $\|\boldsymbol{x}\|_\infty^p > \|\boldsymbol{x}\|_\infty^k$ for $p > k$. Then,

$$\begin{aligned} |h(\boldsymbol{x})| &< N_p \|\boldsymbol{x}\|_\infty^p + \left(\sum_{k=0}^{p-1} N_k \right) \|\boldsymbol{x}\|_\infty^p = \left(\sum_{k=0}^{p} N_k \right) \|\boldsymbol{x}\|_\infty^p \\ &= \left(\sum_{k=0}^{p} N_k \right) \|\boldsymbol{x}\|^p. \end{aligned}$$

Note that, for $\|\boldsymbol{x}\|_\infty \leq 1$, $|h(x)|$ has the maximum $M_0 \geq 0$ since $|h(\boldsymbol{x})|$ is continuous in every bounded closed domain in $\mathcal{R}^n$. It is thus concluded that, for any $\boldsymbol{x} \in \mathcal{R}^n$, the bounds for the polynomial of degree p is given by

$$|h(\boldsymbol{x})| \leq M_0 + M_p \|\boldsymbol{x}\|^p,$$

where $M_p = \sum_{k=0}^{p} N_k$.

Appendix to uniform ultimate boundedness of controlled systems

The existence of κ is proved based on the Lyapunov-Razumikhin theory, which is an extension of the Lyapunov theory of ordinary differential equations to the RFDEs [70, 71]. The following theorem gives a sufficient condition for the uniform ultimate boundedness of the solutions of the RFDEs.

Theorem [70, 71] *Suppose $f : \mathcal{R} \times C \to \mathcal{R}^n$ takes $\mathcal{R}\times$(bounded sets of C) into bounded sets of $\mathcal{R}^n$ and consider the RFDE $\dot{x} = f(t, x_t)$. Suppose $u, v, w : \mathcal{R}^+ \to \mathcal{R}^+$ are continuous nondecreasing functions, $u(s) \to \infty$ as $s \to \infty$. If there is a continuous function $V : \mathcal{R} \times \mathcal{R}^n \to \mathcal{R}$, a continuous nondecreasing function $p : \mathcal{R}^+ \to \mathcal{R}^+$, $p(s) > s$ for $s > 0$, and a constant $H \geq 0$ such that*

$$u(|x|) \leq V(t, x) \leq v(|x|), \quad t \in \mathcal{R},\ x \in \mathcal{R}^n \tag{6.39}$$

and

$$\dot{V}(t, \phi) \leq -w(|\phi(0)|) \tag{6.40}$$

if

$$|\phi(\theta)| \geq H, \quad V(t + \theta, \phi(\theta)) < p(V(t, \phi(0))),\ \theta \in [-r, 0] \tag{6.41}$$

then the solutions of the RFDE are uniformly ultimately bounded.

The theorem is generalized so that one can ensure the uniform ultimate boundedness of a specific coordinate $x_i \in \mathcal{R}$ by verifying the following condition.

$$\dot{V}(t, \phi) \leq -w(|\phi_i(0)|)$$

if $|\phi_i(\theta)| \geq H$, $V(t + \theta, x_1, \cdots, \phi_i(\theta), \cdots, x_n)) < p(V(t, x_1, \cdots, \phi_i(0), \cdots, x_n)))$ for $\theta \in [-r, 0]$ [70, 71]. An example is described on pp.134-135 in Ref. [70] and pp.159-160 in Ref. [71] and the proof below is its direct application.

Consider a second order system under velocity feedback control

$$\begin{cases} \dot{x}(t) = y(t), \\ \dot{y}(t) = -\Phi(t, y(t)) - f(x(t)) + e(t) + K[y(t - \tau) - y(t)], \end{cases}$$

where $K \geq 0$ is feedback gain. It is shown that there is $\kappa > 0$ such that the solutions of the above equation are uniformly ultimately bounded for $K < \kappa$ under the assumptions below.

(A0) The solutions satisfy a uniqueness.

(A1) $\Phi : \mathcal{R}^2 \to \mathcal{R}$ is continuous and Φ maps bounded sets of $\mathcal{R}$ into bounded sets with respect to the second argument of Φ. In addition, there are positive constants $a > 0$ and $H > 0$ such that

$$\frac{\Phi(t, y)}{y} > a > 0 \quad \text{for} \quad |y| \geq H$$

(A2) $f : \mathcal{R} \to \mathcal{R}$ is continuous and $f(x)\mathrm{sgn}x \to \infty$ as $x \to \infty$, where $\mathrm{sgn}x$ is the signum function.

(A3) $p : \mathcal{R} \to \mathcal{R}$ is continuous and $|e(t)| \leq k$ for all $t \in \mathcal{R}$.

The two-well Duffing equation (2.3) with velocity feedback satisfy these assumptions, since $\Phi(t, y) = \delta y$, $\delta > 0$, $f(x) = x^3 - x$, and $e(t) = A\cos\omega t$.

We first take a function as $V(x, y) = F(x) + y^2/2$, $F(x) = \int_0^x f(s)\mathrm{d}s$ to prove the uniform ultimate boundedness of the y coordinate. If $q > 1$ and $a + K > Kq$, the time derivative of $V(x, y)$ is estimated as follows:

$$\begin{aligned}
\dot{V}(x(t), y(t)) &= f(x(t))\dot{x}(t) + y\dot{y}(t) \\
&= -y\Phi(t, y(t)) + y(t)e(t) + Ky(t)[y(t-\tau) - y(t)] \\
&< -[(a + K) - Kq]|y(t)|^2 + k|y(t)|,
\end{aligned}$$

if $|y(t)| \geq H$ and $|y(t-\tau)| \leq q|y(t)|$. The latter condition corresponds the existence of the continuous nondecreasing function p of the theorem above. We define $p(s) = q^2 s > s$, $s > 0$. If $a + K > Kq$, one can choose a positive constant μ and $H_1 \geq H$ such that

$$\dot{V}(x(t), y(t)) < -\mu|y(t)|^2 < 0 \tag{6.42}$$

for $|y(t)| \geq H_1 \geq H$. This implies the y coordinate of the solutions is uniformly ultimately bounded and therefore there is $c > 0$ such that $|y(t)| \leq c$ for sufficiently large t.

If $|y(t)| \leq c$, one can show the uniformly ultimately boundedness of the x coordinate with $V_1(x, y) = V(x, y) + y$ and $V_2(x, y) = V(x, y) - y$. There is a constant $k_1 > 0$ such that

$$\begin{aligned}\dot{V}_1(x(t), y(t)) &= \dot{V}(x(t), y(t)) + \dot{y}(t) \\ &= \dot{V}(x(t), y(t)) - \Phi(t, y(t)) - f(x(t)) + e(t) \\ &\leq -f(x(t)) + k_1.\end{aligned}$$

The assumption (A2) implies one can choose $b_1 > 0$ such that $\dot{V}_1(x(t), y(t)) < -1$ if $x(t) \geq b_1$. The x coordinate of the solutions is therefore $x(t) \leq \alpha$ in $|y(t)| \leq c$ for a positive constant α. $V_2(x, y)$ also shows $x(t) \geq -\alpha$ in $|y(t)| \leq c$ in the same way. This immediately implies the solutions are uniformly ultimately bounded if $a + K > Kq$. κ is chosen as $\kappa = \dfrac{a}{q-1} > 0$.

Chapter 7

Application to control of microcantilever oscillation in dynamic force microscopy

This chapter presents a novel application of the time-delayed feedback control to a nanoengineering system, called the dynamic force microscopy (DFM). The stabilization of unstable periodic oscillation intrinsic to the microcantilever sensors enables us to extend operating range of the DFM. The controlled DFM is allowed to operate even in a parameter range, where chaotic microcantilever oscillations possibly occur without control. In addition, the control method is shown to have an ability to improve the transient response of microcantilever oscillation without reducing force sensitivity. The control input converging to null in steady state provides one way to overcome a trade-off between the scanning rate and force sensitivity of the DFM.

7.1 Dynamic force microscope

A brief introduction of the principle of DFM, or dynamic mode AFM, has to be placed in the beginning of this chapter. A schematic diagram of the DFM in Fig. 7.1 is employed for this purpose. One of the most important device of the DFM is a microcantilever with a sharp tip manufactured at its free-end. The

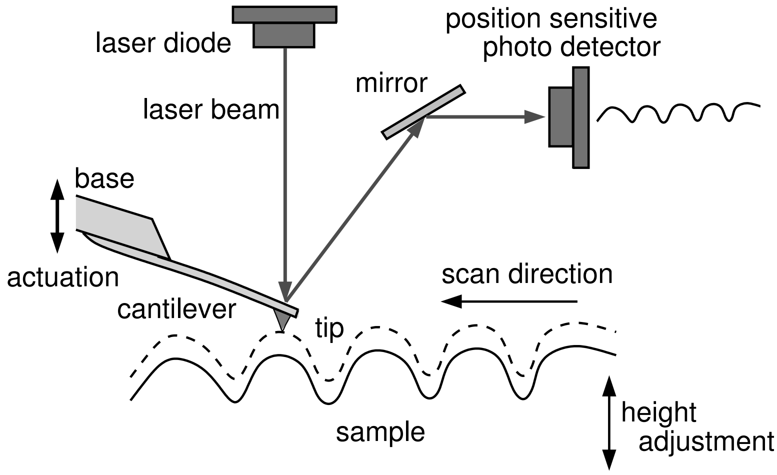

Figure 7.1: Schematic diagram of dynamic force microscopy. Sample surface is scanned by microcantilever probe vibrating at its resonance frequency. During surface scan, mean distance between apex of tip and surface of sample is kept constant with a positioning device, which adjusts vertical position of surface, so that constant shift of resonance frequency is maintained. Time series of signal applied to positioning device provides topography of sample surface. Vibration of microcantilever is measured by optical lever method [72] in standard device configuration.

tip is extremely sharpen to have a typical radius around 10 nm using the microfabrication technique recently. The microcantilever is placed over a sample surface one wish to observe, so that the tip can feel a force between the tip and the atoms or molecules on the sample surface. The force, called *tip-sample interaction*, is so tiny as pico or nano Newton, but it is sufficient to modify the deflection of the microcantilever due to its small dimension.

Since the tip-sample interaction depends on the tip-sample distance, one can maintain the tip-sample distance by adjusting the height of the sample surface with keeping a constant deflection, which is called set-point or reference. The topography measurement of the sample surface one wish to observe is then achieved by the raster-scan over the sample surface. The topography is determined as the time series of signal controlling the positioning device for realizing the constant tip-sample distance. This is the principle of the atomic force microscopy invented by Binnig [83] and now called *the contact mode* AFM. The microcantilever works as a force sensor to detect the tiny tip-sample interaction force.

The DFM, or the dynamic mode AFM, is one of the major and improved operating modes of AFM, in which the microcantilever is vibrated at its resonance frequency. Instead of the deflection detection, the shift of resonance frequency is detected in this mode, since the amount of the shift depend on the mean tip-sample distance. The DFM has two major operating modes called AM-DFM (DFM with Amplitude Modulation detection) [87] and FM-DFM (DFM with Frequency Modulation detection) [88], in which the variation of amplitude and frequency are detected respectively to estimate the shift of resonance frequency. The AM-DFM is mainly used in air and liquid and FM-DFM is operated in vacuum. The force sensitivity of the microcantilever as a sensor is much improved by increasing its quality factor. The adhesion to surface and resulting destruction of samples are also avoided by using the vibrating microcantilever. In both operating modes, variation of oscillation due to the shifted resonance frequency is measured using the optical lever method [72] in the standard device configuration. The height of the sample surface can be precisely adjusted by a positioning device, such as tube scanners.

7.2 Model of vibrating microcantilever under time-delayed feedback control

When the tip-sample interaction force is approximated by the Lennard-Jones potential, the first mode vibration of a microcantilever controlled by a scalar signal $u(t)$ is described by the following equation [79]:

$$\frac{\mathrm{d}}{\mathrm{d}t}\begin{bmatrix} x \\ y \end{bmatrix} = \begin{bmatrix} y \\ -x - \dfrac{d}{(\alpha + x)^2} + \dfrac{\Sigma^6 d}{30(\alpha + x)^8} + \varepsilon(\Gamma \cos \Omega t - \Delta y) \end{bmatrix} + \boldsymbol{b}u, \tag{7.1}$$

where x and y denote the displacement and the velocity of tip, respectively. $\boldsymbol{b}$ denotes a two dimensional constant vector concerning coupling between the control input and the state variables. α is the equilibrium position of tip when the gravity only acts on it. Γ and Ω correspond to the amplitude and frequency of the sinusoidal external force, which is provided to the microcantilever with the damping coefficient Δ, respectively. Σ denotes a constant related to the diameter of each molecule organizing the tip and the sample. It is noticed that Eq. (7.1) is dimensionless and $d = 4/27$ is a constant derived in the course of eliminating the dimension. A small parameter ε was prepared in Refs. [78, 79] to prove the existence of a chaotic invariant set through the Melnikov method on Eq. (7.1) under $u(t) = 0$. A chaotic oscillation of microcantilevers was subsequently presented numerically by Basso *et al.* based the same model. They showed a chaotic attractor arises following the cascade of period-doubling bifurcation [80]. It is noted that the magneto-elastic beam [14] and microcantilever under tip-sample interaction have a similar dynamical structure characterized by an elastic beam sinusoidally forced under two-well potential, although the dimension of the latter system is so much smaller.

We hereafter investigate controlled dynamics of a microcantilever in the AM-DFM. The microcantilever has the damping coefficient $\Delta = 0.4$ and is driven at fixed frequency $\Omega = 1.0$, namely, its dimensionless mechanical resonance frequency. The remaining parameters are set as $\Sigma = 0.3$ and $\varepsilon = 0.1$ based on the numerical result in Ref. [80]. Assuming that the velocity of oscillation is measured as an output of the nonlinear system (7.1), the control signal $u(t)$ is given as follows:

$$u(t) = K[y(t - \tau) - y(t)]. \tag{7.2}$$

This implementation of the control method is also obtained by putting $\boldsymbol{b} = [0\ \ 1]^T$, $g(x, y) = y$ into Eqs. (7.1) and (2.4). The time delay τ is adjusted to $2\pi/\Omega = 2\pi$ to stabilize an orbit with the same frequency as the external force oscillating the microcantilever. We note that the stabilization of this orbit is essential for the measurement by AM-DFM. This is because only this particular frequency

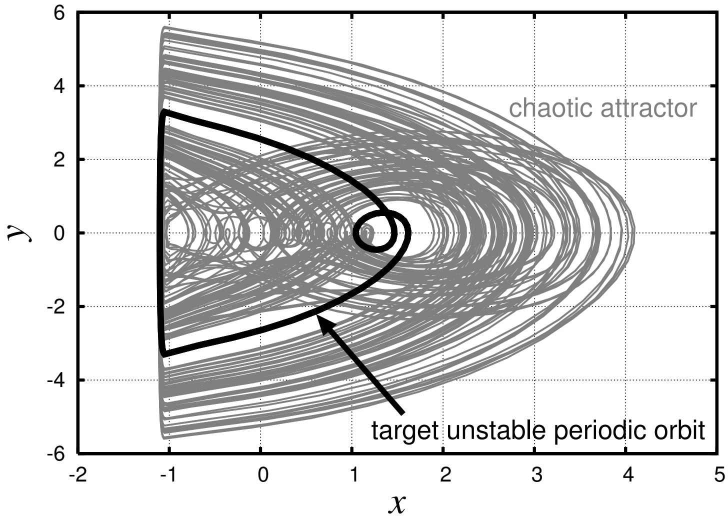

Figure 7.2: Chaotic attractor reported by Basso *et al.* [80] and target unstable periodic orbit embedded in it. The period of target orbit is 2π, which equals to the period of external force driving microcantilever sensor. The tip of microcantilever hits sample surface located $x = -\alpha = -1.2$ and then undergoes large repulsive force.

component is detected in the standard device configuration using such as lock-in amplifiers and RMS-DC (Root-Mean-Square to Direct Current) converters with band-pass filters. A wide spread frequency spectrum due to the subharmonic and chaotic oscillation modes possibly decreases the force sensitivity of AM-DFM, as long as the frequency component corresponding to the driving frequency is detected [139, 140]. Besides, non-periodic and irregular oscillation caused by chaos may also limit the resolution and operating range of the AM-DFM.

7.3 Extension of operating range

Recently, experimental studies by Jamitzky *et al.* have demonstrated a chaotic oscillation of microcantilever in an actual AM-DFM [81, 141], following the prediction by Ashhab *et al.* [78, 79] and Basso *et al.* [80]. In this section, we numerically show that the time-delayed feedback control has a possibility to eliminate the chaotic oscillation from microcantilever sensors based on Eq. (7.1).

Figure 7.2 shows a chaotic attractor reported by Basso *et al.* for $\alpha = 1.2$ and $\Gamma = 20$ [80] and an unstable periodic orbit embedded in it. The chaotic attractor and embedded unstable periodic orbit are shown by gray and black line, respectively. This unstable periodic orbit has the same period as the driving signal and therefore should be stabilized for operation of the AM-DFM detecting the harmonic component of microcantilever for measurement, as mentioned Sec. 7.2. The orbit is hereafter called *target orbit*. The target orbit is stabilized by adjusting the time delay τ to 2π as shown in Fig. 7.3. The chaotic oscillation of tip is converted to the target periodic one after the activation of control. The feedback gain is here adjusted to $K = 0.2$ and time of activation is pointed by an arrow in Fig. 7.3(b). One can confirm that the displacement of tip shown in Fig. 7.3(a) is changed from chaotic to a periodic motion, as control input shown in Fig. 7.3(b) converges to null signal after the activation. Note that the null control signal after the activation implies the chaotic oscillation is eliminated by stabilizing the target unstable period-2π orbit embedded in the chaotic attractor. The control inputs, therefore, change nothing but the stability with respect to the target orbit. No system parameters are modified in contrast to the feedback control proposed in Refs. [78, 79].

The time-delayed feedback control is thus able to extend the operating range of AM-DFM. This is confirmed by Fig. 7.4 showing two different toned parameter ranges, which are numerically characterized based on the stability of the target orbit. The black area displays a parameter range, where the target period-2π orbit is unstable if control is not applied. It has been reported that this black area is not appropriate for operation of the AM-DFM due to the possibility of period-doubling route to chaos [80]. On the other hand, in the gray area, the control method can keep the target period-2π orbit stable. Note that this gray area completely includes the black one, although a part of the gray area is hidden behind the superimposed black area. We therefore conclude that the possibility of period-doubling bifurcation and subsequent chaotic oscillation is eliminated by stabilizing the target

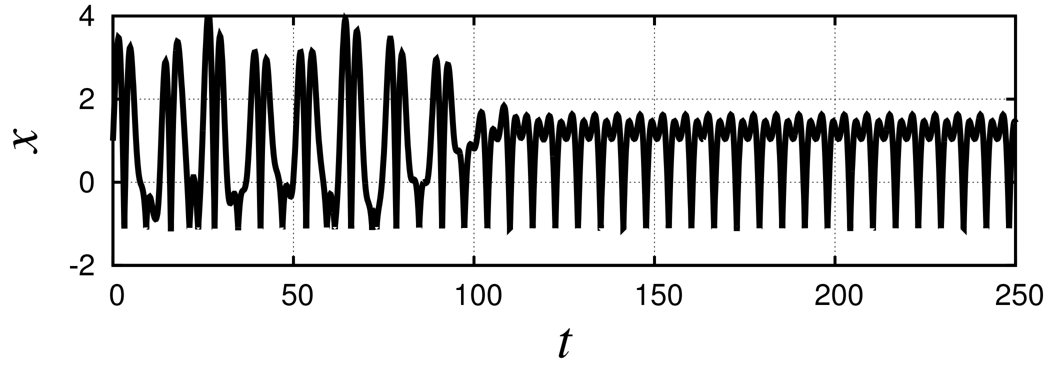

(a) displacement of microcantilever

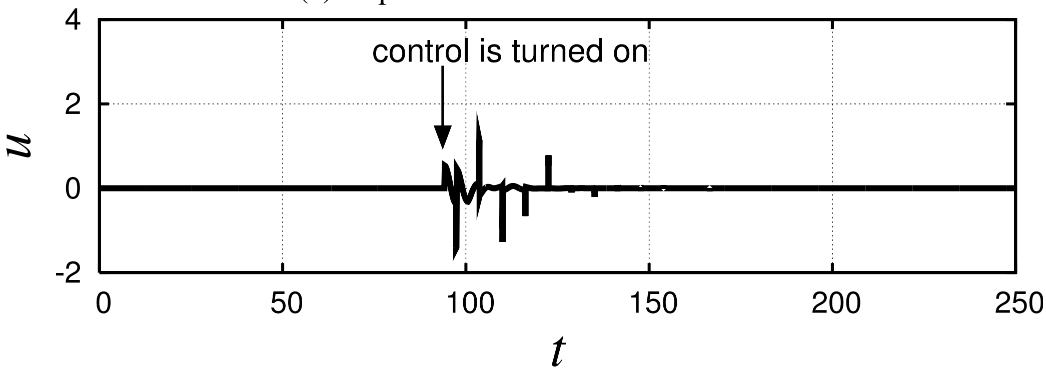

(b) control input

Figure 7.3: Stabilization of target unstable periodic orbit embedded in chaotic attractor using time-delayed feedback control. (a) and (b) show temporal change of displacement of microcantilever and control signal, respectively. Control is activated at the time pointed by arrow in (b). The motion of microcantilever is irregular and non-periodic before the activation. The control input finally converges to null after transient state, indicating that the activated control achieves convergence of motion to target periodic oscillation.

unstable periodic orbit. In other words, the operating range of AM-DFM is extended by applying the control method to microcantilever. It should be mentioned that this extended operating range is limited by white areas outside the gray one. The boundary between two regions shows the saddle-node bifurcation curve of the target orbit. However, another period-2π orbit can be kept stable in the white region, although the target orbit to which we have referred does not exist due to its annihilation by the saddle-node bifurcation. It is also noted that the stability of the target orbit is here numerically determined by spectral radius of the target orbit. The spectral radius is the modulus of the characteristic multiplier that has maximal modulus among all characteristic multipliers. The spectral radius is estimated using the Newton-Picard method [142] and subspace shooting method [143] for difference differential equations. The target orbit is stable, if the spectral radius is less than unity.

In this section, we have numerically shown that time-delayed feedback control can stabilize the unstable oscillation of microcantilevers. The stability analysis of target orbit has suggested the control method allows us to extend the operating range of AM-DFM. We should stress that control input changes only the characteristics multipliers of the target orbit and thereby oscillation in steady state are not modified regardless of control if the target orbit is stable in the uncontrolled system. This implies that time-delayed feedback control has no influence on the force sensitivity and measured quantities of the AM-DFM. Based on this property, the next section discusses improvement of transient response of microcantilever oscillation using the control method.

7.4 Improvement of transient response

Slow scanning rate is a significant weakness of the DFM and thus various efforts have been made to overcome this weakness [144–147]. As for the AM-DFM, the scanning rate is primarily limited by temporal length of the transient response of microcantilever and bandwidth of positioning device [146]. In this section, we

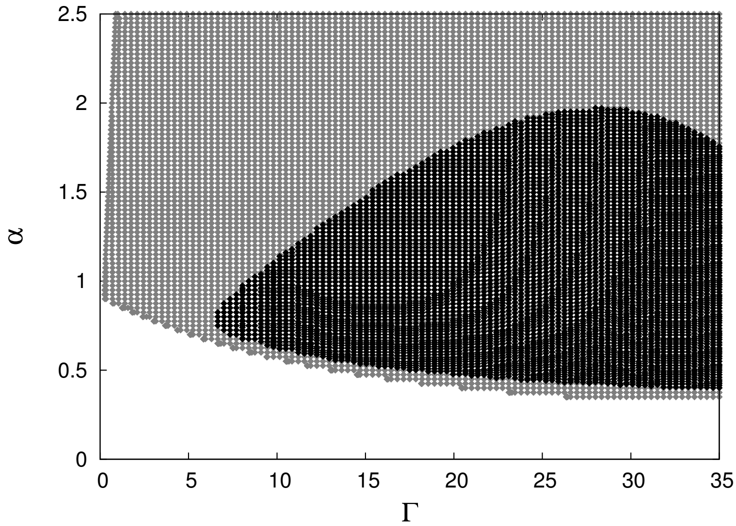

Figure 7.4: Operating range of DFM under time-delayed feedback control. Gray region shows parameter range where target orbit is kept stable under control. The region completely includes black area, in which operation of AM-DFM is not appropriate due to period-doubling route to chaotic oscillation reported in Ref. [80]. Notice that a part of the gray area is hidden by superimposed black region. The boundary between gray and white regions for small α (short tip-sample separation) or tiny Γ (small driving amplitude) shows saddle-node bifurcation curve of target orbit. Another stable periodic orbit can exist outside the gray region, but is not considered in this dissertation.

show the time-delayed feedback control has an ability to improve the transient response of microcantilever. The improved transient response allows us to accelerate the scanning rate of AM-DFM without reducing its force sensitivity.

The control input described by Eq. (7.2) explains the reason why the force sensitivity does not decrease under the time-delayed feedback control. The reason is that the control input can effectively reduce the quality factor of microcantilever just in transient state toward the target periodic oscillation. Since the control input (7.2) includes a term $-Ky(t)$ proportional to the velocity of tip, the control input serves as an apparent damping force applied to the microcantilever. On the other hand, the control input converges to null due to the effect of the term $Ky(t-\tau)$ denoting the past velocity, as the oscillation converges to the target periodic oscillation. The control input has, therefore, no influence on the steady oscillation governing the force sensitivity of the microcantilever at all, while the apparent damping force improves the transient response, depending on the feedback gain. In other words, the time-delayed feedback control allows us to overcome the trade-off between the transient response and force sensitivity. This is the essential difference from the active Q-controlled DFM, in which steady oscillation is changed by a feedback control [144, 146, 148].

Figure 7.5 compares the spectral radius of target orbit in a parameter plane related to amplitude of excitation and displacement of sample surface. The spectral radius without control and under the control with $K = 0.1$ is shown by a gray and black surface, respectively. The gray surface located below the black one illustrates that the transient response is improved under the time-delayed feedback control. The spectral radius under control is smaller than that without control in the whole parameter region we here investigate. Since smaller spectral radius implies faster convergence to the target orbit, Fig. 7.5 evidently shows the transient response is improved by applying the time-delayed feedback control.

We here estimate how much control contributes to the acceleration of scanning rate. The temporal length of transient response depends on the spectral radius and the initial variation of tip from the target orbit, if we assume the initial variation

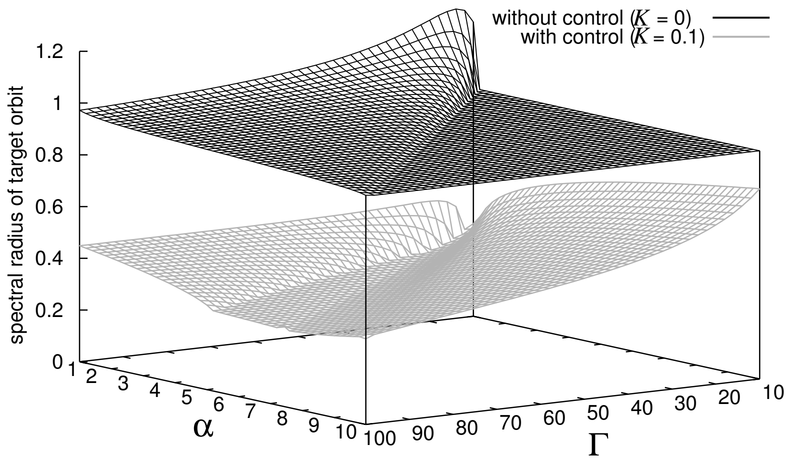

Figure 7.5: Comparison between spectral radius of controlled (gray surface) and uncontrolled (black surface) target orbit. Spectral radius under control with $K = 0.1$ is smaller than that under absence of control. Smaller spectral radius under control suggests that the time-delayed feedback control reduces temporal length of transient response of microcantilever oscillation and then allows us to increase scanning rate of AM-DFM.

is sufficiently small such that the dynamics of microcantilever is approximated by the linearized equation of Eq. (7.1). The motion of microcantilever close to the target oscillation is then described by the sum of dynamics in the direction of each invariant subspace [20, 21]. We additionally assume that the initial variation has only a component in the direction of the invariant subspace with respect to the characteristic multiplier that gives the spectral radius. The amplitude of variation decreasing in transient state is thereby estimated by the temporal change of a scalar variable:

$$|\xi(t)| = |\rho|^{\frac{t}{T}} |\xi(0)|, \tag{7.3}$$

where $\xi(t)$ denotes the amplitude of variation and $\xi(0)$ is the initial variation from the target orbit. The $|\rho|$ is the spectral radius of the target orbit and $T = 2\pi/\Omega$ denotes the period of sinusoidal external force. Note that $\xi(t)$ shows attenuation in the direction of the particular invariant subspace. Although the temporal length of transient response is also related to the remaining invariant subspaces and even global structures of phase space [128], the estimation by Eq. (7.3) insures the upper limit of the acceleration. The characteristic multiplier giving the spectral radius primarily determines the length of transient response. It is also noted that the variation itself is oscillatory if the ρ has nonzero imaginary part. Nevertheless, the decay of its envelope is estimated by $\xi(t)$.

We define the settling time $T_s(K)$ as the elapsed time before the amplitude of variation reaches at $\varepsilon_{th}|\xi(0)|$, where $\varepsilon_{th} > 0$ is small threshold and K the feedback gain. The settling time is then obtained from Eq. (7.3) as follows:

$$T_s(K) = T \frac{\log \varepsilon_{th}}{\log |\rho(K)|}. \tag{7.4}$$

We can thus estimate the ratio of the settling time without control to that with control. The ratio of the settling time is important because it gives the upper limit for acceleration of scanning rate under control input. Equation (7.4) implies that the ratio is given by

$$\frac{T_s(0)}{T_s(K)} = \frac{\log |\rho(K)|}{\log |\rho(0)|}, \tag{7.5}$$

depending on neither the initial variation nor the threshold. Figure 7.6 shows the ratio of settling time numerically estimated for $K = 0.1$. The parameter region here examined is the same as in Fig. 7.5. It is recognized that the ratio, continuously toned in Fig. 7.6, ranges from a few to twenty. This implies the scanning rate can be a few to twenty times faster in the controlled case than in the uncontrolled one. The ratio, or upper limit, is significantly increased due to settling time $T_s(K)$ reduced by control input. It is noted that the ratio is here defined as positive infinity, because $T_s(0) = \infty$ if the uncontrolled target orbit is unstable. The trajectory without control does not converge to the unstable target orbit forever.

In this section, we have discussed improved transient response of the microcantilever under the time-delayed feedback control. The resulting improved transient response enables us to accelerate scanning rate of the AM-DFM without reducing force sensitivity. The analysis on the spectral radius shows a few to twenty times faster scanning rate can be achieved using the time-delayed feedback control.

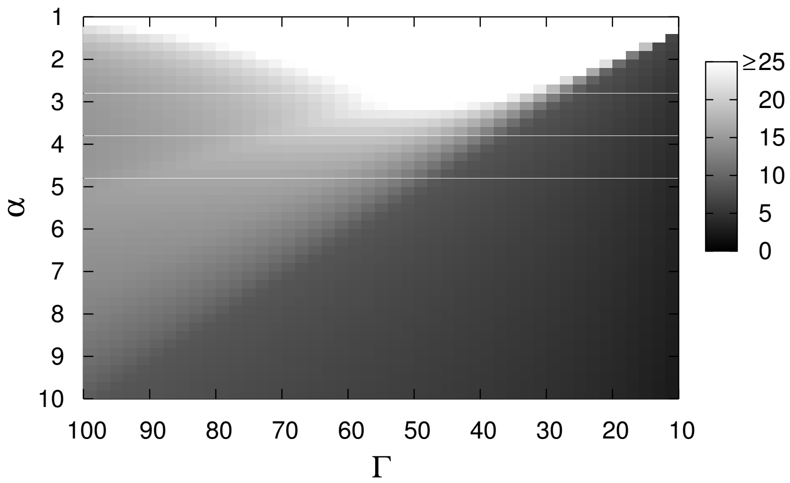

Figure 7.6: Ratio of temporal length of transient response without control to that with control. The ratio (continuously toned in the figure) is numerically determined for $K = 0.1$ based on Eq. (7.5) in the same parameter region as Fig. 7.5. The ratio estimates upper limit for acceleration of scanning rate under time-delayed feedback control. A few to twenty times faster scanning rate can be achieved compared to uncontrolled case. This is due to reduced temporal length of transient response under control. Each axis has the same direction as that in Fig. 7.5.

7.5 Stabilization in grazing region

Another route to chaos in the AM-DFM has been recently demonstrated by Hu and Raman [82]. They suggested the chaotic oscillation is caused by grazing bifurcation, which occurs when the cantilever tip just begins to hit a surface. The grazing bifurcation in the AM-DFM was predicted by van de Water and Molenaar [149]. This section is devoted to show that the time-delayed feedback control works also in a grazing region. The parameter setup for numerical simulation is listed in Table 7.1, from which the dimensionless parameters in Eq. (7.1) are obtained as $\Omega = 0.98$, $\Gamma = 10.0$, and $\Sigma = 0.3$.

When the cantilever approaches the surface, a chaotic oscillation is generated. A corresponding bifurcation diagram is shown in Fig. 7.7, which is obtained by monotonously decreasing the tip-sample distance from $\alpha = 27\,\mathrm{nm}$ to $\alpha = 7\,\mathrm{nm}$.

The vertical axis shows displacement sampled at the same phase for each period of driving force. One can see that the periodic oscillation is bifurcated to chaotic oscillation and periodic oscillations including subharmonic components. The stability of the target orbit and obtained various steady states is given in Fig. 7.8. Figure 7.9 shows a chaotic attractor for $\alpha = 20\,\mathrm{nm}$ and an unstable periodic orbit embedded in it. The chaotic attractor and embedded unstable periodic orbit are shown by gray and black lines, respectively. We should stabilize the orbit for the operation of AM-DFM. The target orbit is stabilized when we adjust the time delay τ to $1/f$ and feedback gain to $K = 0.075$ as shown in Fig. 7.10. The chaotic oscillation of tip is changed to the target periodic one after the activation of control. The time of activation is pointed by an arrow in Fig. 7.10(b). We confirm that the displacement of tip in Fig. 7.10(a) is changed from chaotic to a periodic oscillation. Corresponding to this change, control input in Fig. 7.10(b) converges to null signal after the activation. This null signal implies that the chaotic oscillation is eliminated by stabilizing the target unstable periodic orbit embedded in the chaotic attractor. Figure 7.11 shows the bifurcation diagram for $K = 0.1$. We can see the control input only allows the target periodic oscillation in the whole range we investigate. This implies that the AM-DFM can be stably operated in the grazing regime using the time delayed feedback control. We close this section by summarizing the parameter region where the control is possible in Fig. 7.12.

Table 7.1: Parameter setup of numerical simulation for grazing route. Dimensionless parameters of cantilever model are obtained as $\Omega = 0.98$, $\Gamma = 10.0$, $\Sigma = 0.3$ from this table.

name of parameter	notation	value
resonance frequency	f_0	50 kHz
stiffness	k	1.1 N/m
quality factor	Q	100
tip radius	R	20 nm
diameter of molecule	σ	0.3 nm
Hamaker constant(att.)	A_2	1.0×10^{-19} J
driving frequency	f	49 kHz
amplitude of free oscillation	b_0	25 nm

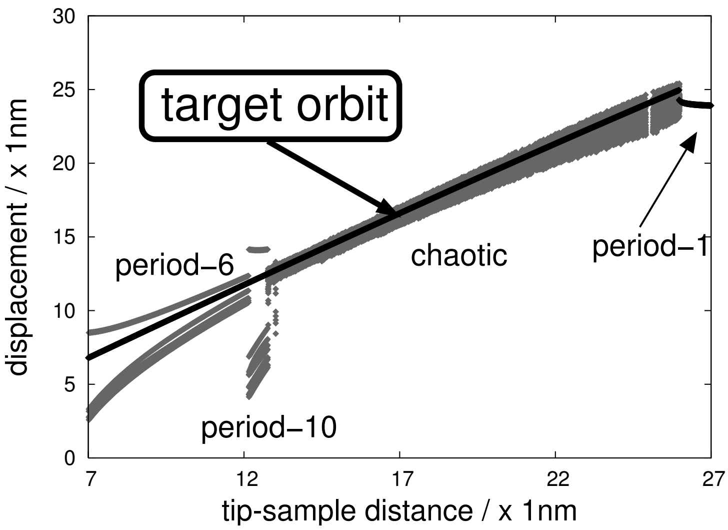

Figure 7.7: Bifurcation diagram of uncontrolled cantilever oscillation in grazing region. Horizontal axis corresponds to tip-sample distance monotonous decreased from 27 nm to 7 nm. Vertical axis denotes displacement sampled at the same phase for each period of driving force. We can see periodic oscillations including subharmonic components and chaotic oscillation.

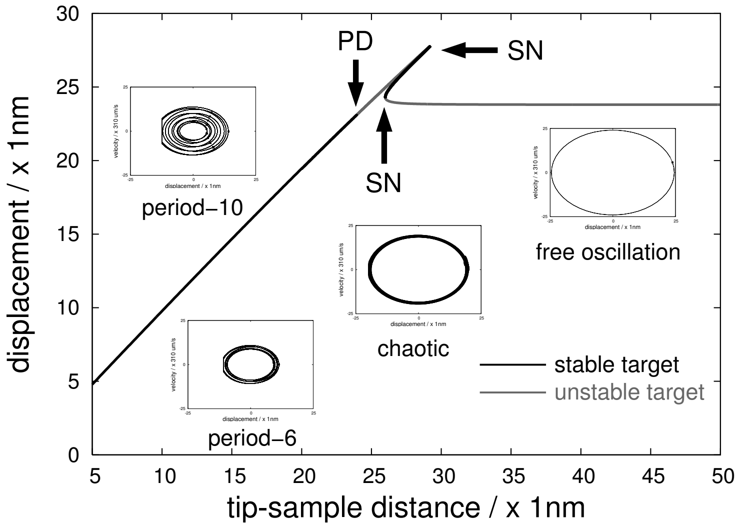

Figure 7.8: Stability of target orbit and various oscillation arising in steady states without control.

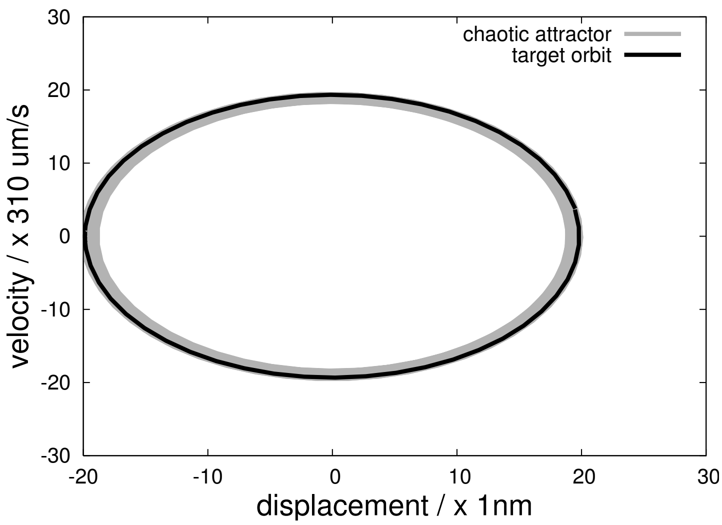

Figure 7.9: Chaotic attractor and target unstable periodic orbit embedded in it. The period of target orbit is $1/f$, which equals to the period of external force driving cantilever sensor. The tip of cantilever hits sample surface located $x = -\alpha = -20\,\text{nm}$ and then undergoes large repulsive force.

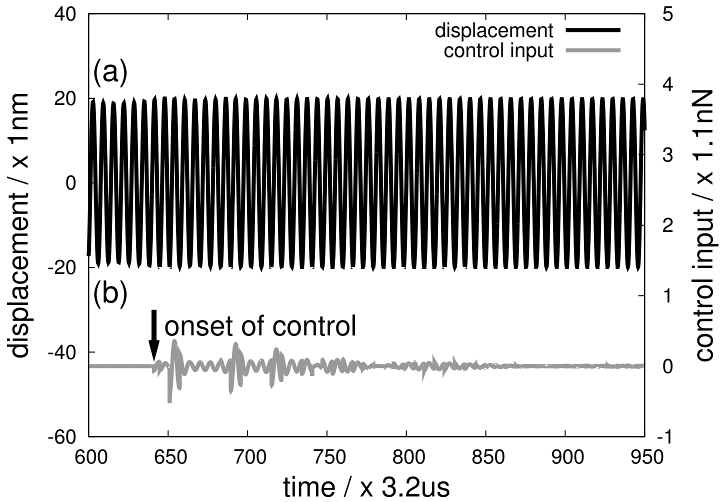

Figure 7.10: Stabilization of target unstable periodic orbit using time-delayed feedback control. (a) and (b) show temporal change of displacement of cantilever and control signal, respectively. Control is activated at the time pointed by arrow in (b). The motion of cantilever is irregular and non-periodic before the activation. The control input finally converges to null after transient. This implies that the activated control achieves stabilization of target periodic oscillation.

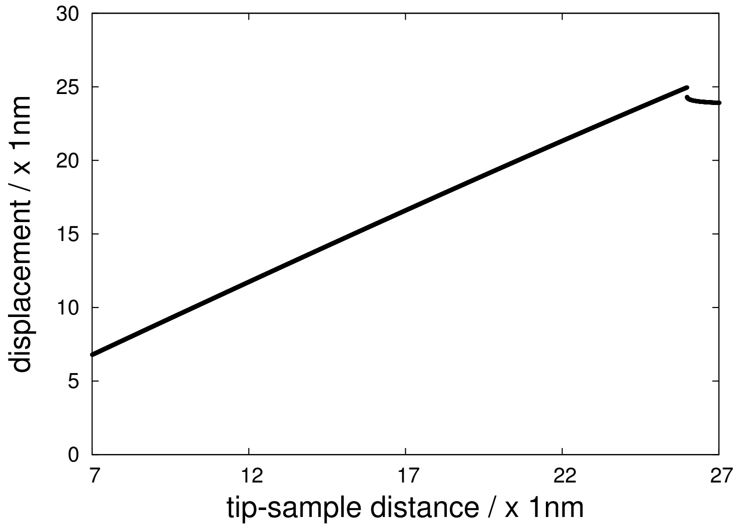

Figure 7.11: Bifurcation diagram of controlled cantilever oscillation in grazing region. Only the target orbits is allowed and oscillation including subharmonic components are suppressed in the whole tip-sample distance under investigation.

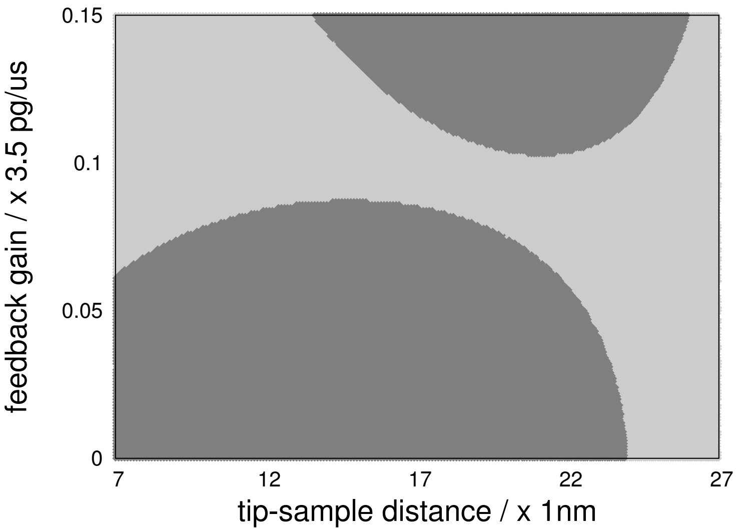

Figure 7.12: Domain of control in grazing region. The target orbit is stable and unstable in light gray region and dark gray one, respectively.

7.6 Concluding remarks

In this chapter, we numerically discussed the stabilization of microcantilever sensors in the AM-DFM using time-delayed feedback control. The operating range of AM-DFM is extended by stabilizing the unstable periodic orbit embedded in the chaotic attractor. It implies that the intrinsic dynamics behind the instable motion including chaos can be utilized for the AM-DFM measurement by applying the time-delayed feedback control. Transient response in AM-DFM is also improved by the control method. We can therefore overcome the trade-off relationship between scanning rate and force sensitivity in the AM-DFM. It is pointed out that control eliminating the irregular oscillation can help manipulation of surface, since the manipulation seems to need strong tip-sample interaction that is obtained in the operation near sample surfaces [81]. In addition, we treated grazing bifurcation of tip oscillation. Generation of subharmonics and chaos in transition from non-contact to contact regime was predicted numerically by van de Water and Molenaar [149] and then suggested experimentally by Hu and Raman [82]. We showed the time-delayed feedback control also stabilize a microcantilever grazing against the sample surface. The subharmonic and chaos are successfully suppressed in the whole range we investigated.

Chapter 8

Conclusion and future directions

The dissertation began with posing the fundamental questions lying on the controlling chaos using time-delayed feedback. The essential importance of the global dynamics in controlling chaos is due to the possibility of the coexistence of global chaotic dynamics and locally stabilized target orbits in controlled systems. The problem simultaneously shed light on the existence of the missing-link between the preceding successful experimental results and theoretical explanation based on the stability analysis of target orbits. The global dynamics of the two-well Duffing system under the time-delayed feedback control was then numerically investigated in this study and the results were generalized to periodic systems under control. The scope and method going beyond those of the conventional stability analysis now enable us to answer the questions and thus provide the new and general insights on the ability and characteristics of the time-delayed feedback control of chaos especially in engineering systems. In addition, the novel application of the control method to DFM was proposed. The possibility of the application numerically confirmed in this study becomes a milestone toward the application of nonlinear dynamics and chaos to nanoengineering systems. The accomplishment and future direction of this study are summarized below.

In Chapter 3, different steady states emerging in the controlled two-well Duffing system were found out and analyzed by applying the bifurcation theory to the difference differential equations describing the controlled systems. It was emphasized that the onset timing of control is an important control parameter determining the success of control. The influence of unstable coexisting orbits on the transient dynamics was also pointed out. The mechanism yielding the multiple steady states was given as the stabilization of the non-target unstable periodic orbits originally embedded in the chaotic attractor. Period-doubling bifurcation and saddle-node bifurcation explained their stability loss and annihilation, respectively.

The multiple steady states found out in the controlled systems motivated us to investigate the domain of attraction for target orbits in function space. In Chapter 4, the dependence of steady states on initial conditions was discussed in detail based on the results in Chapter 3. The boundary structures of the domain of attraction in function space were especially elucidated. The self-similar boundary structure generated by control explained the sensitive dependence on initial conditions and suggested the existence of the chaotic dynamics behind the stabilized target orbits. It was shown that one may encounter the highly complicated boundary structure when attempting the selective stabilization of the two target orbits with the same period. This immediately implied that the stability of the target orbits in the sense of local or linearized dynamics never gives the full explanation of the ability of the time-delayed feedback control experimentally demonstrated so far.

Chapter 5 directly probed the global phase structures in the infinite dimensional phase space by revealing the one-dimensional unstable manifold persistently existing in the controlled system. The unstable manifold and associated global phase structure were shown in various amplitudes of feedback gain. The original chaotic dynamics is destroyed and then completely simple global structure is realized together with stable target orbits, as the feedback gain is increased. The rapid convergence to target orbits is achieved under this simplified global phase structure. On the other hand, persistence of the original chaotic dynamics under control arose as was expected in Chapter 1. The persistence of chaotic dynamics was proved to be a fundamental problem in controlling chaos and provided the full explanation of mechanism that causes transient chaos and highly complicated boundary structures observed in Chapter 4. It is noted that the explanation is never given by the linearizion based approaches.

In Chapter 6, the results in Chapter 3 and Chapter 5 were generalized as the features of the global dynamics in a periodic system under control. The revisit to the results in the previous chapters gave a clue to generalization. It was suggested that the problem of the global change from the original chaos producing to the simplified structure was reduced to that of the annihilation and degeneration of the non-target unstable periodic orbits from the controlled systems. The annihilation and degeneration of the non-target orbits were then generalized to a periodic system under control incorporating the harmonic balance method. A typical scenario of the change of global structure for increase of feedback gain was characterized and then a promising explanation was given to ability and performance of the time-delayed feedback control experimentally demonstrated so far.

Chapter 7 presented a novel and important application of the control method to chaos in the AM-DFM. We numerically demonstrated the ability of the control method as the first step toward the real implementation. It was shown that the two different chaotic oscillations of microcantilever recently reported can be stabilized by the time-delayed feedback control. The control method is able to extend the operating range of the AM-DFMs. The trade-off relationship between the force sensitivity and scanning speed can be overcome under the control method. The control method enables us to improve transient response of the microcantilever without modifying its parameters.

This study is devoted to the global aspects of time-delayed feedback control and its application to the nanoengineering systems. The future directions are mentioned as follows. One direction is classification of dynamical systems by controllability with time-delayed feedback control. In Chapter 6, we provided a theoretical framework to discuss the performance of control from the viewpoint of the global dynamics of controlled systems. The presented result covers only the periodic systems and several assumptions were made to prove the annihilation and degeneration of the target orbits. The further generalization has to be given, because important targets of the time-delayed feedback control are excluded in the present setup. Autonomous systems are one of the most important classes, but the present framework does not work since the period of non-target orbits is varied as the feedback gain is increased. The model of microcantilever in the DFM is also out of the scope now. The uniform ultimate boundedness is the most important assumption; however, the model does not seem to satisfy this assumption and therefore we have to investigate what enabled us to stabilize a target orbit without care to global dynamics in Chapter 7. Justification of the framework is also not completed in this dissertation. The justification of the describing function method given from the 1970s to the 1980s [137, 138] will give us a clue to the justification of the present framework. It is also interesting to clarify the mechanism causing the global chaotic dynamics and its simplification in infinite dimension more precisely. The proof of the existence of the homoclinic intersection and how the intersection is simplified in function space are proposed as a challenging problem for the dynamical system theory.

Another direction is experimental demonstration of control of microcantilever oscillations. In this dissertation, the possibility of the application to the DFM was numerically proved under the ideal conditions on the actuators and sensors for microcantilevers. The next step is implementation of controller to an actual device. The circuit implement of the control method is not a problem if we attempt to stabilize a microcantilever with resonance around 10 to 100 kHz. In this range, the digital facility can be effectively used for making a flexible controller to examine the control performance and resulting improved measurement performance experimentally. On the other hand, there are many factors seriously limiting the control performance in reality and this is emphasized especially in micro and nanosystems. Characteristics of actuator for microcantilever is the most critical in the current standard device configuration of the DFM. One can observe many spurious peaks if one actuates the microcantilever with a standard piezoelectric actuator. This implies that the presence of large phase delay in the feedback loop and therefore one has to at least apply the control method in a limited frequency bandwidth in practice. However, the problem of the bandwidth required for the control method has not been studied so far. We have to investigate the control performance under serious restriction to implementation. This is a practical problem related to the experimental setup, but also opens a new future of theoretical studies on the control method.

Bibliography

[1] Y. Ueda, The Road to Chaos-II, (Aerial Press, Inc., 2001).

[2] F. C. Moon and P. J. Holmes, Strange attractors and chaos in nonlinear mechanics, J. Appl. Mech. -T ASME, **50** (4B), 1021–1032 (1983).

[3] P. Bergé, Y. Pomeau, and C. Vidal, Order Within Chaos: Towards a Deterministic Approach to Turbulence, (John Wiley & Sons, Inc., 1984).

[4] J. M. T. Thompson and H. B. Stewart, Nonlinear Dynamics and Chaos, 1st Ed., (John Wiley & Sons, Ltd., 1986).

[5] F. C. Moon, Chaotic Vibrations, (John Wiley & Sons, Inc., 1987).

[6] C. Grebogi and J. A. Yorke (editors), The Impact of Chaos on Science and Society, (The United Nations University Press, 1997).

[7] R. Abraham and Y. Ueda (editors), The Chaos Avant-Garde : Memories of the Early Days of Chaos Theory, (World Scientific, 2000).

[8] E. Ott, Chaos in Dynamical Systems, 2nd Ed., (Cambridge University Press, 1993).

[9] C. Hayashi, Y. Ueda, N. Akamatsu, and H. Itakura, On the behavior of self-oscillatory systems with external force, Trans. IECE, **53-A** (3), 150–158 (1970).

[10] E. N. Lorenz, Deterministic nonperiodic flow, J. Atmos. Sci., **20** (2), 130–141 (1963).

[11] R. M. May, Biological populations with nonoverlapping generations: stable points, stable cycles, and chaos, Science, **186** (4164), 645–647 (1974).

[12] O. E. Rössler, An equation for continuous chaos, Phys. Lett, **57A** (5), 397–398 (1976).

[13] M. C. Mackey and L. Glass, Oscillation and chaos in physiological control systems, Science, **197**, 287–289 (1977).

[14] F. C. Moon and P. J. Holmes, A magnetoelastic strange attractor, J. Sound. Vib., **65** (2), 275–296 (1979).

[15] K. Ikeda, Multiple-valued stationary state and its instability of the transmitted light by a ring cavity system, Opt. Commun., **30** (2), 257–262 (1979).

[16] B. A. Huberman, J. P. Crutchfield, and N. H. Packard, Noise phenomena in Josephson junctions, Appl. Phys. Lett., **37** (8), 750–752 (1980).

[17] P. S. Linsay, Period doubling and chaotic behavior in a driven anharmonic oscillator, Phys. Rev. Lett., **47** (19), 1349–1352 (1981).

[18] M. Kitano, T. Yabuzaki, and T. Ogawa, Chaos and period-doubling bifurcation in a simple acoustic system, Phys. Rev. Lett., **50** (10), 713–716 (1983).

[19] F. M. A. Salam and S. S. Sastry, Dynamics of the forced Josephson junction circuit: the regions of chaos, IEEE T. Circuits. Syst., **32** (8), 784–796 (1985).

[20] J. Guckenheimer and P. J. Holmes, Nonlinear Oscillations, Dynamical Systems and Bifurcations of Vector Fields, (Springer-Verlag New York Inc., 1983).

[21] S. Wiggins, Introduction to Applied Nonlinear Dynamical Systems and Chaos, (Springer-Verlag New York Inc., 1990).

[22] E. Ott, C. Grebogi, and J. A. Yorke, Controlling chaos, Phys. Rev. Lett., **64** (11), 1196–1199 (1990).

[23] L. M. Pecora and T. L. Carroll, Synchronization in chaotic systems, Phys. Rev. Lett., **64** (8), 821–824 (1990).

[24] K. M. Cuomo and A. V. Oppenheim, Circuit implementation of synchronized chaos with application to communications, Phys. Rev. Lett., **71** (1), 65–68 (1993).

[25] T. Shinbrot, C. Grebogi, E. Ott, and J. A. Yorke, Using small perturbation to control chaos, Nature, **363** (6428), 411–417 (1993).

[26] H. G. Schuster (editor), Handbook of Chaos Control, (Wiley-VCh, 1999).

[27] T. Kapitaniak, Controlling Chaos: Theoretical and Practical Methods in Non-linear Dynamics, (Academic Press, 1996).

[28] W. L. Ditto, S. N. Rauseo, and M. L. Spano, Experimental control of chaos, Phys. Rev. Lett., **65** (26), 3211–3214 (1990).

[29] J. Singer, Y.-Z. Wang, and H. H. Bau, Controlling a chaotic system, Phys. Rev. Lett., **66** (9), 1123–1125 (1991).

[30] E. R. Hunt, Stabilizing high-period orbits in a chaotic system: The diode resonator, Phys. Rev. Lett., **67** (15), 1953–1955 (1991).

[31] B. Peng, V. Petrov, and K. Showalter, Controlling chemical chaos, J. Phys. Chem., **95** (13), 49570–4959 (1991).

[32] A. Garfinkel, M. L. Spano, W. L. Ditto, and J. N. Weiss, Controlling cardiac chaos, Science, **257** (5074), 1230–1235 (1992).

[33] A. Azevedo and S. M. Rezende, Controlling chaos in spin-wave instabilities, Phys. Rev. Lett., **66** (10), 1342–1345 (1991).

[34] K. Pyragas, Continuous control of chaos by self-controlling feedback, Phys. Lett. A, **170** (6), 421–428 (1992).

[35] K. Myneni, T. A. Barr, N. J. Corron, and S. D. Pethel, New method for the control of fast chaotic oscillations, Phys. Rev. Lett., **83** (11), 2175–2178 (1999).

[36] T. Ushio, Controlling chaos (in Japanese), (Asakura Publishing Co., Ltd., 1996).

[37] W. Just, H. Benner, and E. Reibold, Theoretical and experimental aspects of chaos control by time-delayed feedback, Chaos, **13** (1), 259–266 (2003).

[38] K. Pyragas, Delayed feedback control of chaos, Philos. T. R. Soc. A, **364** (1846), 2309–2334 (2006).

[39] N. Minorsky, Self-excited mechanical oscillations, J. Appl. Phys., **19**, 332–338 (1948).

[40] K. Watanabe, Control of time delay systems (in Japanese), (Society of Instrument and Control Engineers, 1993).

[41] S. H. Strogatz, Nonlinear dynamics - death by delay, Nature, **394** (6691), 316–317 (1998).

[42] K. Hirata, Does ”dead” mean ”useless”? (in Japanese), Journal of the ISCIE, Systems, Control and Information, **45** (9), 544–545 (2001).

[43] S.-I. Niculescu, Delay Effects on Stability — A Robust Control Approach —, Lecture Notes in Control and Information Sciences, (Splinger-Verlag London Limited, 2001).

[44] S. Yamamoto, Delayed feedback control —controlling chaos utilizing time-delay— (in Japanese), Journal of the ISCIE, Systems, Control and Information, **46** (7), 377–384 (2002).

[45] Y. Ueda and Y. Inoue, Forced oscillations in a nonlinear system with time delay (in Japanese), The Transaction of the IEEJ, **95** (B6), 239–246 (1975).

[46] Y. Ueda and H. Ohta, Bifurcations in a system described by a nonlinear differential equation with delay, Chaos, **4** (1), 75–83 (1994).

[47] F. C. Moon (editor), Dynamics and chaos in manufacturing processes, (John & Sons, Inc., 1998).

[48] K. Pyragas and A. Tamaševičius, Experimental control of chaos by delayed self-controlling feedback, Phys. Lett. A, **180** (1–2), 99–102 (1993).

[49] J. E. S. Socolar, D. W. Sukow, and D. J. Gauthier, Stabilizing unstable periodic orbits in fast dynamical systems, Phys. Rev. E, **50** (4), 3245–3248 (1994).

[50] S. Bielawski, D. Derozier, and P. Glorieux, Controlling unstable periodic orbits by a delayed continuous feedback, Phys. Rev. E, **49** (2), R971–R974 (1994).

[51] T. Pierre, G. Bonhomme, and A. Atipo, Controlling the chaotic regime of nonlinear ionization waves using the time-delay autosynchronization method, Phys. Rev. Lett, **76** (13), 2290–2293 (1996).

[52] T. Hikihara and T. Kawagoshi, An experimental study on stabilization of unstable periodic motion in magneto-elastic chaos, Phys. Lett. A, **211** (1), 29–36 (1996).

[53] P. Parmananda, R. Madrigal, M. Rivera, L. Nyikos, I. Z. Kiss, and V. Gáspár, Stabilization of unstable steady states and periodic orbits in an

electrochemical system using delayed-feedback control, Phys. Rev. E, **59** (5), 5266–5271 (1999).

[54] A. Guderian, A. F. Münster, M. Kraus, and F. W. Schneider, Electrochemical chaos control in a chemical reaction: experiment and simulation, J. Phys. Chem. A, **102** (26), 5059–5064 (1998).

[55] E. Gravier, X. Caron, G. Bonhomme, T. Pierre, and J. L. Briancon, Dynamical study and control of drift waves in a magnetized laboratory plasma, Eur. J. Phys. D, **8** (3), 451–457 (2000).

[56] T. Fukuyama, H. Shirahama, and Y. Kawai, Dynamical control of the chaotic state of the current-driven ion acoustic instability in a laboratory plasma using delayed feedback, Phys. Plasmas, **9** (11), 4525–4529 (2002).

[57] O. Lüthje, S. Wolff, and G. Pfister, Control of chaotic Taylor-Couette flow with time-delayed feedback, Phys. Rev. Lett., **86** (9), 1745–1748 (2001).

[58] K. Pyragas, Control of chaos via extended delay feedback, Phys. Lett. A, **206** (5–6), 323–330 (1995).

[59] H. Nakajima, On analytical property of delayed feedback control of chaos, Phys. Lett. A, **232** (3–4), 207–210 (1997).

[60] H. Nakajima and Y. Ueda, Limitation of generalized delayed feedback control, Physica D, **111** (1–4), 143–150 (1998).

[61] W. Just, T. Bernard, M. Ostheimer, E. Reibold, and H. Benner, Mechanism of time-delayed feedback control, Phys. Rev. Lett., **78** (2), 203–206 (1997).

[62] W. Just, D. Reckwerth, E. Reibold, and H. Benner, Influence of control loop latency on time-delayed feedback control, Phys. Rev. E, **59** (3), 2826–2829 (1999).

[63] W. Just, E. Reibold, K. Kacperski, P. Fronczak, J. A. Holyst, and H. Benner, Influence of stable Floquet exponents on time-delayed feedback control, Phys. Rev. E, **61** (5), 5045–5056 (2000).

[64] K. Pyragas, Control of chaos via an unstable delayed feedback controller, Phys. Rev. Lett., **86** (11), 2265–2268 (2001).

[65] P. Hövel and J. E. S. Socolar, Stability domain of time-delay feedback control with latency, Phys. Rev. E, **68** (3), 036206 (2003).

[66] T. Ushio, Limitation of delayed feedback control in nonlinear discrete-time systems, IEEE T. Circuits-I, **43** (9), 815–816 (1996).

[67] H. Nakajima, H. Ito, and Y. Ueda, Automatic adjustment of delay time and feedback gain in delayed feedback control of chaos, IEICE T. Fund. Electr., **E80** (9), 1554–1559 (1997).

[68] T. Hikihara and Y. Ueda, An expansion of system with time delayed feedback control into spatio-temporal state space, Chaos, **9** (4), 887–892 (1999).

[69] W. Just, H. Benner, and C. v Löwenich, On global properties of time-delayed feedback control: weakly nonlinear analysis, Physica D, **199** (1–2), 33–44 (2004).

[70] J. K. Hale, Theory of Functional Differential Equations, (Springer-Verlag New York, Inc., 1977).

[71] J. K. Hale and S. M. V. Lunel, Introduction to Functional Differential Equations, (Springer-Verlag New York, Inc., 1993).

[72] G. Meyer and M. Amer, Novel optical approach to atomic force microscopy, Appl. Phys. Lett., **53** (12), 1045–1047 (1988).

[73] R. P. Feynman, There's plenty of room at the bottom, Engineering and Science, **23**, 22–36 (1960).

[74] S. Morita (editor), Nanomechanics of atoms and molecules (in Japanese), (Maruzen Co., Ltd., 2003).

[75] Y. C. Wang, S. G. Adams, J. S. Thorp, N. C. MacDonald, P. Hartwell, and F. Bertsch, Chaos in MEMS, parameter estimation and its potential application, IEEE T. Circuits-I, **45** (10), 1013–1020 (1998).

[76] C. Gui, R. Legtenberg, H. A. C. Tilmans, J. H. J. Fluitman, and M. Elwenspoek, Nonlinearity and hysteresis of resonant strain gauges, J. Microelectromech. S., **7** (1), 122–127 (1998).

[77] S. K. De and N. R. Aluru, Complex oscillations and chaos in electrostatic microelectromechanical systems under superharmonic excitations, Phys. Rev. Lett., **94** (20), 204101 (2005).

[78] M. Ashhab, M. V. Salapaka, M. Dahleh, and I. Mezić, Dynamical analysis and control of microcantilevers, Automatica, **35** (10), 1663–1670 (1999).

[79] M. Ashhab, M. V. Salapaka, M. Dahleh, and I. Mezić, Melnikov-based dynamical analysis of microcantilevers in scanning probe microscopy, Nonlinear Dynam., **20** (3), 197–220 (1999).

[80] M. Basso, L. Giarre, M. Dahleh, and I. Mezić, Complex dynamics in a harmonically excited Lennard-Jones oscillator: microcantilever-sample interaction in scanning probe microscopes, J. Dyn. Syst.-T. ASME, **122** (1), 240–245 (2000).

[81] F. Jamitzky, M. Stark, W. Bunk, W. M. Heckl, and R. W. Stark, Chaos in dynamic atomic force microscopy, Nanotechnology, **17** (7), S213–S220 (2006).

[82] S. Hu and A. Raman, Chaos in atomic force microscopy, Phys. Rev. Lett., **96** (3), 036107 (2006).

[83] G. Binnig, C. F. Quate, and C. Gerber, Atomic force microscope, Phys. Rev. Lett., **56** (9), 930–933 (1986).

[84] G. Binning, H. Rohrer, C. Gerber, and E. Weibel, Surface studies by scanning tunneling microscopy, Phys. Rev. Lett., **49** (57), 57–61 (1982).

[85] F. J. Giessibl, Advances in atomic force microscopy, Rev. Mod. Phys., **75** (112), 949–983 (2003).

[86] R. García and R. Pérez, Dynamic atomic force microscopy methods, Surf. Sci. Rep., **47** (6–8), 197–301 (2002).

[87] Y. Martin, C. C. Williams, and H. K. Wickramasinghe, Atomic force microscope-force mapping and profiling on a sub 100-Å scale, J. Appl. Phys., **61** (4), 4723–4729 (1987).

[88] T. R. Albrecht, P. Grütter, D. Horne, and D. Rugar, Frequency modulation detection using high-Q cantilevers for enhanced force microscope sensitivity, J. Appl. Phys., **69**, 668–673 (1991).

[89] F. J. Giessibl, Atomic resolution of the silicon (111)-(7×7) surface by atomic force microscopy, Science, **267** (5194), 68–71 (1995).

[90] Y. Sugawara, M. Ohta, H. Ueyama, and S. Morita, Defect motion on an InP(110) surface observed with noncontact atomic force microscopy, Science, **270** (5242), 1646–1648 (1995).

[91] S. Kitamura and M. Iwatsuki, Observation of 7×7 reconstructed structure on the silicon (111) surface using ultrahigh vacuum noncontact atomic force microscopy, Jpn. J. Appl. Phys. 2., **34** (1B), L145–L148 (1995).

[92] T. Fukuma, Applications of dynamic force microscopy to molecular-scale investigations on organic ultrathin films, Ph.D thesis, (Kyoto University, 2003).

[93] P. K. Hansma, J. P. Cleveland, M. Radmacher, D. A. Walters, P. E. Hillner, M. Bezanilla, M. Fritz, D. Vie, H. G. Hansma, C. B. Prater, J. Massie, L. Fukunaga, J. Gurley, and V. Elings, Tapping mode atomic force microscopy in liquids, Appl. Phys. Lett., **64** (13), 1738–1740 (1994).

[94] Constant A. J. Putman, Kees O. Van der Werf, Bart G. De Grooth, Niek F. Van Hulst, and Jan Greve, Tapping mode atomic force microscopy in liquid, Appl. Phys. Lett., **64** (18), 2454–2456 (1994).

[95] Y. Martin and H. K. Wickramasinghe, Magnetic imaging by ”force microscopy” with 1000 Å resolution, Appl. Phys. Lett., **50** (20), 1455–1457 (1987).

[96] J. E. Stern, B. D. Terris, H. Mamin, and D. Rugar, Deposition and imaging of localized charge on insulator surfaces using a force microscope, Appl. Phys. Lett., **53** (26), 2717–2719 (1988).

[97] M. Nonnenmacher, M. P. O’Boyle, and H. K. Wickramasinghe, Kelvin probe force microscopy, Appl. Phys. Lett., **58** (25), 2921–2923 (1991).

[98] Y. Sugawara, Y. Sano, N. Suehira, and S. Morita, Atom manipulation and image artifact on Si(111)7×7 surface using a low temperature noncontact atomic force microscope, Appl. Surf. Sci., **188** (3-4), 285–291 (2002).

[99] N. Sasaki, S. Watanabe, and M. Tsukada, Visualization of thermally fluctuating surface structure in noncontact atomic force microscopy and tip effects on fluctuation: theoretical study of Si(111)-($\sqrt{3} \times \sqrt{3}$)-Ag surface, Phys. Rev. Lett., **88** (4), 046106 (2002).

[100] B. Anczykowski, D. Krüger, and H. Fuchs, Cantilever dynamics in quasi-noncontact force microscopy: spectroscopic aspects, Phys. Rev. B, **53** (23), 15485–15488 (1996).

[101] J. Berg and G. A. D. Briggs, Nonlinear dynamics of intermittent-contact mode atomic force microscopy, Phys. Rev. B, **55** (22), 14899–14908 (1997).

[102] N. Sasaki, M. Tsukada, R. Tamura, K. Abe, and N. Sato, Dynamics of the cantilever in noncontact atomic force microscopy, Appl. Phys. A-Mater., **66**, S287–S291 (1998).

[103] J. P. Aimé, R. Boisgard, L. Nony, and G. Couturier, Nonlinear dynamic behavior of an oscillating tip-microlever system and contrast at the atomic scale, Phys. Rev. Lett., **82** (17), 3388–3391 (1999).

[104] R. García and A. San Paulo, Attractive and repulsive tip-sample interaction regimes in tapping-mode atomic force microscopy, Phys. Rev. B, **61** (20), R13381–R13384 (2000).

[105] K. Yagasaki, Nonlinear dynamics of vibrating microcantilevers in tapping-mode atomic force microscopy, Phys. Rev. B, **70** (24), 245419 (2004).

[106] Q. Zhong, D. Inniss, K. Kjoller, and V. B. Elings, Fractured polymer / silica fiber surface studied by tapping mode atomic force microscopy, Surf. Sci., **290** (1–2), L688–L692 (1993).

[107] R. García and A. San Paulo, Dynamics of a vibrating tip near or in intermittent contact with surface, Phys. Rev. B, **61** (20), R13381–R13384 (2000).

[108] S. Rützel, S. I. Lee, and A. Raman, Nonlinear dynamics of atomic-force-microscope probes driven in Lennard-Jones potentials, Proc. R. Soc. Lon. Sea-A., **459** (2036), 1925–1948 (2003).

[109] P. Gleyzes, P. K. Kuo, and A. C. Boccara, Bistable behavior of a vibrating tip near a solid surface, Appl. Phys. Lett., **58** (25), 2989–2991 (1991).

[110] N. A. Burnham, A. J. Kulik, G. Germaud, and G. A. D. Briggs, Nanosubharmonics: the dynamics of small nonlinear contacts, Phys. Rev. Lett., **74** (25), 5092–5095 (1995).

[111] S. Patil and C. V. Dharmadhikari, Small signal amplification using parametric resonance in NcAFM imaging, Appl. Surf. Sci, **217** (1–4), 7–15 (2003).

[112] Y. Fang, D. Dawson, M. Feemster, and N. Jalili, Nonlinear control techniques for the atomic force microscope system, Proceedings of 2002 ASME International Mechanical Engineering Congress and Exposition, 33539 (ASME, New Orleans, Louisiana, 2002).

[113] Y. Ueda, H. Nakajima, T. Hikihara, and H. B. Stewart, Forced two-well potential Duffing's oscillator, Dynamical Systems Approaches to Nonlinear Problems in Systems and Circuits (eds. F. M. A. Salam and M. L. Levi), 128–137 (SIAM, Philadelphia, 1988).

[114] H. Nakajima and Y. Ueda, Half-period delayed feedback control for dynamical systems with symmetries, Phys. Rev. E, **58** (2), 1757–1763 (1998).

[115] H. Nakajima, Delayed feedback control with state predictor for continous-time chaotic systems, Int. J. Bifurcat. Chaos, **12** (5), 1067–1077 (2002).

[116] G. Duffing, Erwungene Schwingungen bei veränderlicher Eigenfrequenz und ihre technische Bedeutung, (Druck und Verlag von Friedr. Vieweg & Sohn, Braunschweig, 1918).

[117] M. Dellnitz, A. Hohmann, O. Junge, and M. Rumpf, Exploring invariant sets and invariant measures, Chaos, **2** (7), 221–228 (1997).

[118] N. Levinson, Transformation theory of non-linear differential equations of the second order, Ann. Math., **45** (4), 723–737 (1944).

[119] T. Ushio and S. Yamamoto, Delayed feedback control with nonlinear estimation in chaotic discrete-time systems, Phys. Lett. A, **247** (1–2), 112–118 (1998).

[120] T. Ushio and S. Yamamoto, Prediction-based control of chaos, Phys. Lett. A, **264** (1), 30–35 (1999).

[121] K. Konishi and H. Kokame, Observer-based delayed-feedback control for discrete-time chaotic systems, Phys. Lett. A, **248** (5–6), 359–368 (1998).

[122] M. Ye, D. W. Peterman, and P. E. Wigen, Controlling chaos in thin yig films with a time-delayed method, Phys. Lett. A, **203** (1), 23–28 (1995).

[123] J. M. Krodkiewski and J. S. Faragher, Stabilization of motion of helicopter rotor blades using delayed feedback-modelling, computer simulation and experimental verification, J. Sound Vib., **234**, 591–610 (2000).

[124] T. Hikihara, M. Touno, and T. Kawagoshi, Stabilization of unstable periodic orbit in magneto-elastic chaos by delayed feedback control, Int. J. Bifurcat. Chaos, **7** (12), 2837–2846 (1997).

[125] B. Martínez-Zérega, A. N. Pisarchik, and L. S. Tsimring, Using periodic modulation to control coexisting attractors induced by delayed feedback, Phys. Lett. A, **318** (1–2), 102–111 (2003).

[126] A. G. Balanov, N. B. Janson, and E. Schöll, Delayed feedback control of chaos: Bifurcation analysis, Phys. Rev. E, **71** (1), 016222 (2005).

[127] C. Grebogi, E. Ott, and J. A. Yorke, Chaotic attractors in crisis, Phys. Rev. Lett., **48** (22), 1507–1510 (1982).

[128] C. Grebogi, E. Ott, and J. A. Yorke, Crises, sudden changes in chaotic attractors, and transient chaos, Physica D, **7** (1–3), 181–200 (1983).

[129] K. Green, B. Krauskopf, and K. Engelborghs, Bistability and torus break-up in a semiconductor laser with phase-conjugate feedback, Physica D, **173** (1–2), 114–129 (2002).

[130] Y. Ueda, Survey of regular and chaotic phenomena in the forced duffing oscillator, Chaos, Solitons & Fractals, **1** (3), 199–231 (1991).

[131] T. Tél, Transient chaos, Directions in Chaos (ed. B. L. Hao), **3**, (World Scientific, Singapore, 1990), pp. 149–211.

[132] F. C. Moon and G. X. Li, Fractal basin boundaries and homoclinic orbits for periodic motion in a two-well potential, Phys. Rev. Lett., **55** (14), 1439–1442 (1985).

[133] C. Grebogi, E. Ott, and J. A. Yorke, Basin boundary metamorphoses: changes in accessible boundary orbits, Physica D, **24** (1–3), 243–262 (1987).

[134] C. Grebogi, E. Ott, and J. A. Yorke, Metamorphoses of basin boundaries in nonlinear dynamical systems, Phys. Rev. Lett., **56** (10), 1011–1014 (1986).

[135] C. Hayashi, Nonlinear Oscillations in Physical Systems, (McGraw-Hill, Inc., 1964).

[136] M. Basso, R. Genesio, L. Giovanardi, A. Tesi, and G. Torrini, On optimal stabilization of periodic orbits via time delayed feedback control, Int. J. Bifurcat. Chaos, **8** (8), 1699–1706 (1998).

[137] A. R. Bergen and R. L. Franks, Justification of the describing function method, SIAM J. Control, **9** (4), 568–589 (1971).

[138] R. K. Miller and A. N. Michel, On existence of periodic motions in nonlinear control systems with periodic inputs, SIAM J. Control Optim., **18** (5), 585–598 (1980).

[139] R. W. Stark and W. M. Heckl, Higher harmonics imaging in tapping-mode atomic-force microscopy, Rev. Sci. Instrum., **74** (12), 5111–5114 (2003).

[140] S. Crittenden, A. Raman, and R. Reifenberger, Probing attractive forces at the nanoscale using higher-harmonic dynamic force microscopy, Phys. Rev. B, **72** (23), 235422 (2005).

[141] F. Jamitzky, M. Stark, W. Bunk, W. M. Heckl, and R. W. Stark, Nonlinear dynamics of a microcantilever in close proximity to a surface, Proc. 2004 4th IEEE Conf. Nanotechnology, 38–40 (IEEE, 2004).

[142] T. Luzyanina, K. Engelborghs, and K. Lust, Computation, continuation and bifurcation analysis of periodic solutions of delay differential equations, Int. J. of Bif. and Chaos, **7** (11), 2547–2560 (1997).

[143] H. Ito and A. Kumamoto, Locating fold bifurcation points using subspace shooting, IEICE Trans. Fundamentals, **E81-A** (9), 1791–1797 (1998).

[144] J. Mertz, O. Marti, and J. Mlynek, Regulation of a microcantilever response by force feedback, Appl. Phys. Lett., **62** (19), 2344–2346 (1993).

[145] N. Ookubo and S. Yumoto, Rapid surface topography using a tapping mode atomic force microscope, Appl. Phys. Lett., **74** (15), 2149–2151 (1999).

[146] T. Sulchek, R. Hsieh, J. D. Adams, G. G. Yaralioglu, S. C. Minne, C. F. Quate, J. P. Cleveland, A. Atalar, and D. M. Adderton, High-speed tapping mode imaging with active Q control for atomic for microscopy, Appl. Phys. Lett., **76** (11), 1473–1475 (2000).

[147] N. Kodera, H. Yamashita, and T. Ando, Active damping of the scanner for high-speed atomic force microscopy, Rev. Sci. Instrum., **76** (5), 053708 (2005).

[148] B. Anczykowski, J. P. Cleveland, D. Krüger, V. Elings, and H. Fuchs, Analysis of the interaction mechanisms in dynamic mode SFM by means of experimental data and computer simulation, Appl. Phys. A-Mater., **66** (S1), S885–S889 (1998).

[149] W. van de Water and J. Molenaar, Dynamics of vibrating atomic force microscopy, Nanotechnology, **11** (3), 192–199 (2000).

List of publications

Journal articles

- K. Yamasue and T. Hikihara, Domain of attraction for stabilized orbits in time delayed feedback controlled Duffing systems, Phys. Rev. E 69(5), 056209 (2004).

- K. Yamasue and T. Hikihara, Persistence of chaos in a time-delayed-feedback controlled Duffing system, Phys. Rev. E 73(3), 036209 (2006).

- K. Yamasue and T. Hikihara, Control of microcantilevers in dynamic force microscopy using time delayed feedback, Rev. Sci. Instrum. 77(5), 053703 (2006).

- K. Yamasue and T. Hikihara, Annihilation of periodic orbits and global dynamics in time-delayed feedback control of chaos, (to be submitted).

International conference proceedings

- T. Hikihara and K. Yamasue, A Study on domain of attraction in time-delayed feedback controlled Duffing system, Dynamics Days Europe 2002, Heidelberg, Germany, July 15-19 (2002).

- K. Yamasue and T. Hikihara, Influence of remaining chaos on convergence of solutions in time delayed feedback controlled Duffing system, XXI International Congress of Theoretical and Applied Mechanics, Warsaw, Poland, August 15-21 (2004).

- K. Yamasue and T. Hikihara, A study on multiple steady states and their relation to global structure in time delayed feedback controlled Duffing System, 2004 International Symposium on Nonlinear Theory and its Applications, Fukuoka, Japan, November 29 - December 3 (2004).

- K. Yamasue and T. Hikihara, Improvement of transient response in non-contact atomic force microscopy: an application of time delayed feedback control, XXV Dynamics Days Europe 2005, Berlin, Germany, July 25-28, (2005).

- K. Yamasue and T. Hikihara, Annihilation of periodic orbits in time delayed feedback controlled systems, 2005 International Symposium on Nonlinear Theory and its Applications, SEC@BRUGES, Bruges, Belgium, October 18-21 (2005).

- K. Yamasue and T. Hikihara, Suppression of subharmonics and chaos in tapping mode atomic force microscopy using time delayed feedback control, 2006 International Symposium on Nonlinear Theory and its Applications, Bologna, Italy, September 11-14 (2006).

Domestic conference proceedings and technical reports

- T. Hikihara and K. Yamasue, A numerical study on stabilization process via unstable coexisting orbits in magneto-elastic system under delayed feedback control, in Proceedings of the 46th Annual Conference of the ISCIE, International conference center Kobe, Japan, May 15-17 (2002).

- T. Hikihara and K. Yamasue, Domain of attraction for initial function space towards convergent solutions in Duffing system under time-delayed feed-

back control, Technical report NLP2002-50, IEICE, Toyonaka Campus, Osaka University, September 3-4 (2002).

- K. Yamasue and T. Hikihara, A study on domain of attraction in function space under a time delay system—time delayed feedback control of Duffing system—, in Proceedings of the 47th Annual Conference of the ISCIE, Kyoto Terrsa, May 14-16 (2003).

- K. Yamasue and T. Hikihara, Relationship between invariant manifold and convergence of solution in magneto-elastic beam system under time delayed feedback control, Technical report NLP2003-32, IEICE, Future University-Hakodate, July 14-15 (2003).

- K. Yamasue and T. Hikihara, On remain of chaos in time delayed feedback control and its influence on transient behavior, in Proceedings of the 48th Annual Conference of the ISCIE, Kyoto Terrsa, May 19-21 (2004).

- K. Yamasue and T. Hikihara, Multiple steady states and their relation to remaining chaos in time delayed feedback controlled Duffing System,Technical report CAS2004-25/NLP2004-37, IEICE, Katsura Campus, Kyoto University, September 13-14 (2004).

- K. Yamasue and T. Hikihara, Application of time delayed feedback control to non-contact atomic force microscopy,Technical report NLP2004-38, IEICE, Kagawa University, January 24-25 (2005).

- K. Yamasue and T. Hikihara, Improved transient response in non-contact atomic force microscopy under time delayed feedback control, 2005 IEICE General Conference, Toyonaka campus, Osaka university, March 21-24 (2005).

- K. Yamasue and T. Hikihara, Stabilization of microcantilever probe motion in non-contact atomic force microscopy: application of time delayed feed-

back control, in Proceedings of the 49th Annual Conference of the ISCIE, Kyoto Terrsa, May 18-20 (2005).

- K. Yamasue and T. Hikihara, Prototyping of cantilever controller for tapping-mode atomic force microscopy: verification experiment toward implementation of the time-delayed feedback control, in Extended Abstracts (The 54th spring meeting, 2007); The Japan Society of Applied Physics and Related Societies, Sagamihara campus, Aoyama Gakuin University, March 27-30 (2007, submitted).

- K. Yamasue and T. Hikihara, Annihilation of periodic orbits and global dynamics in time-delayed feedback control of chaos, in Proceedings of the 51st Annual Conference of the ISCIE, Kyoto Terrsa, May 16-18 (2007, submitted).